Monte Carlo Simulations of Light Propagation in Human Sinus Cavities

Diploma Paper
by
Elias Kristensson and Lisa Simonsson

Abstract

A study in Sweden, has shown that about 2.2% of all consultations with the Primary Care Unit are due to problems with the sinus cavities. In 1993, 2.8% of the Swedish population got diagnosed with sinusitis. Today, it is hard to, in a simple way, diagnose sinusitis. It is very difficult to tell sinusitis from a normal cold. Simple tools and techniques have been requested to improve the diagnosis for a long time.

We investigate the possibility of using diode laser gas spectroscopy for sinusitis diagnostics, by simulating light propagation based on the Monte Carlo method, implemented by the software Advanced Systems Analysis Program (ASAP^{TM}). Simulations and experimental data have been compared for a model based on two scattering plates, representing human tissue, with an air gap in between, representing the sinus cavity. Simulations have also been performed to optimize the detection geometries used in the experiments. The possibility of imaging measurements of the sinuses has as well been studied.

The results show good resemblance between the simulations and experimental data, even though there are differences on a detailed level. No general optimal detection geometry is found but there are optimal detection geometries for some properties of the scattering plates and some measurement techniques. Imaging simulations on the frontal and maxillary sinuses have also been performed, showing that there are possibilities to spatially study these sinuses with moderate resolution.

Contents

Chapter 1

Introduction

1.1 Background

The Applied Molecular Spectroscopy Group at the Atomic Physics Division at the Lund Institute of Technology has developed a technique with potential to do human sinusitis (inflammation of the sinus cavity) diagnostics, by studying the oxygen content in the sinus cavities, using diode laser spectroscopy [1]. The intention is to find a simple way to improve the diagnostics of sinusitis, which is a disease affecting 37 million people annually just in the US [2]. This special technique of using diode laser spectroscopy on gas imbedded in scattering media has been named GASMAS (GAs in Scattering Media Absorption Spectroscopy).

This technique [3] has also been used for several other applications apart from sinusitis diagnostics, such as studies of oxygen in wood, epoxy, fruits and other provisions [4, 5]. Besides from oxygen, water vapor has recently been investigated [6].

The setup is quite simple and cheap, while the theory behind is more complicated. This makes GASMAS an excellent chance for qualified research in, e.g., developing countries. The Applied Molecular Spectroscopy group is today working together with researchers from Sri Lanka, Ghana and Kenya, on setups being shipped to these countries. Equipment has also been installed in Ecuador and Zimbabwe. This is hopefully a good way of promoting useful spectroscopic research in these places.

The group is also involved in environmental investigations, using laser spectroscopy with the LIDAR (LIght Detection And Ranging) technique. LIDAR measurements are done in varying situations, like measuring air pollution, sulphur concentrations in volcano plumes and algae invasion of historical monuments, etc. [7, 8].
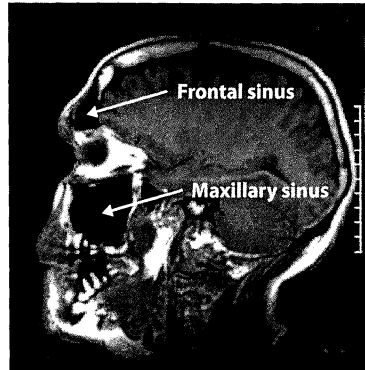
Figure 1.1: *MRI image of a human head with the maxillary and frontal sinuses indicated.*

1.2   Motivation of thesis

A study in Sweden, has shown that about 2.2% of all consultations with the Primary Care Unit are due to problems with the sinus cavities. In 1993, 2.8% of the Swedish population got diagnosed with sinusitis. Today, it is hard to, in a simple way, diagnose sinusitis. It is very difficult to tell sinusitis from a normal cold. Simple tools and techniques have been requested to improve the diagnosis for a long time [9].

The GASMAS technique might be a new alternative way to diagnose sinusitis, since the locations of the sinus cavities make them reachable with optical light, see Fig. 1.1. Two detection geometries are applicable with the GASMAS technique; backscattering geometry and transmission geometry, see Fig. 1.2.
The backscattering geometry can be used for studies of the frontal sinuses as well as the maxillary sinuses, while the transmission geometry is only applicable on the maxillary sinuses. To increase the understanding of how the laser light behaves, when (experimentally) studying the human sinuses, in the two geometries, and to improve the experimental GASMAS set-up, Monte Carlo simulations of light propagation in the backscattering and transmission geometry are motivated.

1.3   Scope of thesis

The thesis work includes:

1. A comparison between results from phantom model experiments performed by the Applied Molecular Spectroscopy Group, on the potential of human sinus cavity diagnostics using diode laser spectroscopy and Monte Carlo simulations done in the ray tracing program ASAP^{TM}.
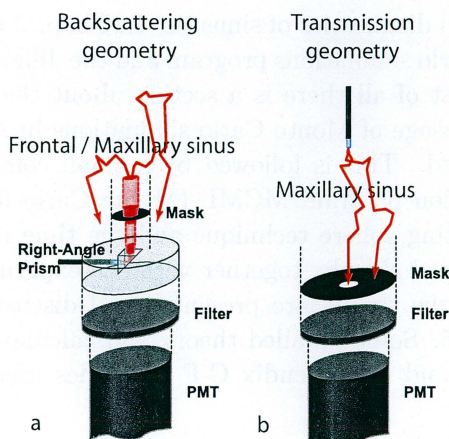
Figure 1.2: *Illustrating applicable detection geometries with the GASMAS technique for human sinuses studies. (a) The backscattering geometry, which can be used for human frontal and maxillary sinus studies. (b) The transmission geometry which can be used for human maxillary sinus studies. (Figure adapted from Ref. [1]).*

2. An investigation of optimal detection apertures for the two different geometries (backscattering and transmission), for the phantom models used in the experiments mentioned above.

3. A study of the influence of different scattering properties of the tissue and an investigation of optimal detection geometries for these models.

4. A comparison of the optimal detection geometries achieved from the diffusion equation and the Monte Carlo simulations.

5. Simulations to study the imaging potential of the technique as well as optimization of the detection apertures to achieve best resolution.

All Monte Carlo simulations have been implemented in ASAP^TM and analyzed in Matlab.

1.4 Outline

The thesis starts with a theory chapter, Chap. 2, where the following aspects are treated: spectroscopy including absorption spectroscopy and molecular spectroscopy, light propagation in scattering media including a discussion on optical properties, a general description of the transport equation, the diffusion equation and Monte Carlo simulations, wavelength modulation with lock-in detection, the theory of GASMAS (GAs in Scattering Media Absorption Spectroscopy) and a section about the human sinuses, including

anatomy, sinusitis and diagnostics of sinusitis. In Chap. 3 there are descriptions of the Monte Carlo simulations program and the different measurement techniques used. First of all there is a section about the ray tracing program ASAP$^{\text{TM}}$, the usage of Monte Carlo simulations in ASAP$^{\text{TM}}$and how the output is analyzed. This is followed by a small comparison with the Monte Carlo simulation program MCML (Monte Carlo for Multi-Layered media). The integrating sphere technique and the time resolved measurement are then explained shortly, together with the experimental GASMAS set-up. In Chap. 4 the results are presented and discussed. Conclusions are drawn in Chap. 5. Some detailed theory and calculations are found in Appendix A and B, and in Appendix C-F the codes used in ASAP$^{\text{TM}}$are found.

Chapter 2

Theory

2.1 Spectroscopy

2.1.1 Absorption spectroscopy

Electromagnetic radiation can be absorbed by atoms and molecules in free gases as well as in liquids and solids. If the energy of the radiation corresponds to an energy difference, ΔE, between two possible energy levels, the energy can be transferred to the atom or molecule, which then will be excited, by promotion of an electron to a higher orbit. After the excitation the electron goes back to its preferred lower energy state by emission of electromagnetic radiation of a certain wavelength, again corresponding to the same ΔE. The absorption is seen as a loss in transmitted radiation intensity for the energy region of absorption. Even though the emitted radiation from the relaxation process is of the same energy, ΔE, as the absorbed light, it will not influence the radiation intensity since it emits light in random directions. This means that the probability for emission in the direction of the traversing beam is very small. Further at atmospheric pressure, which is the relevant case in our study, the deexcitation normally occurs non-radiatively, in collision processes [10].

The absorption spectra of free gases do not look like the absorption spectra of liquids and solids. The shape of the spectrum depends on the energy levels of the atoms or molecules under study, which are different depending on their phase (gas, liquid or solid). A free gas has discrete energy levels and therefore sharp absorption lines. Only radiation of correct wavelengths can excite the electrons and the same wavelengths are emitted during relaxation.

Liquids and solids do not have discrete energy levels but broader energy bands, due to the interaction between the atoms or molecules. This results in very broad absorption lines as a whole wavelength region may be absorbed [11].

In the case of the absorption spectrum of a free gas in human sinuses it
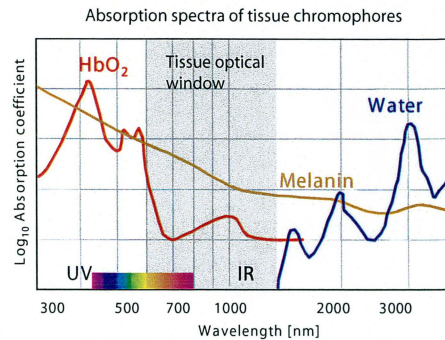
Figure 2.1: *The absorption spectra of tissue chromophores. In the figure the so-called tissue optical window is also indicated. (Figure adapted from [12]).*

is important to get the light to interact with the gas cell (the sinuses). The main problems are absorption and scattering of light by the surrounding tissue. Water and chromophores like hemoglobin and melanin absorb the light; the extent of the absorption depends on the wavelength of the light. Absorption spectra of the main absorbers in human tissue are seen in Fig. 2.1. In a certain wavelength region, also indicated in Fig. 2.1, between approximately 630 nm and 1300 nm, the total absorption is quite low [13]. It is in this region, also called the tissue optical window, that the absorption spectrum of the free gas must be studied, to be able to penetrate the tissue and interact with the gas in the sinuses.

2.1.2   Molecular spectroscopy

Molecular gaseous oxygen, O_2, is a diatomic molecule, which has electronic energy levels as well as different vibrational and rotational energies leading to the appearance of so-called ro-vibrational levels.

Rotational energy

To describe the energy of a rotator a classical approach is a good start. A diatomic molecule with the atomic masses m_1 and m_2 at distances r_1 and r_2 from the center of gravity, according to Fig. 2.2, gives the relations

$$r = r_1 + r_2 \qquad [m] \tag{2.1}$$

$$m_1 r_1 = m_2 r_2 \qquad [kgm] \tag{2.2}$$

$$I = m_1 r_1^2 + m_2 r_2^2 \qquad [kgm^2] \tag{2.3}$$

where I is the moment of inertia with respect to the rotational axis. Rearranging of Eqs 2.1 - 2.3 provides

$$I = \frac{m_1 m_2}{m_1 + m_2}(r_1 + r_2)^2 = \mu r^2 \qquad [kgm^2] \tag{2.4}$$
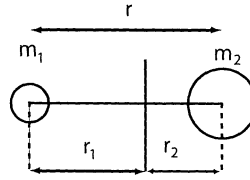
Figure 2.2: *Diatomic molecule seen as a rotator. Two atoms with mass m_1 and m_2 located at r_1 and r_2 from the center of gravity.*

where μ is the reduced mass and $r = r_1 + r_2$ is the distance between the two atoms. From classical mechanics it is known that the angular momentum **L** is given by

$$\mathbf{L} = \frac{I\omega}{\hbar} \qquad [kgm^2 s^{-1}] \tag{2.5}$$

and the energy E is

$$E = \frac{I\omega^2}{2} \Rightarrow E = \frac{\mathbf{L}^2 \hbar^2}{2I} \qquad [J] \tag{2.6}$$

where ω is the angular frequency vector. Now, this is not the classical world but rather the quantum mechanical. Thus, the angular momentum **L** is given by

$$|\mathbf{L}| = \sqrt{J(J+1)}, \qquad J = 0, 1, 2, \ldots \tag{2.7}$$

with the following quantized energies of the rotator

$$E_J = \frac{J(J+1)\hbar^2}{2I} = BJ(J+1), \qquad J = 0, 1, 2, \ldots \tag{2.8}$$

The quantity B is known as the rotational constant and sets the scale of the energy separation between rotational levels. It is of the order of 10^{-3} eV or 3 cm^{-1} [14].

Vibrational energy

The diatomic molecule can be approximated to a harmonic oscillator (two masses connected by a spring). For small displacements the stretching and compression of the bond (the spring), obey Hooke's law:

$$F_{restoring} = -\frac{dV(x)}{dx} = -kx \qquad [N] \tag{2.9}$$

where V is the potential energy, k is the force constant, which reflects the strength of the bond, and x is the displacement from the equilibrium bond length. From this relationship the potential energy is given as

$$V(x) = \frac{1}{2}kx^2 \qquad [J] \tag{2.10}$$
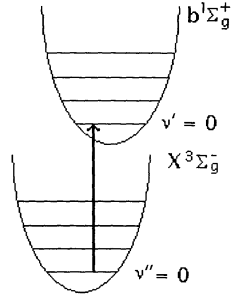
Figure 2.3: *Transitions between the vibronic states located in the ground and excited electronic states which give rise to the oxygen A-band.*

Plotted against x, the potential V behaves parabolical, as seen in Fig. 2.3. From quantum mechanics the vibrational energy levels E_v of such a diatomic molecule are given by

$$E_v = h\nu \left(v + \frac{1}{2}\right) \qquad [J] \qquad v = 0, 1, 2, \ldots \qquad (2.11)$$

where v is the vibrational quantum number and ν is the classical vibrational frequency, which is determined by the reduced mass, μ and the force constant, k [N/m], as

$$\nu = \frac{1}{2\pi} \left(\frac{k}{\mu}\right)^{\frac{1}{2}} \qquad [s^{-1}] \qquad (2.12)$$

The force constant corresponds to the strength of the spring of the approximated harmonic oscillator [15]. Molecular oxygen has a force constant of approximately 11 $k/aJ\mathring{A}^{-2}$. The physical origin of the force are nuclear repulsions, electron repulsions and electron-nuclear attractions.

Electronic levels and the oxygen A-band

The electronic levels of a molecule are more complicated than those of an atom. As this is no report on the basics of molecular structure we are satisfied with the fact that there is a ground electronic state in O_2, called $X^3\Sigma_g^-$ and an excited state called $b^1\Sigma_g^+$, (interested readers are referred to Refs [14] and [15]). The band of transition lines from the vibronic state $v = 0$ of the electronic ground state and the vibronic state $v = 0$ of the excited electronic state is called the A-band; see Fig. 2.3.
In this band the R7R7 transition line (described below), used for human sinuses studies, is found [16].
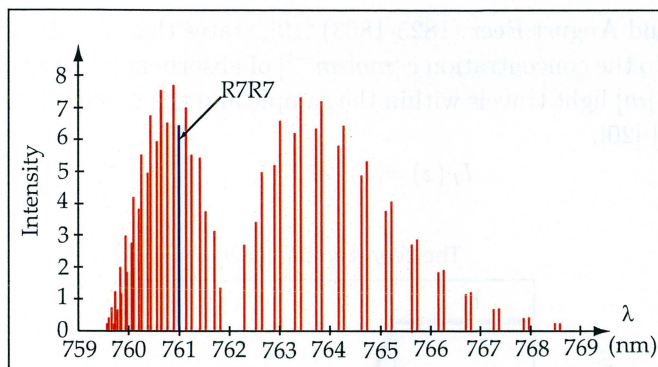
Figure 2.4: *The oxygen A-band, with the R7R7 line indicated, located at 761.003 nm.*

The R7R7 line of the oxygen A-band

The line of study, called R7R7 located at 761.003 nm, is seen in Fig. 2.4 and is a magnetic dipole transition; see Appendix A, between energy levels arising from the coupling between the rotational angular momentum **N** and the total electron spin **S**, according to Hund's case (b).

This means that there is a total angular momentum **J** such that $\mathbf{J} = \mathbf{N} + \mathbf{S}$. In the ground electronic state of molecular oxygen $X^3\Sigma_g^-$ where S = 1, there are three J levels for each N. In the excited electronic state of molecular oxygen, $b^1\Sigma_g^+$, S = 0, which only gives one J level by J = N. Transitions where $\Delta N = N' - N'' = +1$ belong to the R-branch and the same holds for $\Delta J = J' - J''$. ($\Delta N = -1$ and $\Delta J = -1$ belong to the P-branch) Here N' and J' is in the excited electronic level and N'' and J'' is in the ground level. One notation commonly used is $^{\Delta N}\Delta J(N'')$. In this case the notation is $^R R(7)$ or R7R7 which thus means the transition

$$\Delta N = N' - N'' = 8 \leftarrow 7 \tag{2.13}$$

$$\Delta J = J' - J'' = 8 \leftarrow 7 \tag{2.14}$$

However, this notation does not indicate the vibrational transition, which explains why the notation often is followed by the name of the band [17].

The fact that the line is a magnetic dipole transition means that it is forbidden as an electric dipole transition, or more exact; its transition probability is only 10^{-5} of a typical electronic transition. This results in a 10^{-5} times weaker line than for an electric dipole transition [18].

2.1.3 The Beer-Lambert law

Light, at any wavelength, impinging an sample of thickness z containing absorbers, is reduced in intensity from I_0 to I_T (see Fig. 2.5). The Beer-Lambert law (Eq. 2.15), which is named after Johann Heinrich Lambert

(1728-1777) and August Beer (1825-1863) [19], states that the absorbance is proportional to the concentration c $[mol \cdot m^{-3}]$ of absorbers in the sample, the path length z $[m]$ light travels within the sample and the molar absorbability e $[mol^{-1} \cdot m^2]$ [20].

$$I_T(z) = I_0 \cdot e^{-e \cdot c \cdot z} \qquad (2.15)$$
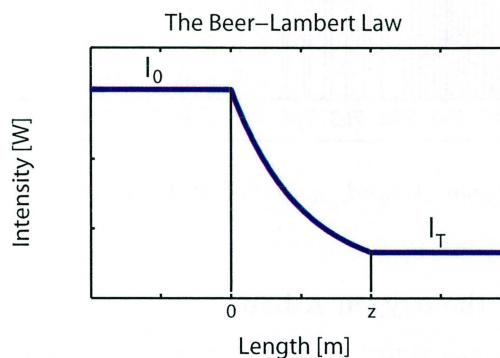
Figure 2.5: *Illustration of how, according to the Beer-Lambert law (Eq. 2.15), the intensity of an incoming light is reduced exponentially due to absorbers inside a sample with the length z.*

2.2   Light propagation in scattering media

Human tissue is a very good example of a scattering medium. When light enters tissue it is scattered due to random spatial variations in tissue density, refractive index and dielectric constant. The light is scattered according to Mie scattering, since the particles are much larger than the wavelength of the light [21].

Scattering is wavelength dependent and, for mixtures of scatterers of different size, it monotonically decreases with wavelength. The light can be scattered as well as be absorbed by molecules. The fraction being absorbed depends on the wavelength of the light and what molecules being interrogated. Tissue components that absorb light are called *chromophores*. For living tissue, and studying the visible wavelength range, the most important chromophores are water, blood and melanin. Melanin forms small ($\sim$1 μm) pigment granules in the skin and eye. The absorption coefficient of melanin decreases with increasing wavelength, as shown in Fig. 2.1. Blood absorption depends highly on the wavelength as well as the oxygenation, as the absorption spectrum of oxyhemoglobin and deoxyhemoglobin differ from each other. In the UV wavelength range the main absorbers are proteins and amino acids, and for IR wavelengths water is responsible for most of the absorption. As the photons undergo multiple scattering in the tissue
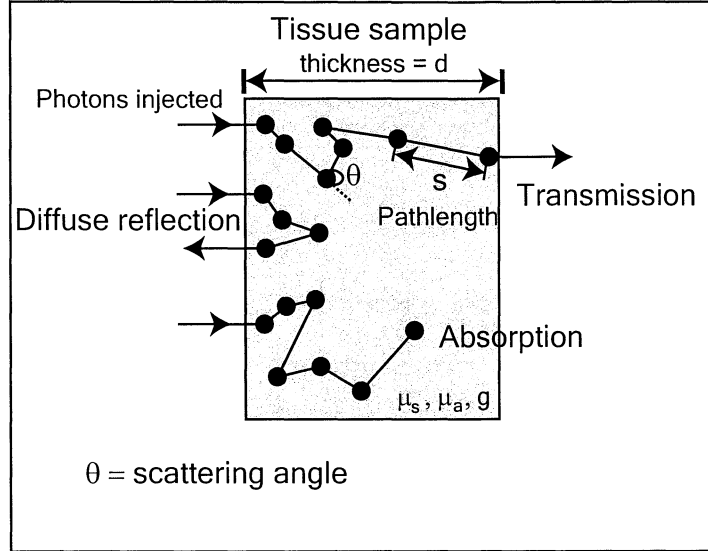
Figure 2.6: *Light interaction with tissue is shown. Scattering and absorption events are illustrated as well as diffuse reflectance and transmission.*

as well as being absorbed it is quite complex to describe the propagation. Using the Maxwell wave equations is not possible. In this study the Monte Carlo method (see Chap. 2.2.4) is used, which is based upon a stochastic model and the transport equation, described in Sect. 2.2.2, to describe this phenomenon [13].

2.2.1 Optical properties

The theory given in this section basically follows that presented in Ref. [13].

Scattering and absorption coefficients

The probability of absorption is determined by the absorption coefficient, μ_a [m^{-1}], times an infinitesimal distance, ds, which the photon has been propagated over. The same is valid for the scattering with a scattering coefficient, μ_s [m^{-1}]. Scattering and absorption events are shown in Fig. 2.6.

The inverse of μ_a and μ_s is the mean free path for an absorption and scattering event, respectively. The sum of μ_a and μ_s is referred to as the total attenuation coefficient, μ_t [m^{-1}]:

$$\mu_t = \mu_s + \mu_a \tag{2.16}$$

The absorption coefficient gives a probability distribution function F, for absorption in a distance less than s:

$$F_a(s) = 1 - e^{-\mu_a s} \tag{2.17}$$

Later Monte Carlo modeling will be discussed and in that context the probability distribution will be used.

Application of Beer Lambert's law

If tissue would not have been scattering but just absorbing, the spatial light distribution could be described by Beer's law (also explained in Sect. 2.1.3) of exponential attenuation

$$E(z) = E_0(1 - r)e^{-(\mu_a + \mu_s)z}, \qquad \mu_s = 0 \qquad (2.18)$$

where $E(z)$ is the fluence rate of *collimated* light at position z. E_0 is the collimated irradiance and r is the Fresnel surface reflection, which will be discussed later.

No matter how complicated the relations for scattered light are, the fluence rate distribution of collimated light with tissue depth is always governed by Beer's law Eq. 2.18. For a non-scattering medium, the absorption coefficient can be determined form the slope of a plot of $\ln T_c$ versus sample thickness, z. T_c is the collimated transmission.

$$\ln T_c = \ln \left[\frac{E(z)}{E_0} \right] = \ln(1 - r) - \mu_a z \qquad \text{for } \mu_s = 0 \qquad (2.19)$$

Theoretically, for a scattering medium, the slope of $\ln T_c$ versus z gives the total attenuation coefficient, μ_t. However, it is very difficult to measure transmission of only collimated light, as it is hard to separate it from scattered light.

Effects of the refractive index

One of the important optical properties is the refractive index of the scattering medium. The difference in refractive index between air and tissue gives rise to both refraction of the transmitted light and Fresnel reflection. The Fresnel reflection is given by

$$R(\theta_i) = \frac{1}{2} \left[\frac{sin^2(\theta_i - \theta_t)}{sin^2(\theta_i + \theta_t)} + \frac{tan^2(\theta_i - \theta_t)}{tan^2(\theta_i + \theta_t)} \right] \qquad (2.20)$$

where θ_i is the angle of the incoming light and θ_t is the angle of the light transmitted (refraction of the transmitted light) into the medium. The angle of the transmitted beam is given by Snell's law

$$n_i \sin \theta_i = n_t \sin \theta_t \qquad (2.21)$$

where n_i is the refractive index of air and n_t is the refractive index of the medium of interest. For a unit irradiance, the light transmitted into the tissue is given by

$$T = 1 - R \qquad (2.22)$$

Another effect which has to be handled is the total internal reflection. This occurs when the light inside the tissue strikes the surface with an angle θ larger than the critical angle θ_c, which is given by

$$\sin \theta_c = \frac{n_1}{n_2} \sin 90° = \frac{n_1}{n_2} \qquad \text{for } n_1 < n_2 \tag{2.23}$$

$$\Rightarrow \theta_c = \arcsin \left(\frac{n_1}{n_2} \right) \tag{2.24}$$

Fresnel reflection is not the only form of reflection that occurs when a scattering medium is being irradiated by laser light. The photons injected in the medium are undergoing multiple scattering, being diffuse and some amount may be backscattered. The backscattered light reaching the surface is either internally reflected or transmitted according to Fresnel's relation given in Eq. 2.20. The total measured reflection is thereby given from

$$R_t = r + R_d \tag{2.25}$$

where R_t is the total reflectance, r is the specular Fresnel reflection at the surface and R_d is the diffuse backscattered light.

Phase function

A further important property of the scattering medium is the phase function, which tells the probability for the photon trajectory being deflected an angle θ in the interval $[0, \pi]$. The calculations of the phase function are based on the assumption that the tissue is isotropic in terms of physical properties (refractive index, density, etc.). This means that the scattering is said to only depend on the angle θ between the unit vector directions $\hat{s}$ and $\hat{s}'$. The vector $\hat{s}$ describes the direction the light comes from, and $\hat{s}'$ is the direction the light will be scattered to. Now it is possible to write the single scattering probability density function $p(\hat{s},\hat{s}')$ as

$$p(\hat{s}, \hat{s}') = p(\cos \theta) = p(\sigma) \tag{2.26}$$

where $\sigma = \cos \theta$. The integral of the density function over its domain is equal to one.

$$\int_{4\pi} p(\hat{s}, \hat{s}') d\omega' = 2\pi \int_{-1}^{1} p(\sigma) d\sigma = 1 \tag{2.27}$$

If single scattering is isotropic, which means that the phase function equals a constant, the single scattering probability density function is

$$p(\hat{s}, \hat{s}') = p(\mu) = \frac{1}{4\pi} \tag{2.28}$$

Light scattering in tissue is not isotropic; it is strongly forward scattered. The anisotropy factor, g [dimensionless], is a measure of the anisotropy of

the scattering. It is defined as the expectation value of the cosine of the scattering angle θ

$$g = \frac{\int_{4\pi} p(\hat{s}, \hat{s}')(\hat{s} \cdot \hat{s}')d\omega}{\int_{4\pi} p(\hat{s}, \hat{s}')d\omega} = \int_{4\pi} p(\hat{s}, \hat{s}')(\hat{s} \cdot \hat{s}')d\omega \qquad (2.29)$$

The second relation is true due to the normalization condition of Eq. 2.27. An anisotropy factor of $g = 1$ means total forward scattering and an isotropic scatterer has an anisotropy factor of $g = 0$. When measured for in vitro tissues and in the visible and near-infrared region, g varies between about 0.7 and 0.99 [13]. One of many functions postulated to represent the single scattering phase functions for tissue is the Henyey-Greenstein function, which was originally proposed for galactic light scattering. This function approximates Mie scattering by particles about the same size as the wavelength of the light and is given by

$$p(\cos\theta) = \frac{1 - g^2}{2(1 + g^2 - 2g\cos\theta)^{\frac{3}{2}}} \qquad (2.30)$$

It is convenient to substitute the variable μ for the factor $\cos\theta$, so that μ is distributed in the interval [-1, 1]. The density function proposed by Henyey and Greenstein gives the following identity

$$g = \int_{-1}^{1} p(\sigma)\sigma d\sigma = <\sigma> \qquad (2.31)$$

which is the definition of g. The anisotropy factor both characterizes the average amount of scattering in a medium and specifies the shape of the scattering function; Eq. 2.30.

In tissue optics it is common to use the reduced scattering coefficient

$$\mu_s' = \mu_s(1 - g) \qquad (2.32)$$

where μ_s is the scattering coefficient introduced earlier.

2.2.2 Transport equation

Light scattered from a beam undergoes multiple scattering events as it propagates through tissue. A description of this propagation in terms of Maxwell's wave equations is not possible due to the complexity of tissue. The transport equation that describes the transfer of energy through a turbid medium is an effective alternative approach [13].

There are some precautions to mention, when using the radiative transport theory. The light propagation is treated like a stream of neutral particles (photons), that do not interact with each other. The model simply describes energy transport within the medium.
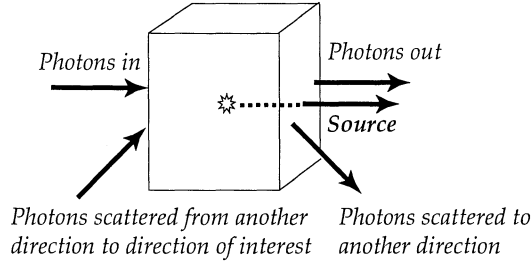
Figure 2.7: *Schematic description of the different parts of the transport equation.*

The transport equation is built up by five different contributions. These are described schematically in Fig. 2.7, figuring a small volume element dV. The equation is expressed as a continuity function of the radiance, $L(\mathbf{r}, \mathbf{s}, t)[W/m^2 sr]$, i.e., the light intensity per unit area and solid angle. The five contributions are:

1. Transmitted light

2. Absorbed light

3. Light scattered from the direction s

4. Light scattered into the direction s

5. Sources within the volume

Together they sum up to the transport equation:

$$\frac{1}{c}\frac{\partial L(\mathbf{r}, \mathbf{s}, t)}{\partial t} = \underbrace{-\mathbf{s} \cdot \nabla L(\mathbf{r}, \mathbf{s}, t)}_{1} \underbrace{- \mu_a L(\mathbf{r}, \mathbf{s}, t)}_{2} \underbrace{- \mu_s L(\mathbf{r}, \mathbf{s}, t)}_{3} +$$

$$+ \underbrace{\mu_s \int_{4\pi} L(\mathbf{r}, \mathbf{s}', t) p(\mathbf{s}, \mathbf{s}') d\omega'}_{4} + \underbrace{Q(\mathbf{r}, \mathbf{s}', t)}_{5} \qquad (2.33)$$

where μ_a is the absorption coefficient, μ_s is the scattering coefficient, c is the speed of light, s is the direction of study and $p(\mathbf{s}, \mathbf{s}')$ is the scattering phase function, which describes the probability of a photon being scattered into direction s from direction s'. It is difficult to solve this equation as there are complications with the coupling to all different directions, s'. This together with boundary conditions and other geometrical aspects make analytical solutions possible only for a few idealized cases. One way to get an approximal solution though, is to derive a so-called diffusion model [22].

2.2.3   The diffusion equation

Under certain assumptions the radiative transport equation can be reduced to a diffusion-type equation, for which, in some cases, an analytical solution exists.

It is traditional to simplify the radiative transport equation into the diffusion equation by expanding the radiance, L, (in Eq. 2.33) into spherical harmonics, Y_{lm} and truncate the expansion.

$$L(\mathbf{r}, \mathbf{s}, t) = \sum_{l=0}^{\infty} \sum_{m=-1}^{l} \sqrt{\frac{2l+1}{4\pi}} L_{lm}(\mathbf{r}, t) Y_{l,n}(\mathbf{s}) \approx$$
$$\approx \frac{1}{4\pi} \left(\phi(\mathbf{r}, t) + 3\mathbf{F}(\mathbf{r}, t) \cdot \mathbf{s} \right) \tag{2.34}$$

This is called the P_1-approximation, as it contains the 0th and the 1st terms, while terms of higher orders are neglected. Eq. 2.34 should be interpreted as the radiance divided into an isotropic term (ϕ) and one term ($\mathbf{F}$), called photon flux, describing the angular dependence of the radiance. These terms can be calculated using

$$\phi(\mathbf{r}, t) = \int_{4\pi} L(\mathbf{r}, \mathbf{s}, t) d\omega \tag{2.35}$$

$$\mathbf{F}(\mathbf{r}, t) = \int_{4\pi} L(\mathbf{r}, \mathbf{s}, t) \mathbf{s} d\omega \tag{2.36}$$

For an isotropic light source, the photon flux is given by Fick's law:

$$\mathbf{F}(\mathbf{r}, t) = -D\nabla\phi \tag{2.37}$$

where the diffusion coefficient D, is defined as

$$D = \frac{1}{3(\mu_a + \mu'_s)} \tag{2.38}$$

The scattering phase function, $p(\mathbf{s}, \mathbf{s}')$ in Eq. 2.33, can also be expanded in a series, in this case of Legendre polynomials, P_l:

$$p(\mathbf{s}, \mathbf{s}') = p(\cos\theta) = \frac{1}{4\pi} \sum_{l=0}^{L} (2l+1) b_l P_l(\cos\theta) \approx$$
$$\approx \frac{1}{4\pi} (1 + 3g\cos\theta) . \tag{2.39}$$

Finally, the source term is expanded and truncated in a similar way:

$$Q(\mathbf{r}, \mathbf{s}, t) \approx \frac{1}{4\pi} \left(q_0(\mathbf{r}, t) + 3\mathbf{q_1}(\mathbf{r}, t) \cdot \mathbf{s} \right) \tag{2.40}$$
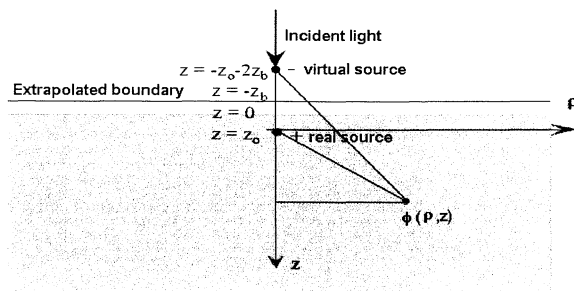
Figure 2.8: *A collimated beam incident on a semi-infinite medium can be modeled as an isotropic point source at a depth of $z_0 = 1/\mu_s'$. A virtual negative point source, mirrored about a virtual surface at $z = -z_e$, is introduced to fulfill the boundary conditions.*

For an isotropic source $q_1 = 0$ and Eq. 2.40 can be expressed as:

$$Q(\mathbf{r}, \mathbf{s}, t) \approx \frac{1}{4\pi} q_0(\mathbf{r}, t) \tag{2.41}$$

By inserting Eqs 2.34, 2.37, 2.39 and 2.41 into Eq. 2.33, the time-dependent diffusion equation is obtained:

$$\frac{1}{c} \frac{\partial \phi(\mathbf{r}, t)}{\partial t} - \nabla (D \nabla \phi(\mathbf{r}, t)) + \mu_a \phi(\mathbf{r}, t) = q_0(\mathbf{r}, t) \tag{2.42}$$

The time-independent diffusion equation for steady-state is written as:

$$-D\nabla^2 \phi(\mathbf{r}) + \mu_a \phi(\mathbf{r}) = q_0(\mathbf{r}) \tag{2.43}$$

This is the diffusion equation later used in this thesis, since only steady-state processes will be considered.

By first studying a semi-infinite medium seen in Fig. 2.8, the analytical steady-state solution for a collimated beam incident on a slab (e.g. a Delrin plate) of thickness l, see Fig. 2.9, can be understood. "Infinite" means that no light escapes along the boundary of that surface, the intensity at the boundary is therefore set equal to zero [23].

Collimated beam, semi-infinite medium

The source can be thought of as an isotropic point source at a depth of $z_0 = 1/\mu_s'$; see Fig. 2.8. This means that all the incident photons are scattered at a single depth, which is an approximation [24]. To meet the boundary conditions at the surface a negative image of the source is introduced at $z = -(2z_b + z_0)$, see Fig. 2.8. At a virtual surface ($z = -z_b$) between the sources the flux will be zero. This extrapolated boundary is introduced to model the Fresnel reflections, which cause the flux to be non-zero in the tissue. The distance is a function of the effective Fresnel reflection coefficient and z_0 [24].

z = -2l

z = -l

z = -z₀-2z_b ● - 2
                              z = -z_b
z = z₀ ● + 1

z = l   z = l + z_b

z = 2l
z = 2l - z₀+ 2z_b ● - 3
z = 2l + z₀+ 4z_b ● + 4
z = 3l

↓ z
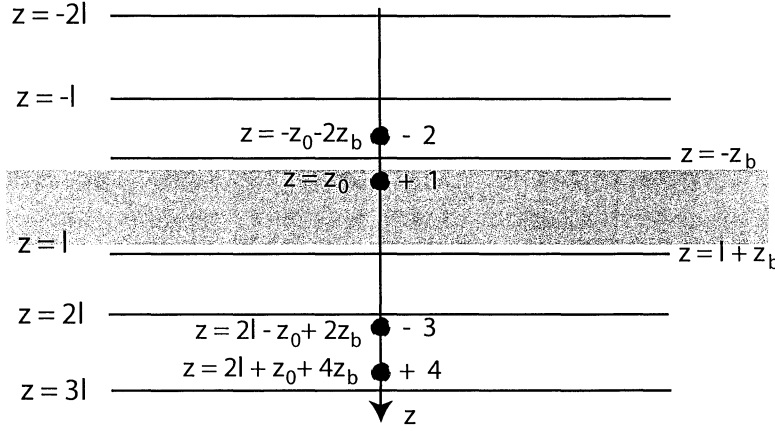
Figure 2.9: *A collimated beam incident on a slab needs extra virtual mirrored sources to fulfill the complex boundary conditions. Source 3 and 4 are mirrored about a virtual surface at $z = l + z_b$.*

Collimated beam, slab geometry

When studying the flux in a Delrin plate (slab geometry) it is more complex to fulfill the boundary conditions. It is now necessary to mirror the source in multiple virtual planes; see Fig. 2.9. The result is a sum of the terms arising from the different virtual sources. As the flux is supposed to be equal to zero in the two extrapolated boundaries, the sources are mirrored about these. To get a good result, mirroring twice may not be enough. However, for each mirroring the virtual sources will be located further from the slab and their contribution to the flux will decrease. In the case of Fig. 2.9, the resulting steady-state diffusion equation will look like

$$\phi(\rho, z) = \frac{P\mu_{eff}^2}{4\pi\mu_a} \left(\frac{e^{-\mu_{eff}r_1}}{r_1} - \frac{e^{-\mu_{eff}r_2}}{r_2} - \frac{e^{-\mu_{eff}r_3}}{r_3} + \frac{e^{-\mu_{eff}r_4}}{r_4} \right) \tag{2.44}$$

where P is the effect of the incoming light and μ_{eff} is the effective attenuation coefficient given by

$$\mu_{eff} = \sqrt{3\mu_a(\mu_a + \mu_s')} \tag{2.45}$$

Finally, r_1, r_2, r_3 and r_4 are the distances to each source, respectively. They are given by

$$r_1 = \sqrt{(z - z_0)^2 + \rho^2} \tag{2.46}$$

$$r_2 = \sqrt{(z + z_0 + 2z_b)^2 + \rho^2} \tag{2.47}$$

$$r_3 = \sqrt{(2l - z - z_0 + 2z_b)^2 + \rho^2} \tag{2.48}$$

$$r_4 = \sqrt{(2l - z + z_0 + 4z_b)^2 + \rho^2} \tag{2.49}$$

The reflectance, R, and the transmittance, T are found by

$$
\begin{aligned}
R(\rho) &= h\nu \mathbf{J}(\rho,0) \cdot \mathbf{n} = D\frac{\partial}{\partial z}\phi(\rho,z)|_{z=0} = \\
&= \frac{1}{4\pi}\Big(z_0\Big(\mu_{eff} + \frac{1}{r_1(z=0)}\Big)\frac{e^{-\mu_{eff}r_1(z=0)}}{r_1^2(z=0)} + \\
&\quad + (z_0 + 2z_b)\Big(\mu_{eff} + \frac{1}{r_2(z=0)}\Big)\frac{e^{-\mu_{eff}r_2(z=0)}}{r_2^2(z=0)} + \\
&\quad + (z_0 - 2d - 2z_b)\Big(\mu_{eff} + \frac{1}{r_3(z=0)}\Big)\frac{e^{-\mu_{eff}r_3(z=0)}}{r_3^2(z=0)} + \\
&\quad + (2d + z_0 + 4z_b)\Big(\mu_{eff} + \frac{1}{r_4(z=0)}\Big)\frac{e^{-\mu_{eff}r_4(z=0)}}{r_4^2(z=0)}\Big) \quad (2.50)
\end{aligned}
$$

$$
\begin{aligned}
T(\rho) &= h\nu \mathbf{J}(\rho,0) \cdot \mathbf{n} = -D\frac{\partial}{\partial z}\phi(\rho,z)|_{z=0} = \\
&= -\frac{1}{4\pi}\Big(z - z_0\Big(-\mu_{eff} - \frac{1}{r_1(z=l)}\Big)\frac{e^{-\mu_{eff}r_1(z=l)}}{r_1^2(z=l)} - \\
&\quad - (z + z_0 + 2z_b)\Big(\mu_{eff} + \frac{1}{r_2(z=l)}\Big)\frac{e^{-\mu_{eff}r_2(z=l)}}{r_2^2(z=l)} - \\
&\quad - (z + z_0 - 2d - 2z_b)\Big(\mu_{eff} + \frac{1}{r_3(z=l)}\Big)\frac{e^{-\mu_{eff}r_3(z=l)}}{r_3^2(z=l)} + \\
&\quad + (z - 2l - z_0 - 4z_b)\Big(\mu_{eff} + \frac{1}{r_4(z=l)}\Big)\frac{e^{-\mu_{eff}r_4(z=d)}}{r_4^2(z=l)}\Big) \quad (2.51)
\end{aligned}
$$

2.2.4 Monte Carlo simulations

Introduction

The theory in this section basically follows that presented in Ref. [25]. A Monte Carlo simulation is based on a stochastic model. This is suitable for simulation of light propagating in scattering media such as human tissue. In Monte Carlo simulations every single photon is followed and its destiny comes out of the stochastic model. When the photon is launched, it is moved a distance Δs and then an event is recorded. The photons may be scattered a certain angle, absorbed by the medium, propagated undisturbed, internally reflected or transmitted out of the medium. The photon is followed step by step, until it is absorbed or leaves the medium. Even the position of absorption or escape is recorded. To achieve a result similar to a real measurement many photons need to be followed. The most significant disadvantage of this method is that it takes long time to make a simulation with good statistics. For a shorter simulation time fast computers are needed. The better the computers get, the more conveniently Monte Carlo simulations can be performed. The fluence rate of the light in the medium can as well be calculated by the Monte Carlo program. A flow chart of how
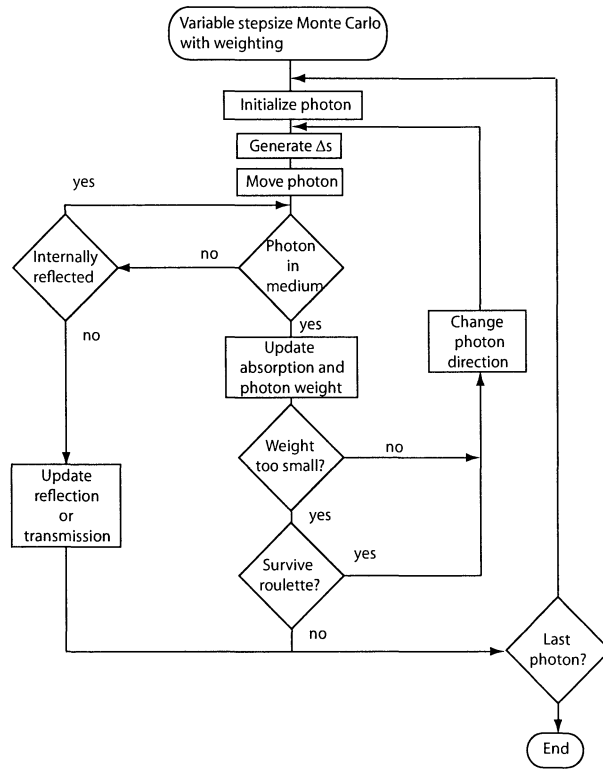
Figure 2.10: *Flow chart of the Monte Carlo model (from Ref. [25]).*

the Monte Carlo model operates is shown in Fig. 2.10. This scheme will be described in the following sections.

Photon introduction

The model starts by initializing a photon into the scattering medium. The beam shape of the incident light can be varied, from a collimated beam, where all photons have an initial direction downwards, to a gaussian distribution of the photons directions. Actually, it is not a photon that is launched but a photon packet. This is to reduce the number of photons needed to get accurate results. Instead of following just one photon until it is absorbed or leaves the medium, a photon packet is followed and in every step a part of it might be absorbed. The packet is given a certain weight (w) which is set to unity when introducing the packet.

Propagation distance

The propagation distance Δs is the distance a photon travels before being absorbed or scattered by the media. Different step sizes are set for

each propagation step to simulate the propagation of a real photon. The Beer-Lambert law, Eq. (2.52), is used to determine the probability density function of the stepsize.

$$P \propto e^{-\mu_t \Delta s} \tag{2.52}$$

where P is the probability and $\mu_t = \mu_a + \mu_s$ is the total attenuation coefficient. From Eq. (2.52) it can be seen that the probability is higher for the photon to travel a short distance than a long distance. The step size is found from

$$\Delta s = \frac{-\ln \xi}{\mu_t}. \tag{2.53}$$

The variable ξ is randomly distributed between zero and one, which will give a value of Δs between zero and infinity.

Changing the coordinates of the photon

Five variables are needed to describe a photon, two directional angles for the traveling direction and three spatial Cartesian coordinates for the position. For convenience the direction of travel is described with three direction cosines. These are specified by taking the cosine of the angle that the direction of the photon makes with each axis. The direction cosines are labeled μ_x, μ_y and μ_z corresponding to the x, y, and z-axes. A photon located at (x, y, z) traveling a distance Δs in the direction (μ_x, μ_y, μ_z) are given the new coordinates (x', y', z') by

$$x' = x + \mu_x \Delta s \tag{2.54}$$

$$y' = y + \mu_y \Delta s \tag{2.55}$$

$$z' = z + \mu_z \Delta s \tag{2.56}$$

Internal reflection

A photon may be internally reflected when it crosses a boundary to a medium with a different refractive index. Whether a photon is internally reflected or not is determined from a random number ξ uniformly distributed between zero and one. Internally reflection occurs if $\xi < R(\theta_i)$ otherwise the photon is recorded to have left the tissue. $R(\theta_i)$ is the Fresnel reflection coefficient

$$R(\theta_i) = \frac{1}{2} \left[\frac{sin^2(\theta_i - \theta_t)}{sin^2(\theta_i + \theta_t)} + \frac{tan^2(\theta_i - \theta_t)}{tan^2(\theta_i + \theta_t)} \right] \tag{2.57}$$

where θ_i is the angle of incidence on the boundary, according to

$$\theta_i = \cos^{-1} \mu \tag{2.58}$$

The other angle θ_t is the angle of transmission and determined by Snell's law

$$n_i \sin \theta_i = n_t \sin \theta_t \tag{2.59}$$

where n_t and n_i are the refractive indices of the medium the photon is being transmitted into and being incident from, respectively. After the photon is internally reflected the new positional and directional coordinates are calculated.

Absorption

Every time a photon packet is moved a distance Δs, a fraction of its weight may be absorbed. The size of this fraction $frac_{abs}$ is decided by

$$frac_{abs} = \frac{\mu_a}{\mu_a + \mu_s} = 1 - \frac{\mu_s}{\mu_a + \mu_s} = 1 - a \qquad (2.60)$$

where a is called the albedo. The weight of the packet which is not absorbed but scattered is incremented by $w' = aw$. When recording an absorption event, both the position of the event and the amount of light being absorbed are concerned. The amount of absorbed light is given by $(1-a)w$.

Photon termination

During the absorption events the weight of every photon packet goes towards zero, but it will never reach zero. This is a problem since it is a waste of time following all those tiny packets, which will give very little information. So why not kill the packets when they have reached a certain minimum weight? As this approach violates the conservation of energy and skews the absorption profile, it is not a good suggestion. The Monte Carlo method uses a so called roulette technique, to decide the destiny of a photon packet with a weight below a certain value. This technique gives a low weight (w) packet one chance in m of surviving. If the photon packet survives it receives a weight of mw otherwise its weight is reduced to zero and the packet is terminated in a way not violating the conservation of energy.

Scattering

Scattering means changing the direction of the photon; this is done after every step Δs. Scattering in tissue is characterized by the Henyey-Greenstein phase function, which depends on the anisotropy, g, having a value in the range between -1 and 1. A g-value of -1 means totally backscattering, 1 means totally forward scattering and an isotropic distribution of the photons has a g-value of 0. The scattering angle θ is given by

$$\cos\theta = \frac{1}{2g}\left(1 + g^2 - \left[\frac{1 - g^2}{1 - g + 2g\xi}\right]^2\right) \qquad (2.61)$$

This equation is only valid if g $\neq$ 0. For an isotropic distribution θ is given by

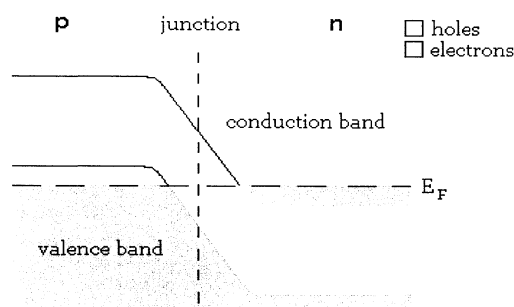$$\cos\theta = 2\xi - 1 \qquad (2.62)$$

Figure 2.11: *Indication of the Fermi level E_F in the region of a p-n junction (adapted from Refs [26, 27]).*

The azimuthal angle ϕ is changed as well and calculated by

$$\phi = 2\pi R \qquad (2.63)$$

where R is a random number between 0 and 1. After the scattering event a new direction is specified with the new angles.

2.3 Diode lasers

Semiconductor lasers, or more often called diode lasers, are very commonly found in CD players, laser printers and bar code readers but are also used in laser spectroscopy, due to uncomplicated wavelength tuning and excellent modulation capabilities [26]. The properties of a diode laser can be understood by the physics of the solid state. The key word for any kind of laser is inverted population. When this is achieved the light source will turn into a laser. The laser action in a diode laser is located in the p-n junction between a p-type and an n-type semiconductor made from the same host material. Such a p-n combination is called a semiconductor diode. The conduction band and valence band energies of the host are shifted in the two semiconductors; see Fig. 2.11.
The bands are filled up with electrons to the Fermi level with the Fermi energy E_F, indicated in Fig. 2.11 [27].

When a voltage is applied over the junction, with the negative and positive terminals attached to the n- and p-regions, respectively, electrons flow from the n-region to the p-region and positive holes flow from the p-region to the n-region. The levels are displaced and the Fermi energies $E_F'(n)$ and $E_F''(p)$ are unequal; see Fig. 2.12. This results in an inverted population in the junction region and the desired laser action is achieved [27].
One practical advantage with the semiconductor laser is its small size; it is typically only a millimeter long and has an effective thickness of a few μm. The wavelength of the emitted laser light can be tuned, but the tuning
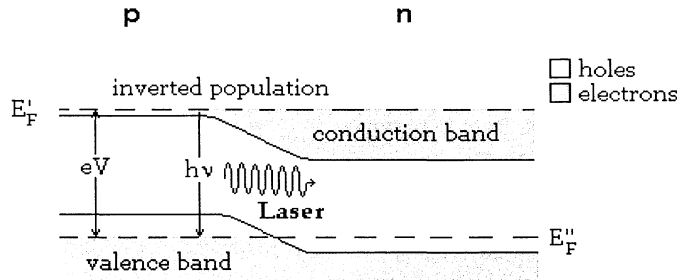
Figure 2.12: *The diode laser is the result of applying a voltage across a p-n junction (adapted from Refs [26, 27]).*

range for one particular laser is small, up to a few nm in best cases. There are diode lasers from the violet region up into the infrared region of the electromagnetic spectrum. The wavelength is determined by the size of the energy gap ($E = h\nu$) between the conduction and valence band seen in Fig. 2.12 and the size of the energy gap is determined from what materials the diode is manufactured from. The coarse tuning is done by changing the temperature of the diode, which corresponds to a change of the band gap. Swift scanning over small spectral regions is achieved by current ramping. An effect of this ramping is that the current and also the power out from the diode laser changes with the wavelength of the laser [26].

The crystal itself serves as the laser cavity. This is achieved by polishing two opposite sides of it, which make them act as mirrors. The light intensity is substantially increased by reflections back and forth through the laser medium. In order to obtain an external beam, one of the mirrors is partially transmitting light. The cavity works as a resonator which makes laser oscillation possible. A stable oscillation mode can only be achieved if there is constant constructive interference in the cavity. This occurs when an integer number of half wavelengths fit into the cavity of optical path length l. The mode separation $\Delta\nu$ is given by

$$\Delta\nu = \frac{c}{2l} \tag{2.64}$$

where c is the speed of light [26]. As the semiconductor laser has a very small optical path length (typically a millimeter) the mode separation is very large and thus only one mode may fit the cavity. Hence the semiconductor laser is frequently a single mode laser.

2.4 Wavelength modulation with lock in-detection

According to Fourier's theorem, any signal, noisy or clean, can be represented by a sum of sine waves with different amplitudes, phases and fre-

quencies. Therefore, a signal can be separated from others by knowing its frequency and phase. This is in principle what a lock-in amplifier does. By using a frequency and phase-sensitive detector, a signal can be measured in a noise-filled background. The method is based on signal modulation where the wavelength of the impinging light is modulated with a known frequency and the fact that noise, by definition, has no frequency reference [28]. As discussed in Chap. 2.3, diode lasers are very suitable light sources for wavelength modulation due to its uncomplicated wavelength tuning capability.
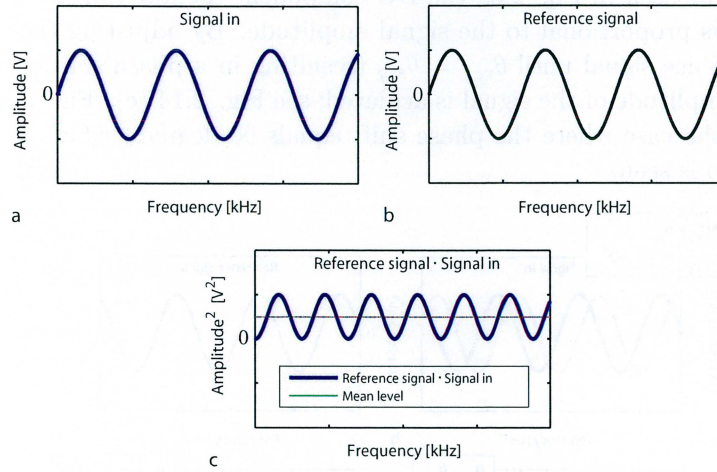
Figure 2.13: *Signal in, reference signal and their multiplication.*

At first, consider a noise-free sinusoidal signal (Fig. 2.13, (a)). The signal is repeated with the same frequency as a reference, which is done, for instance in absorption spectroscopy, by letting the reference signal control the wavelength modulation. This signal is described in Eq. 2.65 and the reference signal in Eq. 2.66.

$$S_{sig} = V_{sig} \cdot sin(\omega_{sig}t + \theta_{sig}) \tag{2.65}$$

$$S_{ref} = V_{ref} \cdot sin(\omega_{ref}t + \theta_{ref}) \tag{2.66}$$

The input signal (and any present noise) is then multiplied with the reference (Eq. 2.66).

$$
\begin{aligned}
V_{Multi} &= V_{sig}V_{ref}sin(\omega_{sig}t + \theta_{sig})sin(\omega_{ref}t + \theta_{ref}) \\
&= \frac{1}{2}V_{sig}V_{ref}cos([\omega_{sig} - \omega_{ref}]t + \theta_{sig} - \theta_{ref}) - \\
&\quad -\frac{1}{2}V_{sig}V_{ref}cos([\omega_{sig} + \omega_{ref}]t + \theta_{sig} + \theta_{ref}) \tag{2.67}
\end{aligned}
$$

The solution to the multiplication result in two AC signals, one having the frequency $\omega_1 = \omega_{sig} - \omega_{ref}$, the other $\omega_2 = \omega_{sig} + \omega_{ref}$. By using a low pass filter all AC components are removed, but if $\omega_{sig} = \omega_{ref}$ (illustrated in Fig. 2.13) the multiplication results in a DC component described in Eq. 2.68.

$$V_{Multi} = \frac{1}{2}V_{sig}V_{ref}cos(\theta_{sig} - \theta_{ref}) \tag{2.68}$$

As can be seen in Eq. 2.68 the DC component (denoted *Mean level* in Fig. 2.13) is proportional to the signal amplitude. By adjusting the phase of the reference signal until $\theta_{ref} = \theta_{sig}$ (resulting in a phase shift equal to zero) the amplitude of the signal is achieved; see Fig. 2.14 (c). Fig. 2.14 (d) illustrates the case where the phase shift equals 90 degrees, where a mean level of zero is seen.
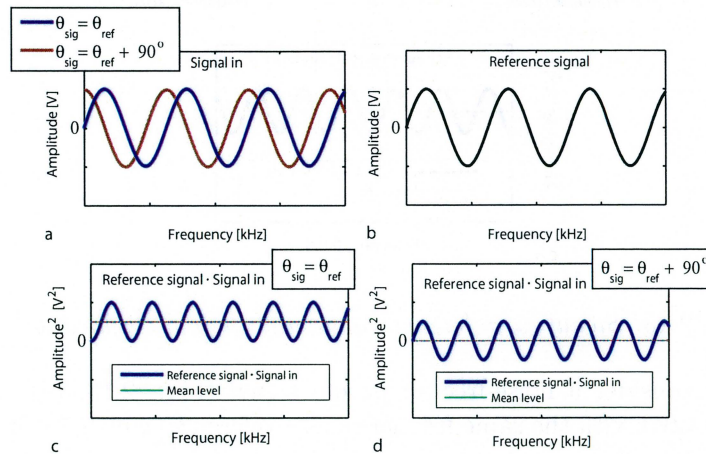
Figure 2.14: *(a) Signal in without a phase shift and with a phase shift of 90 degrees. (b) The reference signal. (c) The multiplication between the signal in (without phase shift) and the reference signal. (d) The multiplication between the signal in (with a phase shift) and the reference signal. As can be seen, the mean DC level is zero.*

In reality, no signal is free from noise, but since noise has no fixed frequency or phase relationship with the reference any multiplication between the two will not result in any change in the mean DC level. It should be noted that some noise exists with a fixed frequency, e.g. the 50 Hz background noise from the power grid. Such frequencies and their harmonics shall therefore be avoided. The signal-to-noise is even more improved if the reference frequency is chosen at high frequencies (limitation due to the capacity of the instrument lies around 100 to 250 kHz), since noise falls off at higher frequencies with a rate of $\frac{1}{f}$ [29].

2.5 GASMAS

GASMAS stands for GAs in Scattering Media Absorbtion Spectroscopy. This technique can be used to detect and in real time study the presence of gas dispersed in a scattering medium. The method has so far been used to investigate biological samples, such as fruit and wood [3]. It can also be used for medical purposes to detect gas inside human air cavities, such as sinuses [1]. So far only oxygen and water vapor has been investigated by the GASMAS technique [6] but in theory, any gas with absorption lines located within the tissue optical window ($600 < \lambda < 1300$ nm) is detectable using GASMAS. This chapter will discuss the theory behind GASMAS.

2.5.1 General GASMAS concepts

When illuminating scattering materials, the light propagates diffusely (see further Chap. 2.2.3), e.g. a pulse of light will be broadened in time due to different photon path lengths inside the media. The scattering of the light is due to inhomogeneities in the optical properties, such as the refractive index, of the medium [21, 30].

The concept of GASMAS is based on the difference in wavelength dependence of the absorption profile between free gases and liquids or solids, where the absorption lines of the two latter depend slowly on an incoming wavelength, unlike for free gases, which have 10 000 times more narrow absorption lines. The reason for solids and liquids having slow wavelength dependence is the influence of nearby atoms or molecules (see Chap. 2.1.1). If such a sample is illuminated, the outgoing radiation will therefore not vary if the frequency of the incoming light is slightly changed. However, should this sample contain small gas cells, randomly situated throughout the entire sample, a gas imprint will occur in the outgoing radiation if the frequency is varied in an interval covering one absorption line of the gas. This imprint will be seen as a sudden decrease in intensity, occurring at the light wavelength matching the absorption line. Hence, the higher concentration of gas situated inside the sample, the more will the intensity decrease. By using this technique on turbid materials one can actually use the scattering of light as an advantage, since the path length increases when light is scattered.

This has been studied using two different detection geometries; backscattering and transillumination. To explain the difference between the two detection geometries, a simple model consisting of two non-absorbing scattering materials, denoted S_1 (primary scatter) and S_2 (secondary scatter) is considered. The gas of interest is situated between S_1 and S_2. The model, which has been used to verify the GASMAS method, as applied to the sinus cavity case [1], is illustrated in Fig. 2.15. To simplify, all dimensions apart from the thicknesses of the scatterers, are considered to be infinitely large.
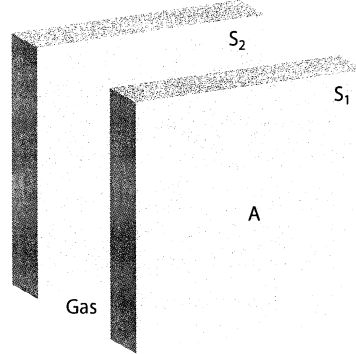
Figure 2.15: *The model used to describe the transillumination and backscattering technique. Light is, in both cases, sent in at position A.*

2.5.2   The transillumination detection technique

When the primary scatter is illuminated at position A light will propagate diffusely. Some is directly or diffusely reflected while the remaining light will exit the back of S_1, where it will follow a straight line, with a certain angle to S_1, towards the front of S_2. In this region the intensity of light will decrease according to the Beer-Lambertian law (Eq. 2.15). Inside S_2, the light can either backscatter to once again pass the gas or propagate toward the back of S_2 where the light is detected. The great advantage when using this measurement geometry is that all light reaching the detector has passed the gas filled gap in between S_1 and S_2, thus creating a good signal-to-background ratio. If the distance between the two plates is increased, the amount of absorbed photons increases, giving rise to a higher GASMAS signal. The disadvantage is when the scattering coefficient or the thickness of the primary and the secondary scatter becomes too large. If this occurs the amount of photons reaching the detector is heavily reduced, resulting in a low signal-to-noise ratio. When facing this problem, the backscattering technique could be used instead.

2.5.3   The backscattering detection technique

As previously mentioned, the backscattering geometry could be an alternative detection geometry, when the dimensions of the samples become too large for any photons to be transmitted. An example is when trying to investigate the oxygen content in the frontal sinuses, where no transillumination is possible.

When using this technique the source and the detector are located on the same side of S_1. The main difference from the transmission technique is that not all photons reaching the detector have passed the gas filled gap in between S_1 and S_2, giving rise to a reduced signal-to-background ratio. To

improve the signal an absorbing detection aperture can be used to remove photons that are directly backscattered, the so-called shortcut photons. This is based on the fact that photons that are detected at a large radius from the illumination point have a higher probability of having traveled deeper into the sample, which is illustrated in Fig. 2.16. The problem that occurs is the loss of flux, and thus a need for an optimized detection aperture exists.
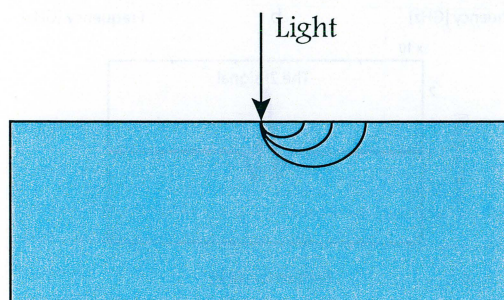

Figure 2.16: *Radial dependence of sampling depth. By moving towards larger radii the sampling depth becomes greater, but with the cost of loosing flux.*

An advantage when using the backscattering technique in the model in Fig. 2.15 is that all photons that have passed the gas must at least make a double pass, which improves the signal.

Note that the model discussed above is merely to explain the basic concept of the GASMAS technique. Experiments on porous materials, such as wood, fruit and powder have been performed [3]. These materials are ideal for investigation with the GASMAS method, since they contain free gas cells randomly distributed throughout the material. Since the path length inside a scattering material increases with increasing scattering coefficient μ_s (if one neglects direct backscattering), the probability of a photon passing through such a gas cell gets higher and thus the absorption signal, the imprint from the gas, also gets stronger.

2.5.4   Utilizing a lock-in amplifier in GASMAS

To be able to measure the gas content when the absorption signal is very weak, wavelength modulation spectroscopy with lock-in detection can be used, see Chap. 2.4. Fig. 2.17 (a) shows the direct signal S_{Dir} where the decrease in intensity due to gas absorption can be seen.

When utilizing the lock-in amplifier the wavelength is scanned across the absorption line with a repetition rate of a few Hz. By superimposing an additional sinusoidal component in the kHz-region onto the current ramp sensitive wavelength modulation spectroscopy (WMS) can be done. This will produce the so called 1f-signal, i.e. the derivative of the direct signal (see Fig. 2.17 (b)).
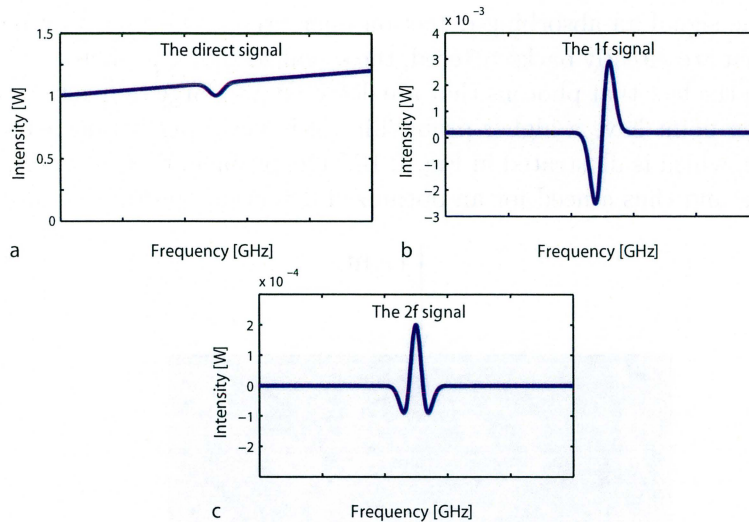
Figure 2.17: *(a) The direct signal measured by wavelength scanning. The small decrease in intensity is due to absorption of the gas. (b) The 1f-signal (the derivative of the direct signal). (c) The 2f-signal (the second derivative of the direct signal).*

Instead of using the 1f-signal, the second harmonic at twice the fundamental modulation frequency can be studied, denoted the 2f-signal (see Fig. 2.17 (c)), i.e. the second derivative of the signal. By doing this the maximum of the signal is located at the same frequency as the absorption maximum.

2.5.5   Experimental data analysis - Standard addition

To avoid confusion it should be noted that the value received when using the GASMAS method is not an absolute value of the gas concentration inside the sample, since this depends on the sampled path length. To know this volume, the scattering coefficient μ_s must be measured, which is not possible with the GASMAS setup today.

To evaluate the gas content of a sample the peak-to-peak value of the 2f-signal (S_{2f}), is measured (see Fig. 2.18 (b)). The amplitude of this signal is both dependent on the absorption due the gas inside the sample and on the amount of light reaching the detector. Hence, by normalizing the signal with the total amount of light reaching the detector (S_{Dir}), compensated for the background, a measure of the absorption due to the gas is received. This measure is called the GMS (GASMAS measurement signal), $GMS = \frac{S_{2f}}{S_{Dir}}$.

To calibrate the GMS value obtained into a more meaningful quantity a method called *standard addition* is used. This method is commonly used

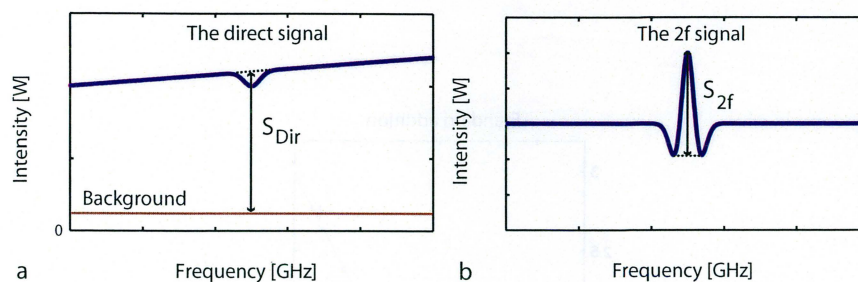Figure 2.18: *The direct and the 2f-signal with indications of the S_{Dir} and S_{2f} which is used to achieve the normalized GASMAS signal GMS.*

in analytical chemistry when the concentration of an unknown substance is investigated. By adding volumes of a substance with a known concentration to the substance and measure the reduction in intensity of the transmitted light, the concentration can be found. The only requirement is that the Beer-Lambert law (Eq. 2.15) can be rewritten as a linear relation between absorption and intensity, described in Eq. 2.69, which is true if the absorption is small.

$$I_t = I_0 \cdot e^{-\mu_a \cdot z} \approx I_0 \cdot (1 - \mu_a \cdot z) \tag{2.69}$$

In chemistry, the geometrical path length is well defined (the thickness of the cuvette) unlike the samples investigated using GASMAS. In this case the additional path length is added outside the sample. By simply moving the source away from the sample, an added path length of absorbing gas can be added. In the case of this report where the gas of interest is oxygen, ambient air is used [31], thus creating a well-defined added path length of oxygen. Due to this added path length of oxygen the intensity will decrease, resulting in an increased GASMAS signal. By repeating this for different added lengths and by extrapolating the graph obtained to the intersection between the curve and the x-axis, representing added air, the equivalent mean path length in oxygen can be found, i.e. the mean distance light has to travel through ambient air to obtain the same signal as in the sample. Hence $\langle L_{Sample} \rangle \langle c_{sample} \rangle = \langle L_{eq} \rangle \langle c_{air} \rangle$.

To get a high signal, the exponential in Eq. 2.69 must be reasonably large, but not to large. Thus, if the path length z [m] inside the medium is large the only way to fulfill Eq. 2.69 is to study a gas with a low μ_a [m^{-1}].

Experiments have been done on various porous media (see Table 2.1) using standard addition to estimate the equivalent mean path length [3]. As can be seen in Table 2.1 the equivalent mean path length is usually longer than the geometrical thickness of the sample but it should be noted that it also can be shorter as can be seen with epoxy.
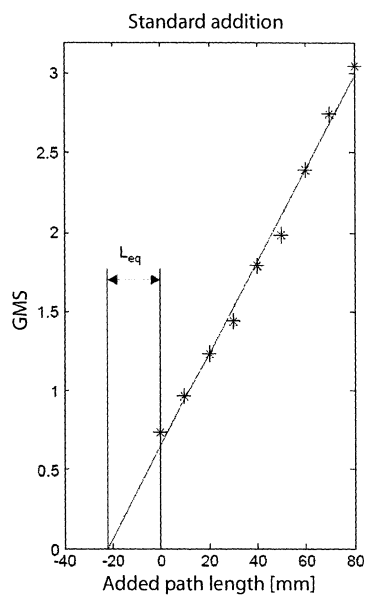
Figure 2.19: *Illustrating the standard addition method. The extrapolation shows an equivalent mean path length slightly above 20 mm [32].*

Material	Thickness (mm)	Equivalent Mean Path Length (mm)
Wood	10	123
Apple	26	33
Lump sugar	12	20
Granulated salt	18	170
Wheat flour	18	380
Polystyrene foam	19	600
Turbid epoxy	19	5

Table 2.1: *Shows different measured equivalent mean path lengths for different samples [3].*

2.5.6   Static and dynamic measurements

There are two different approaches to study samples with the GASMAS set-up. A static measurement can be obtained and compared with other absolute values of different samples. Sometimes this is very difficult since, as mentioned before, the obtained result is the so-called L_{eq} which depends on both the scattering coefficient and the concentration of the gas. Instead a dynamic or diffusion measurement can be performed, where the change in the signal is studied. An example of how a dynamic measurement can be performed, is by letting some gas, like molecular nitrogen, diffuse into the otherwise air filled cells (e.g. a sinus cavity). During this gas exchange a decrease in the GASMAS oxygen signal can be seen [1]. The opposite could as well be studied by first letting the sample be immersed with e.g. nitrogen gas and study the re-invasion of oxygen [32].

2.6   The human sinuses

Sinuses are air-filled cavities located in the cranial bones. They, like the nasal cavity and the lungs, are covered with small hair-like filaments called cilia and serve as protection to the airways by trapping germs and irritants. These cavities are also covered with mucous, which in combination with the movement of the cilia keeps the body free from bacteria, pollen, irritants to name a few. The sinuses also help the lungs by moistening and warming the inhaled air [33]. Sometimes it is even claimed that one of the sinus purposes is to make the head lighter [34].

There are three major sinuses: sinus frontalis, maxillaris and sphenoidalis (see Fig. 2.20) and all are connected to the nasal cavity, where they are drained of mucous. This connection is called the nasal ostium. The frontal sinus is located approximately one centimeter behind the eyebrows on an adult person and can be either bilateral or consist of only one single cell. The shape and depth varies from person to person but the dimensions for an ellipsoidal bilateral frontal sinus lies around $20 \times 25 \times 10$ mm. The maxillary sinus is always bilateral and are located beneath the cheek bone above the oral cavity. The sphenoidal sinus, which consist of one single cavity, is approximately located in the center of the cranium [35].

In Fig. 2.20 the sinus ethmoidalis cells are also shown. The ethmoidal sinuses consist of many very small (compared to the other major sinuses) air cells.

2.6.1   Sinusitis

Inflammations in the sinuses often occurs as a consequence of having a cold, where the virus attacks the sinuses, causing a production of fluid. This reaction can block the connection between the sinuses and the nasal cav-

Ethmoid sinuses

Frontal
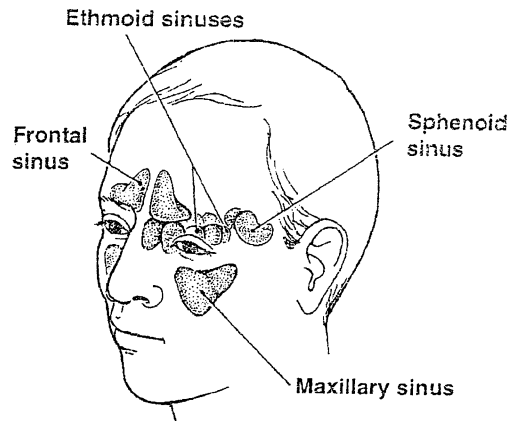sinus

Sphenoid
sinus

Maxillary sinus

Figure 2.20: *The human head with indication of the human sinuses. (Figure from [36]).*

ity, causing a buildup of liquid, which is an ideal environment for bacterial growth. Normally, these bacteria are washed away by the cilia but the production of pus reduces their movement. This condition is known as sinusitis and over 37 million people per year in the USA suffer from severe sinusitis attacks [2].

If one suffers from sinusitis the body gets weakened since the cilia in the sinuses will no longer keep the body free from other infections. The disease is treated with antibiotics and although most patients respond to this treatment there is always the risk of developing antibiotic resistance, i.e. reducing the effect of this treatment on infections that occur later in life [9].

Symptoms of sinusitis are facial pain, thick discolored mucous, fever, headache, toothache, fatigue, cough, bad breath among others. In extreme cases of sinusitis the infection might even be spread to the brain [37].

2.6.2   Diagnostics

To diagnose sinusitis there are today three methods; clinical examination, ultrasound and radiography [9]. The most accurate method is radiography where either computer tomography or X-ray of the sinus cavities is performed. These examinations are both very expensive and not without health risks. The most common diagnostic method is clinical examination. Unfortunately, other nasal complaints share many of the symptoms for acute sinusitis so misdiagnosis and over-treatment is believed to be common. This can lead to unnecessary resistance development against the antibiotic [9]. Since all the current methods are either unsafe or not satisfyingly accurate

there is a great need for optional examinations. The GASMAS method might be such an alternative.

2.6.3   Diagnostics using GASMAS

Sinusitis causes the sinuses to fill with mucous and block the nasal ostium, which prevents air flow through the sinuses. This can not be investigated with a clinical examination, but with the GASMAS method this would be possible to do non-intrusively. By letting the patient inhale fortified oxygen and study the GASMAS-signal, using either the backscattering technique to study the frontal sinus or the transmission technique to study the maxillary sinus, an increase in the signal will be seen if the airways are free but none if the airways are closed. This experiment has been performed using the backscattering technique with phantoms of Delrin. Air situated between two Delrin plastic plates (primary scatter $l_1 = 3$ mm, secondary scatter $l_2 > 30$ mm, air gap $d = 8$ mm) was replaced by a different gas mixture resulting in a 33 % reduction in the signal [1].

Chapter 3

Simulations and measurements

To be able to compare the experimental data [1] with the simulated data, values of the optical properties, μ_s, μ_a and g are required. These parameters were described in more detail in Chap 2.2.1. The material used in the study was white Delrin-type plastic with an estimated reduced scattering coefficient of 2 mm^{-1}. This choice of Delrin mixture makes the plastic similar to human tissue [38], but the variation of optical parameters for human tissue makes it impossible to represent human tissue with one given set of optical parameters. The aim of the study was to show the response in the GAS-MAS signal due to different layers of air between two Delrin-plates (both transillumination and backscattering measurements were investigated).

According to a study made on Delrin by the Linköping Biomedical Optics Group [39] the optical parameters are $\mu_s = 18\ mm^{-1}$, $\mu_a = 0.0017$ mm^{-1} and g = 0.87 but the result vary for different mixtures. To further investigate the optical properties of the Delrin plates used, measurements using the integrating sphere technique and time-resolved measurements were performed.

3.1 The ASAP$^{\text{TM}}$ software

There exist a large variety of software for analyzing light propagation. Of these softwares few are able to handle volume scattering, which is probably due to the very recent progress made in this field. Because of the technical development of more powerful computers many of the existing simulation programs were reconstructed, going from sequential to non-sequential ray tracing. Sequential ray tracing is when the program only traces the photons that follow a pre-determined path. By ignoring other rays the time of tracing is reduced, while all rays are traced when using non-sequential ray tracing, a requirement when simulating scattering media.

ASAP$^{\text{TM}}$ is one of the leading light simulation programs, handling non-sequential ray tracing, able to simulate biological systems, thus well suited for this project. Although many similar programs exist the choice of ASAP$^{\text{TM}}$ was not due to any differences in capability with respect to other programs. A generous offer from Breault Research, Tucson, Arizona, allowed the Applied Molecular Spectroscopy Group at the Atomic Physics Division at Lund Institute of Technology to use the program for a year free of charge.

3.1.1 The interface

When using ASAP$^{\text{TM}}$, the objects are created with a script language (advanced users) or a less powerful user-friendly builder (for beginners), where the user more or less is told which parameters to define. No visual geometry control is directly shown when objects are added to the model. The total script must be compiled to achieve a visual image of the created model. The script concept is a powerful way to control the model once the user has enough knowledge of the language. An example of the ASAP$^{\text{TM}}$ script is shown in Fig. 3.1, displaying a script for a simple model of a sinus together with the image of the created model.

```
SYSTEM NEW
RESET

UNITS MM 'mW'
WAVELENGTH 760 NM

LEVEL 2E9

COATING PROPERTIES
    0 1 'TRANSMIT'
    1 0 'REFLECT'
    0 0 'ABSORB'

MODEL
    VOLUME 0.99 1E-9`2E-5 1
MODEL
    VOLUME 0.93 16 1

MEDIA
    1.0 'AIR'
    1.53 'SCHOTT'
    1.49 'PLEXI'
    1.0 SCATTER .2 'OXY'
    1.48 SCATTER .1 0 1 10000000 10000000 'DELRIN'

FRESNEL TIR

SPLIT 10 MONTECARLO

HALT 1000 1E-6


ENT OBJECT
    ELLIPSOID 15 20 15 0 0 16 'SINUS'
    INTERFACE COATING BARE DELRIN AIR
    REDEFINE COLOR 24

EMITTING DISK Z 0 0.3 0.3 10 10 10
    FLUX TOTAL 2

WINDOW Y Z
PLOT FACETS 10 10 OVERLAY

TRACE PLOT
```

Part 1

Part 2

Part 3

Figure 3.1: *Example of the ASAP$^{\text{TM}}$ script language. Three different parts are indicated, where part 1 contains definitions, part 2 the geometry and location of the model, and part 3 the ray tracing.*

The script concept is divided into three groups also indicated in Fig. 3.1. The first part starts with defining parameters, such as wavelength, units, materials and so forth. The second part contains the geometry of the

model, where every element is defined by its location, mathematical shape and dimensions. The last part handles the light sources, the ray tracing and the analysis.

3.1.2 Rays and ray tracing

Sources may have any shape, and consist of a user-defined number of rays. There is also the possibility to produce a desired beam profile, such as a Gaussian or a Lorentzian [40]. A ray should not be confused with a photon, carrying a quantum of energy. It should instead be considered as built up by many photons. The difference is that if a photon is absorbed all energy is lost, while in the case of a ray a percentage of the energy may be absorbed. By doing this and thus allowing the ray to survive longer a better reality resemblance is achieved (see further Chap. 2.2.4). The default value for ray termination is when the weight of the package is reduced to 10^{-6} of the original value, but this can be defined by the user [41].

When a ray has passed a surface it is denoted as though it belongs to the surface (or the surface number) and does so until passing the next surface. This is how ASAP^{TM} keeps track of rays and how the tracing results are presented. Fig. 3.2 shows an example of how the ray tracing of one ray is presented in ASAP^{TM}.


```
 Object number              Coordinate                    Flux

 --- HISTORY LIST                                          !!
 Ray 1
    Object        X           Y            Z              Flux
    1.0000  -6.673533     0.7831945    -10.70000        -.48657
    2.0000  -6.610276     0.7101154    -10.60000        -.48657
    3.0000  -5.609207     -.4464021    -7.600000        -.48657
    5.0201  -5.545950     -.5194814    -7.500000        -.48657
    5.0601  -2.094978     -4.506329    2.500000         -.48657
    7.0000  -2.031721     -4.579408    2.600000         -.48657
    8.0000  -1.968464     -4.652487    2.700000         -.48657
    9.0000  -1.276071     -3.619487    5.700000         -.49263
    9.0000  1.443569      -.7719370    5.700000         -.49624
   12.0000  0.2143912     -3.437829    10.70000         -.49630
   12.0000  0.2228222     -3.507510    10.70000         -.49632
   12.0000  0.2266966     -3.536226    10.70000         -.49633
   12.0000  0.8024626     -3.044588    10.70000         -.49717
    9.0000  0.8302016     -1.912183    5.700000         -.49723
    9.0000  0.7481408     -1.685477    5.700000         -.49732
    9.0000  0.8965628     -.9026272    5.700000         -.49765
    9.0000  1.267130      -.7763247    5.700000         -.49776
    9.0000  1.643404      -.7816795    5.700000         -.49786
    8.0000  0.1873332     -.3671769    2.700000         0.50000
    7.0000  0.1856598     -.3591085    2.600000         0.50000
    6.0300  0.1839863     -.3510401    2.500000         0.50000
    6.0200  0.1398380     -.1381809    -.1381809        0.50000
    6.0100  0.1003143     -2.500000    0.5238042E-01    0.50000
   -0.0000  0.9529399E-01 -2.800000    0.7658565E-01    0.50000
 --- $IO OUTPUT CLOSE
```

Figure 3.2: *Example of how ASAP^{TM} presents ray tracing. The coordinate and flux are given for each object number.*

3.1.3 Modeling a volume scatterer

To perform volume scattering in ASAP^{TM}, the user must define the scattering parameters (μ_s and g). Absorption can also be added, but is by default zero. Fig. 3.3 illustrates where and how these parameters are added in the

ASAP™ script (defined in part 1 according to the denotation in Fig. 3.1). As can be seen, the scattering medium (in the shown example *DELRIN*) has a maximum number of scattering events set to 10 000 000. This value is of great importance, because if that value is reached by any ray, it will no longer scatter but instead follow a straight path until leaving the model. The absorption and scattering coefficients are multiplied with the fractional obscuration, which can be set to 1 to avoid confusion.

Figure 3.3: *ASAP™ script for volume scattering.*

It is also important to define how ASAP™ traces the rays. In this case Monte Carlo is used (see further Chap. 2.2.4 for more Monte Carlo ray tracing) but it is also possible to not use the Monte Carlo command and instead let the rays split due to the Fresnel reflections. These specular reflections are not accounted for when using the Monte Carlo command [42].

The modeling of a volume scatterer described above uses Monte Carlo simulation and the Henyey-Greenstein model, an alternative is to use the Mie particles model, where random scattering spheres are distributed throughout a volume [42].

3.1.4 Analyzing the data using Matlab

The ray tracing result given by ASAP™, which is shown in Fig. 3.2, must be analyzed, which, in this case, has been done using Matlab. To explain how this analysis is done, consider the ray shown in Fig. 3.2 (ray from script in appendix C). To be able to follow the ray tracing the model used in this simulation is shown in Fig. 3.4.

The information given by ASAP™ should be read backwards, i.e. the ray is created in the light source (object number 0), passes the prism (object numbers 6.01, 6.02 and 6.03). Thereafter the ray passes through the control surface (object number 7) and enters the primary scatter S_1 (object number 8) where it is scattered. Note, that how the rays are scattered in the primary scatter is not given by ASAP™, since the information would then become
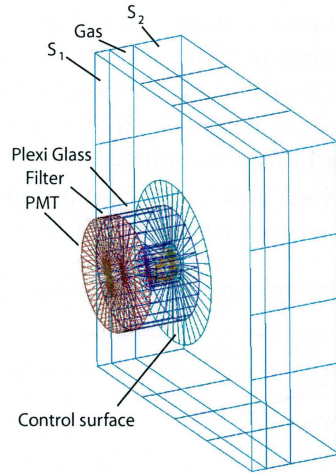
Figure 3.4: *Model used for ray tracing of phantom measurement in the backscattering geometry.*

overwhelming. After propagating diffusely the ray finally reaches the back of S$_1$ (object number 9) where it is reflected a few times. When exiting this object the ray follows a straight line reaching the front of the secondary scatter (object number 12) where it, after two reflections, leaves S$_2$ to once again enter S$_1$. When the ray exit the primary scatter it once again passes the control surface, which purpose is to later on find the exit coordinates. This is of importance since the control surface will act as an absorbing detection aperture, when analyzing the data Matlab. After this, the ray passes through the plexi glass (object numbers 5.0601 and 5.0201), through the filter (object numbers 3 and 2) and is finally absorbed in the photomultiplier tube (object number 1). A closeup of the ray tracing is shown in Fig. 3.5. All four rays used in the simulation are plotted, but note that only the one reaching the detector is given in the result.

After sorting away the unwanted text information, Matlab is programmed to find the object numbers of interest, which in this case are 1, 7, 9 and 12. Since the only rays that are of interest are the ones reaching the detector, ASAP^{TM} is (in before hand) told to neglect all other rays, saving time for data analysis.

The aim of the simulations is to calculate the so-called L_{eq}, which is the average length the detected rays have traveled in the air gap, according to Eq. 3.1, which represents one passage through the air gap. This calculation is then repeated for the second passage and the results are added. Matlab is also told to control whether multiple passages occur and add them to L_{air}.

$$L_{air}^{(1)} = \sqrt{(X_{12}^{(1)} - X_9^{(1)})^2 + (Y_{12}^{(1)} - Y_9^{(1)})^2 + (Z_{12}^{(1)} - Z_9^{(1)})^2} \qquad (3.1)$$
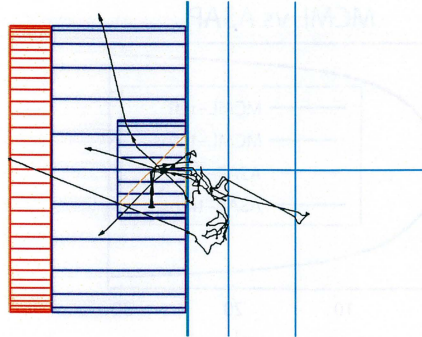
Figure 3.5: *Illustration of ray tracing in the model shown in Fig. 3.4.*

In this equation, the denotation [1] is used to indicate the first passage and [12] or [9] indicates the object number. The L_{air} for all rays, together with the coordinates for the control surface and the flux ϕ when reaching the PMT are stored. The equivalent mean path length is then calculated according to Eq. 3.2.

$$L_{eq} = \frac{\sum (L_{air} \cdot \phi_{ray})}{\sum \phi_{ray}} \tag{3.2}$$

where ϕ_{ray} stands for the flux of each ray when reaching the PMT.

3.2 MCML

To control the output from ASAP$^{\mathrm{TM}}$, it is compared with the output from another software, called MCML (Monte Carlo for Multi-Layered media), commonly used for Monte Carlo simulations of scattering media [43]. As the name tells, this software also uses Monte Carlo simulations. The division has used this program for several years. A simple model was used in this comparison. A slab geometry is built up with the same optical properties in both softwares. The fractions that are being transmitted, diffusely reflected, specularly reflected and absorbed are compared. The model in ASAP$^{\mathrm{TM}}$ has a finite size in radial direction and the MCML model is infinitely large in the radial direction. To be able to compare the results, an approximation has to be done. The fraction of the flux going through the sides of the ASAP$^{\mathrm{TM}}$ model is simply added to the diffuse reflectance as it is not followed any longer, though some of it should have been added to the transmittance instead. As the ASAP$^{\mathrm{TM}}$ model is large (a width of 10 cm) in the radial direction, the fraction of the flux transmitted through the sides is very small, which makes the error very small. The ASAP$^{\mathrm{TM}}$ model uses absorbing surfaces that detects all light leaving the plate. The comparison is made for different scattering coefficients, as shown in Fig. 3.6. As seen the two Monte Carlo simulation programmes provide very similar results.
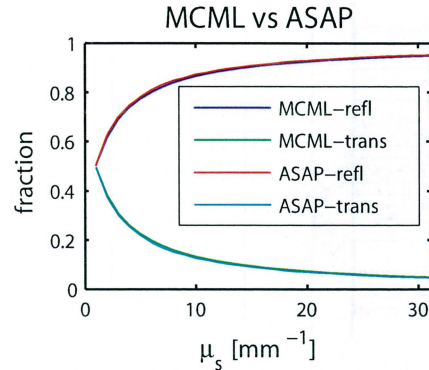
Figure 3.6: *Comparison between ASAP^{TM} and MCML for different scattering coefficients.*

3.3   Integrating sphere

The concept of the integrating sphere technique is fairly simple and results in the complete set of optical parameters; scattering and absorption parameters (μ_s and μ_a) and the anisotropy factor g. Results from the measurements are compared with a Monte Carlo simulation database (Monte Carlo simulation is described in more detail in Chap. 2.2.4). When performing light propagation simulations based on the Monte Carlo method, transmitted and diffusely reflected light for a given set of optical parameters and sample thickness are obtained. The integrating sphere technique is the exact opposite, measurements give values of transmittance and reflectance. The optical parameters are then received by finding the best match between the measurements and the Monte-Carlo database [44].
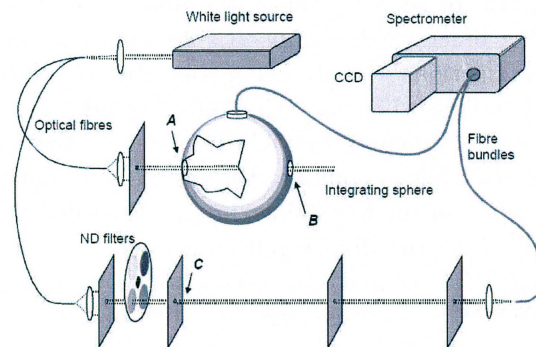

Figure 3.7: *The experimental setup of the integrating sphere technique. (Figure from Ref. [44]).*

3.3.1 Integrating sphere theory

The integrating sphere consists of a sphere with a diameter of 20 cm with highly reflecting barium sulphate covering the inside surface. By placing the sample of interest in position A (see Fig. 3.7) the transmitted light I_T is collected, neglecting other losses except reflection and diffusive reflection, which both are measured by placing the sample in the position B. The reflectance and transmittance are determined by Eq. 3.3 and 3.4 [44].

$$R = R_{BS} \cdot \frac{I_R}{I_{ref}} \qquad (3.3)$$

$$T = \frac{I_T}{I_{ref}} \qquad (3.4)$$

where I_R is the reflected intensity measured when the sample is placed at position B, I_{ref} the reference intensity measured without any sample. R_{BS} is the reflectance factor for the barium sulphate plug which must be placed at position B when measuring the transmitted light. To receive the complete set of optical parameters, the total interaction coefficient μ_t must also be measured, which is performed with a collimated light measurement. By measuring the intensity of the light that passes straight through the sample, a comparison with the Beer-Lambert law (Eq. 2.15) can be done giving a value for $\mu_t = \mu_s + \mu_a$. This intensity is described according to Eq. 3.5.

$$I_{col} = \frac{I_0 \cdot e^{-(\mu_a + \mu_s) \cdot d}}{T_{ND}} \qquad (3.5)$$

where I_{col} is the detected intensity, I_0 the intensity of the laser and T_{ND} is the transmittance of a neutral density filter (denoted ND filters in Fig. 3.7). The latter is used to attenuate the light in the reference measurement, to decrease the requirement of the dynamic range of the detection system [44].

3.3.2 Databases used for evaluation

Although the whole set of optical parameters are provided using the integrating sphere, there is still the question of the validity of these values. Since both the transmittance and the diffuse reflectance depend on the thickness of the sample a slight error in this value will thus change the result. This error is relatively small when using liquid samples but since the measurements were performed using Delrin plastics, this effect must be considered. The reason for this is due to the possibility to have a more accurate measured sample thickness should it be a liquid. Also, the smoothness of the plastics will effect the results. The ideal situation is when the sample is cut to be completely smooth, which unfortunately is very difficult. The measurements were compared with two different databases, according to Table 3.1:

Database	Range of μ_s $[mm^{-1}]$	Range of μ_s' $[mm^{-1}]$
Epoxy database [45]	[0.001-0.05]	[2.5-20]
"Nazila database" [46]	[0.001-1]	[0.3-50]

Table 3.1: *The two databases used to compare the results given by the integrating sphere technique.*

As can be seen, the databases are not optimized for the Delrin plastics (assuming that the results from Linköping are correct). If one considers only absorption (μ_a), which in the case of the Delrin plastics is approximately zero, the epoxy database would be able to find a good match, whereas the match with the "Nazila database" might be slightly more inaccurate. If one instead considers scattering (μ_s'), it is the opposite (since $\mu_s' \approx 2.34$) where the "Nazila database" might be able to find the best match. The best result expected using the epoxy database would be $\mu_s' = 2.5$ mm^{-1}, which deviates by 6.4 % (as compared to the value given by the Linköping group [39]). Therefore the result from the "Nazila database" was used.

3.3.3   Results from the integrating sphere

The optical parameters obtained with the integrating sphere technique in the case when using both the epoxy database and the "Nazila database" are shown in Table 3.2.

Database	g	μ_a $[mm^{-1}]$	μ_s $[mm^{-1}]$	μ_s' $[mm^{-1}]$
Epoxy database	0.87	-0.2	14	1.8
"Nazila database"	0.9	-0.3	14	1.4

Table 3.2: *The results of the optical properties from the integrating sphere measurement.*

The fact that both absorption coefficients are negative is due to the very small absorption in the Delrin plates ($\mu_a \approx 0$) which cannot be measured more accurately due to the absorption ranges of the databases.

3.4   Time-resolved measurement

Time resolved measurements were also performed, to find the correct optical parameters for the Delrin plastic plates. The concept is based on pulse broadening and by iterations finding the optical parameters μ_a and μ_s' that will reproduce the same shape of the measured pulse. As previously mentioned, a pulse will be broadened in time when propagating in a scattering media, such as tissue (see Fig. 3.8). The shape of the broadened curve can be described according to the diffusion equation (Eq. 2.42) where the

absorption coefficient μ_a will determine the final slope of the curve whereas the reduced scattering coefficient μ_s' will determine the rising edge. This is due to that photons that are detected later in time have traveled a greater distance in the tissue sample making the probability of photon absorption higher. If the scattering coefficient is high the pulse will be more broadened than if it is low and thus μ_s will therefore determine the slope of the pulse around its maximum.
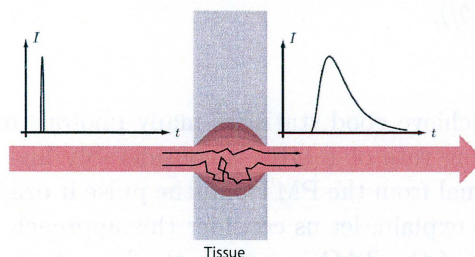

Figure 3.8: *Pulse broadening due to scattering in tissue. (Figure from Ref. [47]).*

3.4.1   Instrumentation

If using time resolved measurements no restrictions are made on the measurement and can be either transillumination, reflectance (backscattering) or interstitial (where an optical fibre is inserted into the sample). The technique used is *time-correlated single photon counting* (TCSPC), which is a very sensitive technique, based on statistics. A short pulse is sent into a sample and is detected using a photomultiplier tube (PMT). When the PMT detects a photon a signal is sent to a *constant fraction discriminator* (CFD), which improves the timing of the system and also reduces noise. Thereafter the signal is sent to a *time-to-amplitude converter* (TAC), which can measure the time difference between two signals. When the signal reaches the TAC an internal clock starts and runs until the next pulse is fired. This time difference is converted into an electrical pulse, having an amplitude proportional to the time interval and sent to a *multi-channel analyzer* (MCA). Every voltage (proportional to the time difference) of the incoming signal corresponds to a channel in the MCA and increases the counts in that channel by one. To receive good statistics this procedure is repeated thousands of times, resulting in a histogram of the broadened pulse. A schematic view of the system is shown in Fig. 3.9 [47].

The reason why the signal received by the PMT is compared to the next laser pulse and not by the laser pulse itself is due to the finite sampling rate of the TAC (1 MHz). This is because the TAC requires 1 μs to start,
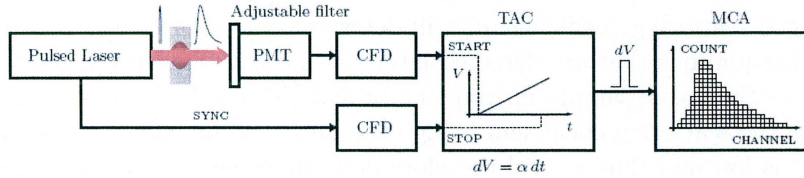
Figure 3.9: *Schematics of the time-correlated single photon counting system. (Figure from Ref. [47]).*

stop and reset. To achieve good statistics many photons must be detected and even if a sampling rate of 1 MHz is considerably high, measuring the time between the signal from the PMT and the pulse it originate from has a major drawback. To explain, let us consider this approach. Since the maximum sampling rate of the TAC is 1 MHz the largest number of photons measured per second is one million. This holds, if, for each fired pulse, one photon is detected by the PMT and one must therefore increase the flux of the laser until the possibility for photon detection is close to one. This will unfortunately lead to that photons arriving later almost never are detected, resulting in a false histogram of the pulse. One could, to avoid this, decrease the flux of the laser, making the possibility for photon detection much less than one. Now photons arriving late or early will have the correct possibility to be detected (naturally, photons arriving later has a lower possibility to be detected since fewer survive) and the correct histogram is achieved. Unfortunately, by doing this, the TAC has to start, stop and reset many times without ever a photon being detected, leading to unnecessary wear to the TAC and a low number of photons detected per second. If instead, the signal is compared in time relative to next laser pulse, not only will the TAC not start in vain but the full repetition rate of the laser could be used (roughly 40 MHz). Since this technique is used for medical applications [48], a low measuring time is important and by using the full repetition rate of the laser this is reduced.

3.4.2   Results from the time resolved measurement

As mentioned above, only the reduced scattering coefficient μ'_s and the absorption coefficient μ_a is received using time resolved measurements. The result for the reduced scattering coefficient was $1.1 < \mu'_s < 1.15 \; mm^{-1}$ and for the absorption coefficient $0.0005 < \mu_a < 0.0006 \; mm^{-1}$. Using the value for the anisotropy factor g from the measurement performed in Linköping (g = 0.87) gives a scattering coefficient $8.46 < \mu_s < 8.85 \; mm^{-1}$.

3.5   Experimental GASMAS set-up

The experimental set-up described in Fig. 3.10 was used in the experimental measurements. A near infrared single mode diode laser, Sharp LT031MDO, was used as a spectroscopic light source during the experiments. It had a nominal output power of 7 mW, and the power used during the measurements was about 2 mW, due to the current ramping; see Chap. 2.3. The laser driver current was ramped at a repetition rate of 4 Hz, to wavelength tune the diode laser over the R7R7 molecular oxygen line, at 761.003 nm (vacuum wavelength); see Chap. 2.1.2.

A 9 kHz sine-wave was superimposed on the current ramp to achieve sensitive wavelength modulation spectroscopy with lock-in detection. It relies on the detection of a known frequency among others, to reduce noise, see Chap. 2.4. A phase-sensitive detector is used to extract the frequency of the signal from the noise, by comparing the frequencies to a reference frequency.

The light from the diode laser was focused into a multi-mode optical fibre with a core diameter of 600 μm. To get the light into the backscattering geometry a right-angle BK7 prism was used, which was placed in front of the fibre and over the center of the detector. Due to total internal reflection in the prism, all light will enter the sample without having the fibre blocking the detector; see Fig. 3.10. In the transmission geometry the fibre was placed above the sample, and the detector was positioned under the sample. In both geometries circular apertures, were used; see Fig. 3.11. The detection aperture was about 5 mm for the transmitting sample; see Fig. 3.11 (b). For the backscattering sample a detection aperture with an inner radius r_i of about 5 mm and an outer radius of about 21 mm, as seen in Fig. 3.11 (a).

The detector used was a photomultiplier tube (PMT), Hamamatsu 5070A. A glass filter, SchottRG715, used to block out the background light, was placed in front of the photomultiplier.

The signal from the PMT was divided into two parts. One signal was going direct to the oscilloscope, the direct signal, and one, referred to as the WMS signal, was going via a lock-in amplifier, EG&G Princeton Applied Research 5209. The lock-in amplifier provides phase-sensitive detection at twice the modulation frequency (18 kHz), making the lock-in signal look like the second derivative of the input signal; see Chap. 2.4. The amplitude of the WMS signal is determined by the absolute absorption, that is the fractional absorption due to the gas and the amount of light reaching the detector.

The peak-to-peak value of the WMS signal, normalized with respect to the total amount of light reaching the detector, gives an estimation of the absorption due to the air. At small gas absorptions the WMS signal is proportional to the absorbance, and therefore also to the product of gas
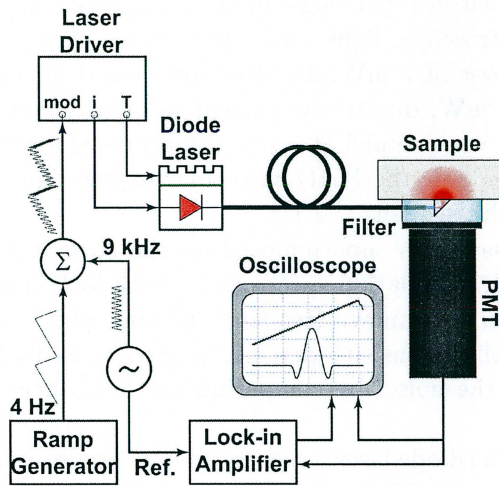
Figure 3.10: The set-up used during the GASMAS experiments. (Figure from [1]).
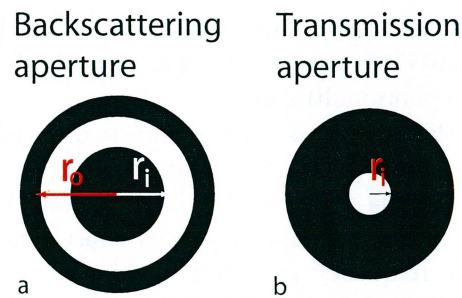

Figure 3.11: (a) Illustrative detection aperture for backscattering geometry, with inner radius r_i and outer radius r_o indicated. (b) Detection aperture for transmission geometry, with inner radius r_i indicated.

concentration and the distance of light traveling in air.

To calibrate the normalized WMS signal the standard addition method was used, as described in Chap. 2.5.5 [1].

Chapter 4

Results and discussion

Monte Carlo simulations implemented by the ray tracing program Advanced System Analysis Program (ASAP^{TM}) were done to model experimental results previously obtained in the group. The simulations were also used to optimize the detection geometry for future implementation of the technique. The influence of different scattering coefficients was studied as well. A comparison between the simulations and the diffusion equation was also performed. Finally, simulations were made to investigate the possibility of 3D-imaging of the sinus cavities using the GASMAS technique.

4.1 Choice of optical parameters

The models form a coarse approximation to the facial structures and the human sinus cavities. They are built up by two Delrin plates, called primary, S_1, and secondary, S_2, scatterers with thicknesses of l_1 and l_2, respectively. The plates are separated by a distance d; see Fig. 4.1.

Delrin is a highly scattering material, with almost no absorption, like human tissue. It was chosen to resemble human tissue and has a reduced scattering coefficient of about 2 mm^{-1}, as mentioned earlier. Optical properties of Delrin measured by the Linköping Biomedical Optics Group (LBOG) [39] at 632.8 nm, was found; see Table 4.1. Our measurements of the optical properties with the integrating sphere technique, (see Chap. 3.3), are also presented in this table, for a wavelength of 760 nm, as well as a time resolved measurement (see Chap. 3.4) at 780 nm. These three sets of optical properties, together with a fourth set found in Biomedical Photonics Handbook [49] for wavelengths of 674-849 nm, were used in simulations attempted to find the properties giving best resemblance to the experimental curves.

The anisotropy factor g was measured by LBOG to a value of 0.87. It was also measured with the integrating sphere to about the same value. Some techniques and sources mentioned, give a value of the scattering coefficient μ_s and some of the reduced scattering coefficient μ'_s. They are related to
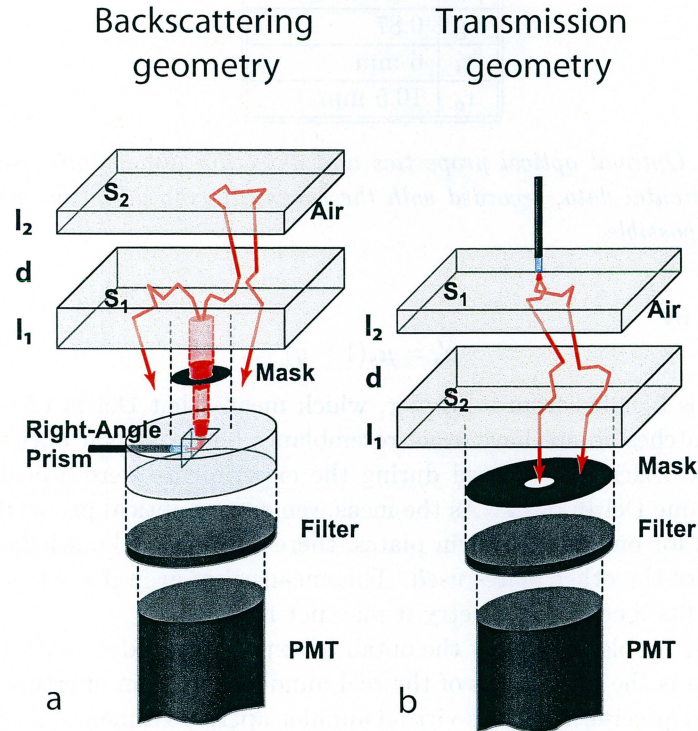
Figure 4.1: *The models used in the simulations. The primary, S_1, and secondary, S_2, of thickness l_1 and l_2, respectively, are separated by a distance d. (a) The backscattering geometry. (b) The transmission geometry.*

Optical properties	μ_s $[mm^{-1}]$	μ_s' $[mm^{-1}]$	μ_a $[mm^{-1}]$	g
LBOG [39]	18.0	2.4	0.0017	0.87
Integrating sphere	14	1.8	not measurable	0.87
Time resolved	8.5	1.1	0.0005	not measurable
Vo-Dinh [49]	7	0.9	not available	not available

Table 4.1: *Optical properties of Delrin.*

μ_s	14 mm^{-1}
μ_a	0.0005 mm^{-1}
g	0.87
r_i	6 mm
r_o	10.5 mm

Table 4.2: *Optimal optical properties and detection dimensions used to fit the experimental data, recorded with the backscattering detection geometry, as well as possible.*

each other by

$$\mu_s' = \mu_s(1 - g) \tag{4.1}$$

Delrin is blended from a powder, which means that Delrin pieces from different batches do not have exact resemblance between their optical properties. The Delrin plates used during the experiments were not all taken from the same Delrin block. As the measurements of optical properties only were made for one of the Delrin plates, there is no exact knowledge of the properties of the other plates used. This means that even if a set of optical properties fits a certain geometry it may not fit another.

Another problem to verify the obtained experimental data with the simulated data is the dimensions of the real annular detection aperture. These are not very precise, while the virtual annular aperture dimensions are. The dimensions influence the curve size and shape. Fine adjustments were done with the optical properties of the Delrin plate as well as the annular aperture dimensions to fit the experimental data as well as possible. Finally, it was shown that the set of optical properties and detection aperture dimensions seen in Table 4.2 and Fig. 4.2 gave the best resemblance.

It should also be noted that the accuracy of the optical properties is not that important, at least not in the framework of this work. However, in order to be able to quantitatively compare the results from simulations and experiments, the optical properties must be very well known. In the case of this master theses, it is rather a qualitatively comparison of the shape of the curves than the exact details that is of interest. This is due to the fact that when measuring on humans, the optical properties will vary a lot between different persons. The aim of the work is obtain a resemblance between simulated and experimental curves for optical properties in the range of possible properties for human tissue and use the simulation to evaluate the potential of the technique.

It is known that the reduced scattering coefficient for human tissue varies between 1 and 2 mm^{-1} from 600 to 800 nm [13]. The scattering coefficient varies linearly with the reduced scattering coefficient with a factor $1/(1 - g) \sim 10$ for $g = 0.9$. This means that μ_s has a value of 10 – 20 mm^{-1} for human tissue.

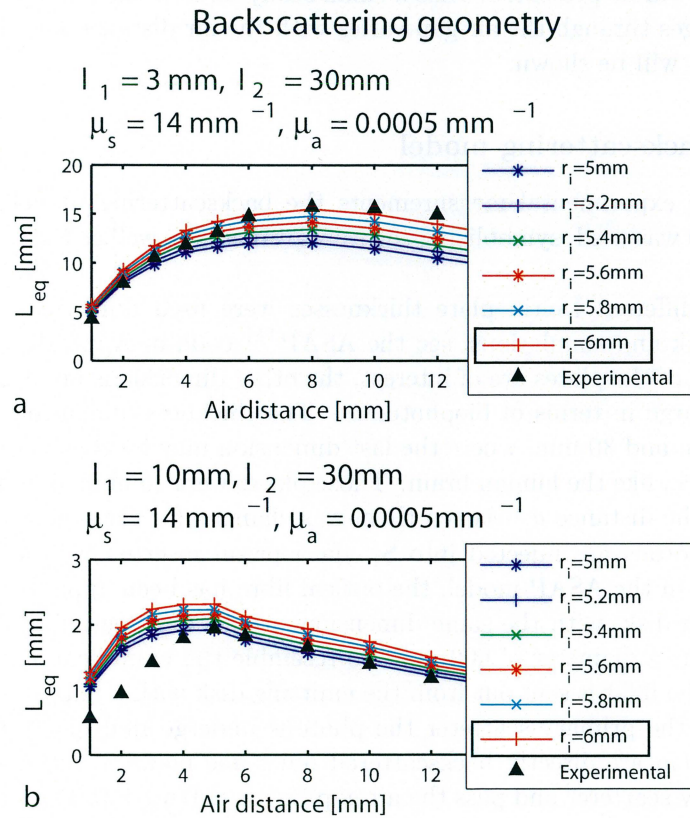Figure 4.2: *Simulated curves for the optimal optical properties, $\mu_s = 14$ mm^{-1}, $\mu_a = 0.0005$ mm^{-1} and $g = 0.87$. Illustrating how well the simulated data and the experimental data agree when the inner radius of the detection aperture, r_i, is varied and the outer radius is constant at 10.5 mm. The best resemblance with the experimental curves for both geometries were found for $r_i = 6$ mm.*

4.2   Comparing simulated and experimental data

Two different detection geometries, backscattering and transmission, have
been studied, and simulated data and experimental data have been com-
pared. Each geometry will be discussed more thoroughly in the following
chapters and finally a discussion on comparing the results from the two
geometries will be presented. Also a small study on how the number of mul-
tiple passages through the air gap varies with the air distance and different
geometries, will be shown.

4.2.1   Backscattering model

During the experimental measurements the backscattering model seen in
Fig. 4.1 (a) was used, symbolizing the frontal sinuses as well as the maxillary
sinuses.

Three different Delrin plate thicknesses were used during the experi-
mental work and simulations, see the ASAP$^{\text{TM}}$ code in Appendix C. The
thicknesses of the plates are of interest, the other dimensions are considered
infinitely large in terms of biophotonics. The thickness dimensions were 3
mm, 10 mm and 30 mm, where the last dimension may be considered as in-
finitely thick, like the human brain. Those plates were combined in different
ways and the distance d between them was changed for each measurement.

The photons are injected into S_1 via a prism inserted into a piece of
plexiglass. In the ASAP model, the optical fibre has been approximated to
an emitting disk, with the same dimensions as the intersection area of the
fibre, that is a diameter of 600 μm. To resemble the numerical aperture of
the fibre, the light is sent out from the emitting disk with a maximum angle
of 10°. In the primary scatterer the photons undergo multiple scattering.
Most of them are directly backscattered but some manage to get through
the primary scatterer and pass the air gap before getting into the secondary
scatterer. Here they are backscattered again and travel through the air once
more. Each time the photons travel through air, a fraction of them are
absorbed by the oxygen and there is an oxygen imprint in the light. Those
photons have traveled a distance of $2d$ or more. There is also a possibility for
reflection in the surfaces of S_1 and S_2, called multiple passes, which means
the absorptive imprint will be stronger, as the distance traveled through air
is longer. A path length in air of normal ambient composition of $2d = 20$
mm, gives rise to a fractional absorption of $4 \cdot 10^{-4}$ due to the strength of
the R7R7 oxygen line.

The absorption signal, which is weak due to the small air gaps (1 – 70
mm) and small absorption line intensity, is strongly diluted by the directly
backscattered photons, the so-called shortcut photons, with no gas absorp-
tive imprint. To reduce this problem a central beam stop is used. The larger
the inner detection radius is the deeper volumes of the scattering media will
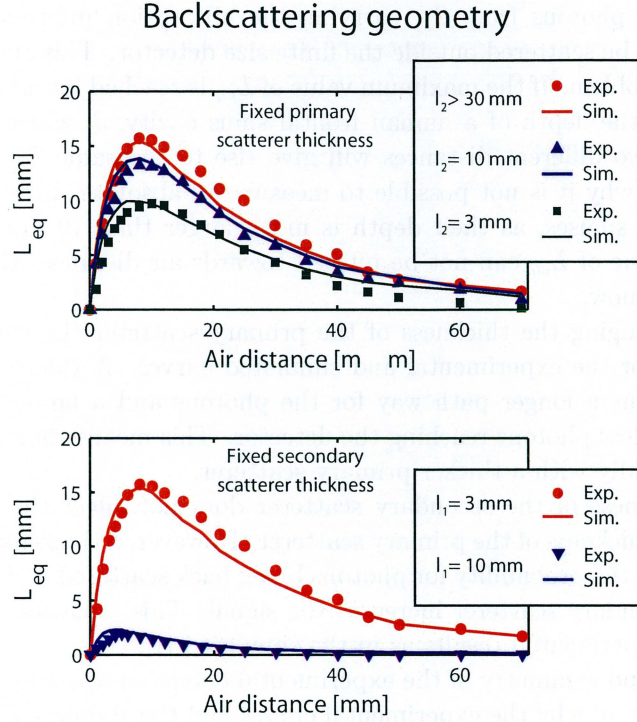
Figure 4.3: *Experimental and simulated results for $\mu_s = 14\ mm^{-1}$, $\mu_a = 0.0005\ mm^{-1}$ and $g = 0.87$ (a) and a fixed primary scatterer thickness, $l_1 = 3\ mm$. (b) and a fixed secondary scatterer thickness, $l_2 = 10\ mm$. The backscattering geometry has been used according to Fig. 4.1 (a).*

be probed and the stronger the relative influence of the absorption signal will be. On the other hand, there will be large losses of intensity to the detector by increasing the inner detection radius [1]. This will be discussed in detail in Chap. 4.3.

The backscattering geometry shows good agreement with the experimental result, see Fig. 4.3, even though all the simulated curves do not fit the experimental curves equally well. The major reason for this is that the three different plastic plates used during the experimental measurements did not all have the same optical properties, as explained in Chap. 4.1. It should also be stressed that the dimensions of the detection aperture have been adjusted to an inner radius of 6 mm compared to about 5 mm in the experiments.

The same dependence on the air distance between the scatterers is seen in the experimental curves as in the simulated. The equivalent mean path length in air, L_{eq} (the signal) increases with the air distance, as expected, until the light spot size grows too large. At air distances above a certain

threshold the photons from S_2, carrying the absorption information, are more likely to be scattered outside the finite size detector. This curve shape results in a problem. If the maximum value of L_{eq} is reached for air distances smaller than the depth of a human frontal sinus cavity, d, which is about 10 mm [1], two different distances will give rise to the same L_{eq}. This is the reason of why it is not possible to measure an absolute value of L_{eq} of the maxillary sinuses, as their depth is much larger than 10 mm and the maximum value of L_{eq} can not be pushed towards air distances that large, as far as we know.

When changing the thickness of the primary scatterer the dependence is the same for the experimental and simulated curves. A thicker primary scatterer means a longer path way for the photons and a larger spot size which means less photons reaching the detector. This means that the signal decreases rapidly with a thicker primary scatterer.

The thickness of the secondary scatterer does not effect the signal as much as the thickness of the primary scatterer. However, a thicker secondary scatterer rises the probability for photons being back scattered and therefore a thicker secondary scatterer increases the signal. This behavior is seen as well in the experimental results as in the simulated [1].

The size and symmetry of the experimental detection aperture might be another reason of why the experimental curves and the simulated curves do not agree totally. The precision of the detection aperture cutting was low, why neither the size nor the symmetry of it is well defined, the air distances are not more accurate than 0.1 mm either. As discussed before, the optical properties can be another reason why there is no total resemblance, since the Delrin plates cannot be exactly represented by one set of optical properties. A final source of error is, as mentioned in Chap. 3.1, that when using Monte Carlo simulations in ASAP$^{\text{TM}}$ there are no Fresnel reflections simulated.

How the number of multiple passes varies with the air distance and with the thickness of the scatterers has been investigated. This can easily be done from the simulations but is impossible to achieve experimentally. In Tables 4.3 – 4.6 the results are presented for the different plate thicknesses. The percents between different number of passes and the total rays reaching the detector are shown.

All rays reaching the detector that have traveled over the air distance, in the case of backscattering geometry, must have passed the air distance at least twice (back and forth). In the tables it can be seen that with increasing air distance the fraction of multiple passes decrease. This can be explained by the finite size of the detector, see Fig. 4.4 where only the case of two passes is shown.

Since a larger air distance corresponds to that rays travel longer over the air gap and therefore enter the second scatterer further out on the secondary scatterer and the same when they travel back to the primary scatterer, the chance to get detected decrease. The same concept also explains the increase

Air distance [mm]	1	5	10	30	70
2 passes [%]	55	71	77	85	97
4 passes [%]	26	20	16	12	3
6 passes [%]	11	6	5	2	0
8 passes [%]	5	2	2	0	0
10 passes [%]	2	1	1	0	0
12 passes [%]	1	0	0	0	0
14 passes [%]	0	0	0	0	0
$\sum$ [%]	≈ 100	≈ 100	≈ 100	≈ 100	≈ 100

Table 4.3: *The table shows in percent, how the number of multiple passes varies with the air distance, in relation to all rays reaching the detector, for $l_1 = 3$ mm and $l_2 = 3$ mm and $r_i = 3$ mm and $r_o = 10.5$ mm in backscattering geometry.*

Air distance [mm]	1	5	10	30	70
2 passes [%]	47	63	70	82	94
4 passes [%]	25	21	19	14	6
6 passes [%]	13	9	7	3	0
8 passes [%]	7	4	2	1	0
10 passes [%]	4	2	1	0	0
12 passes [%]	2	1	0	0	0
14 passes [%]	1	0	0	0	0
$\sum$ [%]	≈ 100	≈ 100	≈ 100	≈ 100	≈ 100

Table 4.4: *The table shows in percent, how the number of multiple passes varies with the air distance, in relation to all rays reaching the detector, for $l_1 = 3$ mm and $l_2 = 10$ mm and $r_i = 3$ mm and $r_o = 10.5$ mm in backscattering geometry.*
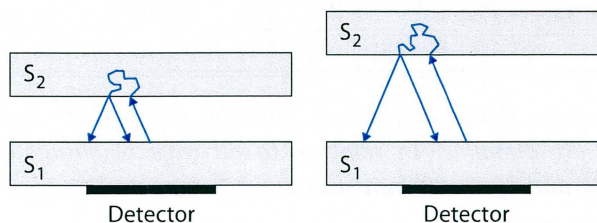

Figure 4.4: *Illustrative figures of how the air distance influences the number of multiple passes.*

Air distance [mm]	1	5	10	30	70
2 passes [%]	44	59	66	81	93
4 passes [%]	25	22	19	15	6
6 passes [%]	13	9	8	4	1
8 passes [%]	7	4	3	1	0
10 passes [%]	4	2	2	0	0
12 passes [%]	2	1	1	0	0
14 passes [%]	1	1	0	0	0
$\sum$ [%]	≈ 96	≈ 98	≈ 100	≈ 100	≈ 100

Table 4.5: *The table shows in percent, how the number of multiple passes varies with the air distance, in relation to all rays reaching the detector, for $l_1 = 3$ mm and $l_2 = 30$ mm and $r_i = 3$ mm and $r_o = 10.5$ mm in backscattering geometry.*

Air distance [mm]	1	5	10	30	70
2 passes [%]	31	42	51	74	98
4 passes [%]	20	22	23	19	2
6 passes [%]	14	13	11	5	0
8 passes [%]	10	8	6	1	0
10 passes [%]	7	4	3	1	0
12 passes [%]	5	4	2	0	0
14 passes [%]	3	2	2	0	0
$\sum$ [%]	≈ 90	≈ 95	≈ 100	≈ 100	≈ 100

Table 4.6: *The table shows in percent, how the number of multiple passes varies with the air distance, in relation to all rays reaching the detector, for $l_1 = 10$ mm and $l_2 = 30$ mm and $r_i = 3$ mm and $r_o = 10.5$ mm in backscattering geometry.*

of multiple passes with thicker primary scatterer, i.e. a thicker primary scatterer can collect oblique rays that have been through more multiple passes. It is also observed that a thicker secondary scatterer increases the number of multiple passes, as a thicker secondary scatterer allows more photons to be scattered back to the primary scatterer. It should be stressed again that the Monte Carlo model used in ASAP^{TM} does not simulate Fresnel reflections, just diffuse reflections.

The simulation time depends on many factors. Naturally the simulation time increases with the number of injected rays. Using a larger reduced scattering coefficient means longer simulation time, as do thicker scatterers. As the simulations of this thesis involves both different reduced scattering coefficients and scatterer thicknesses, the simulation time varies. To prevent simulation times longer than 6-7 hours per point, some simulations had 500 000 rays injected, and most of them had 1 000 000 rays injected. Also the air distance between the plates effects the simulation time, the smaller air distances takes longer time to simulate than the larger air distances. The simulation times varied between 1-2 hours per point to 6-7 hours per point, which means 1-6 days to get a curve with 20 points.

4.2.2 Transmission model

Also a transmission model, symbolizing the maxillary sinuses, seen in Fig. 4.1 was investigated and simulated data were compared with experimental data; see the ASAP^{TM} code in Appendix D.

The plates used and simulated were 6 and 10 mm thick, respectively. The model was built up by one primary, S_1 and one secondary scatterer S_2, like the backscattering model denoted as in Fig. 4.1. The major difference between the transmission and the backscattering geometry is the fact that all photons reaching the detector must have passed the air gap, which should result in a larger resulting L_{eq}.

In this geometry there is a quite good resemblance between experimental and simulated data as well, see Fig. 4.5. In both the experimental and simulated curves it is seen that the thickness of the primary and the secondary scatterers do not have the same impact on the oxygen signal as in the case of backscattering detection geometry. The oxygen signal increases with the air distance in all cases, as all detected photons have passed through the air. In Fig. 4.5 it is seen that a thicker secondary scatterer gives a slightly larger equivalent mean path length, as a thicker secondary scatterer gives oblique photons, with longer air path way, a larger probability to be scattered into the detection area. This behavior is also seen in the simulated curves, even if both the simulated curves lies somewhat above the experimental.

The effect of changing the primary scatterer is very small. In the experimental curves a small divergence is seen for small air distances. This effect comes from the fact that a somewhat larger fraction of the photons have
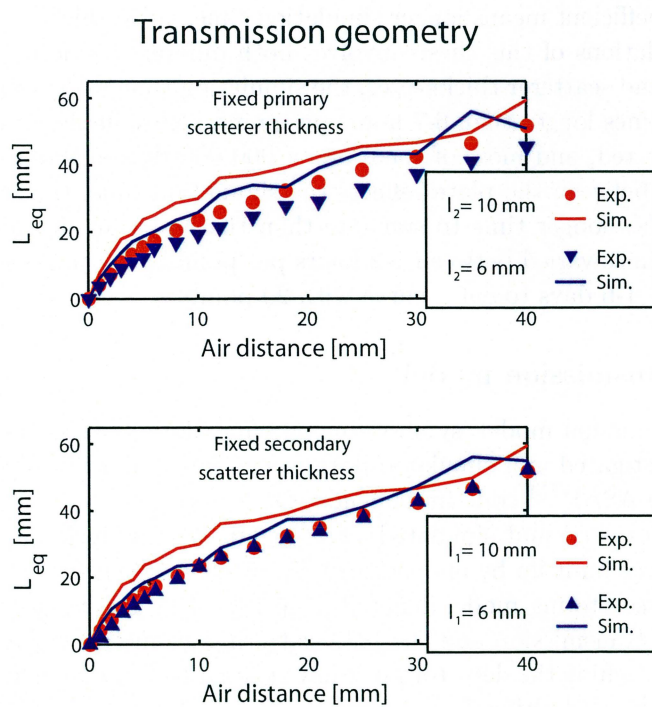
Figure 4.5: *Experimental and simulated results for $\mu_s = 14$ mm^{-1}, $\mu_a = 0.0005$ mm^{-1} and $g = 0.87$ (a) and a fixed primary scatterer thickness, $l_1 = 10$ mm. (b) and a fixed secondary scatterer thickness, $l_2 = 10$ mm. The transmission geometry has been used according to Fig. 4.1 (b).*
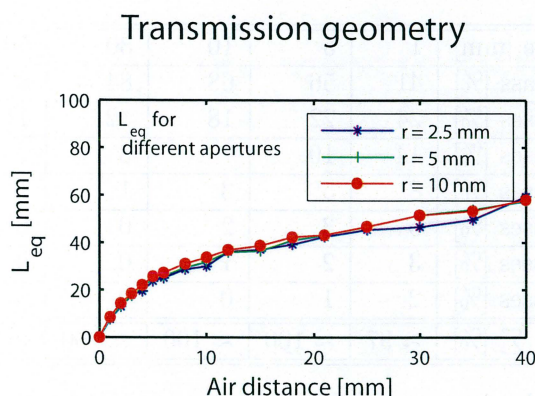
Figure 4.6: *The influence of different aperture radii in the case of transmission geometry, for $\mu'_s = 1.8$ mm^{-1}, $\mu_a = 0.0005$ mm^{-1}, $l_1 = 10$ mm and $l_2 = 10$ mm*

gone a slightly longer path through the air, as a thicker primary scatterer presents a larger solid angle to the air gap. As this is a very small effect is it not seen for larger distances [1]. This behavior cannot be seen in the simulations, as it is very small and the quite poor photon statistics makes the simulated curves uneven. Even though the small effects cannot be seen, the gross curve structure still have a good resemblance.

The major reason for the simulated transmission curves to resemble less, compared to the backscattering geometry, with the experiment is the fact that the plates of the experiment do not have exactly the same optical properties as the simulated, see Chap. 4.1. It could be noted that the the size of the detection aperture will not influence the resulting signal in a larger scale, as seen in Fig. 4.6.

Another reason is bad photon statistics, especially for larger air distances, as fewer photons reach the finite size detector. Another reason why the transmission simulations resembles somewhat less than the backscattering might be that some of the plates used during the transmission measurement have uneven thicknesses together with the size of the air distance, which in the experiments cannot be measured more accurately than to 0.1 mm, in the simulations the sizes of the air gap is exact. A final source of error is again the fact that the Monte Carlo model used in ASAP$^{\text{TM}}$ does not simulate Fresnel reflections.

As in the case of backscattering geometry, a study of how the number of multiple passes varies with the air distance and with the thickness of the scatterers has been studied in the case of transmission geometry. The results are shown in Tables 4.7 – 4.9.

In this case, all rays reaching the detector must have traveled at least once over the air distance. The same behavior as for the backscattering case

Air distance [mm]	1	5	10	30	70
1 pass [%]	41	56	68	84	87
3 passes [%]	24	22	18	12	11
5 passes [%]	14	10	7	3	2
7 passes [%]	8	5	3	1	1
9 passes [%]	5	3	2	0	0
11 passes [%]	3	2	1	0	0
13 passes [%]	2	1	0	0	0
$\sum$ [%]	≈ 97	≈ 100	≈ 100	≈ 100	≈ 100

Table 4.7: *The table shows in percent, how the number of multiple passes varies with the air distance, in relation to all rays reaching the detector, for $l_1 = 6$ mm and $l_2 = 10$ mm and $r_i = 2.5$ mm in transmission geometry.*

Air distance [mm]	1	5	10	30	70
1 pass [%]	41	56	66	84	88
3 passes [%]	23	22	19	12	10
5 passes [%]	14	10	8	3	2
7 passes [%]	8	5	3	1	0
9 passes [%]	5	3	2	0	0
11 passes [%]	3	2	1	0	0
13 passes [%]	2	1	0	0	0
$\sum$ [%]	≈ 96	≈ 100	≈ 100	≈ 100	≈ 100

Table 4.8: *The table shows in percent, how the number of multiple passes varies with the air distance, in relation to all rays reaching the detector, for $l_1 = 10$ mm and $l_2 = 6$ mm and $r_i = 2.5$ mm in transmission geometry.*

Air distance [mm]	1	5	10	30	70
1 passes [%]	35	49	61	81	88
3 passes [%]	22	23	20	14	10
5 passes [%]	14	11	9	4	2
7 passes [%]	9	6	4	1	1
9 passes [%]	6	4	2	0	0
11 passes [%]	4	3	2	0	0
13 passes [%]	3	1	1	0	0
$\sum$ [%]	≈ 93	≈ 97	≈ 100	≈ 100	≈ 100

Table 4.9: *The table shows in percent, how the number of multiple passes varies with the air distance, in relation to all rays reaching the detector, for $l_1 = 10$ mm and $l_2 = 10$ mm and $r_i = 2.5$ mm in transmission geometry.*

is observed, i.e. an increase of the air distance results in less rays detected with multiple passes. This could again be understood by the finite size of the detector. An increase of the air distance will result in rays entering the secondary scatterer further out and the possibility for these rays to be detected decreases. This also explains why a thicker secondary scatterer results in more detected multiple passes rays, since more oblique rays will be collected.

The simulation time of a transmission geometry depends on the same factors as the backscattering geometry. At larger air distances the photon statistics are poor as very few (fewer than in the backscattering geometry) photons reaches the detector, about 0.1% of the injected flux is detected in the transmission geometry. This means that more injected rays are wanted, which also increases the simulation time. The transmission geometries are simulated with 2 000 000 rays injected. Such a simulation takes 6-8 days per curve.

4.3 Detection aperture optimization

The annular detection aperture in the backscattering model, can be seen as a ring with an inner radius, r_i and an outer radius, r_o; see Fig. 3.11 in Chap. 3.5. Its task is to stop directly backscattered photons, shortcut photons, which only have interacted with S_1. A larger inner radius of the detection aperture will sample photons from deeper volumes. At the same time the detected flux will decrease with a large inner radius. A larger outer radius will rise the value of the equivalent mean path length as well, as more of the deep going photons will be sampled. The flux is getting lower at larger radii, thus the size of the outer radius will have a smaller impact than the size of the inner. It may also have the effect of moving the maximum L_{eq} towards larger values of d. This behavior is appreciated as the maximum value of L_{eq} should be located at an air distance d of about 10 mm, which is the depth of a human frontal sinus cavity [1]. All these behaviors were investigated in simulations. The detection geometry of the transmission model do not affect the curve shape or size, as seen in Fig. 4.6.

To be able to give an indication of which dimension on the detection aperture that is the optimal, an optimization number Q_{st} must be found. To find an equation for Q_{st}, it is important to know what parameters that are of interest. In this case there are three factors of impact; the flux, the equivalent mean path length (L_{eq}) and the air gap d, corresponding to the maximum L_{eq}.

$$Q_{st} = \langle L_{eq} \rangle_{max} \cdot \phi_{det} \cdot d \qquad d \geq 10mm \qquad (4.2)$$

In Fig. 4.7 (a) it is seen how the flux increases with the outer radius of detection, while keeping the inner radius fixed at 3 mm. Fig 4.8 (a) shows
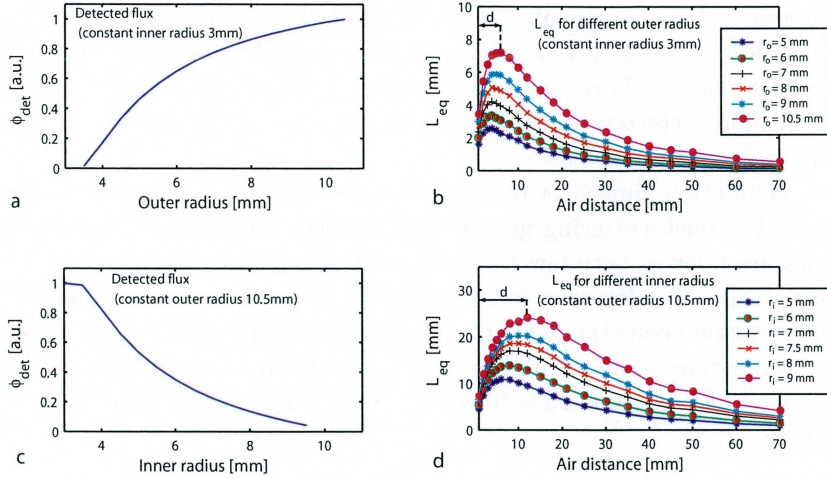
Backscattering geometry

Figure 4.7: *Studies of the influence of the annular detection aperture in backscattering geometry. The simulations have been performed for a model with a primary scatterer thickness of 3 mm and a secondary scatterer thickness of 10 mm, $\mu_s' = 1.8$ mm^{-1} and $\mu_a = 0.0005$ mm^{-1}. (a) The flux as a function of outer radius, r_o, the inner radius is kept constant at 3 mm. (b) L_{eq} for the same conditions as in (a). (c) The flux as a function of inner radius, r_i, the outer radius is kept constant at 10.5 mm. (d) L_{eq} for the same conditions as in (c).*

how the detected flux varies between 0 to 15 percent of the injected flux. The equivalent mean path length increases as well, together with the location of the maximum L_{eq}, as seen in Fig. 4.7 (b). The maximum outer radius is 10.5 mm, as that is the radius of the detector. The minimum inner radius is 3 mm, due to the radius of the injection system of approximately 3 mm.

When keeping the outer radius fixed at 10.5 mm and increasing the inner detection radius, the flux decreases as seen in Fig. 4.7 (c). Fig. 4.8 (b) shows how the detected flux varies between 15 and almost 0 percent of the injected flux. The equivalent mean path length on the other hand increases with the inner radius, together with d; as seen in Fig. 4.7 (d).

The optimal dimensions of the detection aperture can be found according to Eq. 4.2. The result for the four different geometries are seen in Figs 4.9 – 4.12, where the Q_{st} factor for the different cases also is plotted. In the Q_{st} factor plots it is also indicated where the condition that $d \geq 10$ mm is valid by shadow over the radii where it is not valid.

In the case of a dynamic measurement, when the change in oxygen signal is studied, the condition $d \geq 10$ mm is not needed since it does not matter
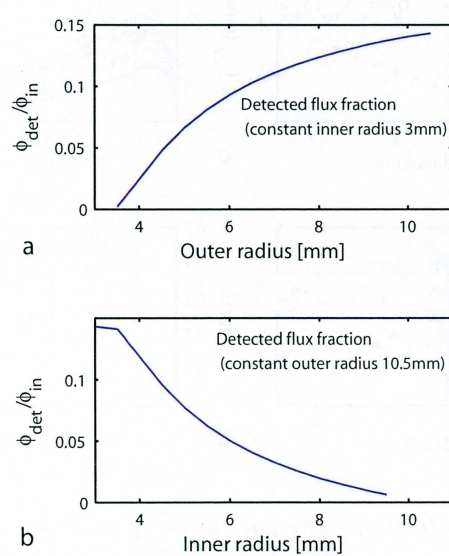
Figure 4.8: *Detected fraction of injected flux when in (a) the inner radius has been kept constant at 3 mm while the outer radius has been varied. (b) The outer radius has been kept constant at 10.5 mm while the inner radius has been varied. The simulations have been performed for a model with a primary scatterer thickness of 3 mm and a secondary scatterer thickness of 10 mm, $\mu_s' = 1.8$ mm^{-1} and $\mu_a = 0.0005$ mm^{-1}.*
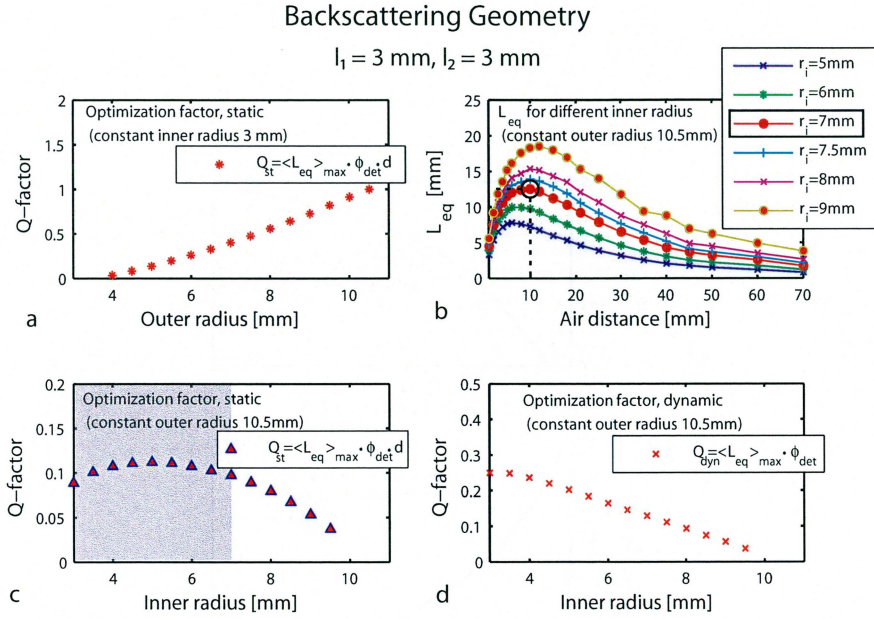
Figure 4.9: *Optimal detection dimensions for $l_1 = 3$ mm and $l_2 = 3$ mm, $\mu'_s = 1.8$ mm^{-1} and $\mu_a = 0.0005$ mm^{-1}, in backscattering geometry. (a) The optimal outer radius is found to be 10.5 mm, when the inner radius is kept constant at 3 mm and the outer radius is varied. (b) The air distance d, corresponding to $< L_{eq} >_{max}$, reaches a value of 10 mm for an inner detection radius of 7 mm, when the outer radius is kept constant at 10.5 mm and the inner radius is varied. (c) The optimal inner detection radius is found to be 7 mm, when the outer radius is kept constant at 10.5 mm and the inner radius is varied, in the static case. The not shaded area shows where the condition $d \geq 10$ mm is fulfilled. (d) In the dynamic case, the optimal inner radius is found to be 3.5 mm, when the outer radius is kept constant at 10.5 mm and the inner radius is varied.*
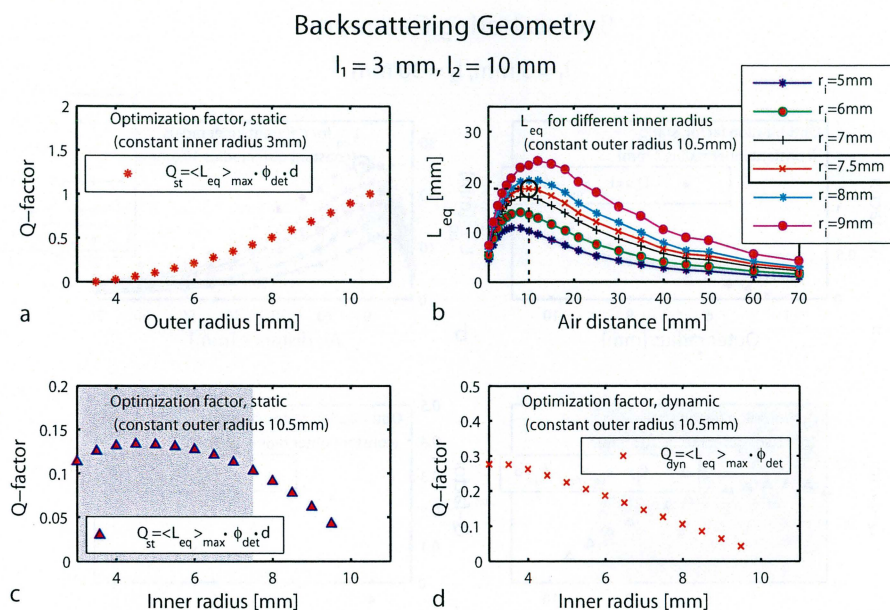
Figure 4.10: *Optimal detection dimensions for $l_1 = 3$ mm and $l_2 = 10$ mm, $\mu'_s = 1.8$ mm^{-1} and $\mu_a = 0.0005$ mm^{-1}, in backscattering geometry. (a) The optimal outer radius is found to be 10.5 mm, when the inner radius is kept constant at 3 mm and the outer radius is varied. (b) The air distance d, corresponding to $< L_{eq} >_{max}$, reaches a value of 10 mm for an inner detection radius of 7.5 mm, when the outer radius is kept constant at 10.5 mm and the inner radius is varied. (c) The optimal inner detection radius is found to be 7.5 mm, when the outer radius is kept constant at 10.5 mm and the inner radius is varied, in the static case. The not shaded area shows where the condition $d \geq 10$ mm is fulfilled. (d) In the dynamic case, the optimal inner radius is found to be 3.5 mm, when the outer radius is kept constant at 10.5 mm and the inner radius is varied.*
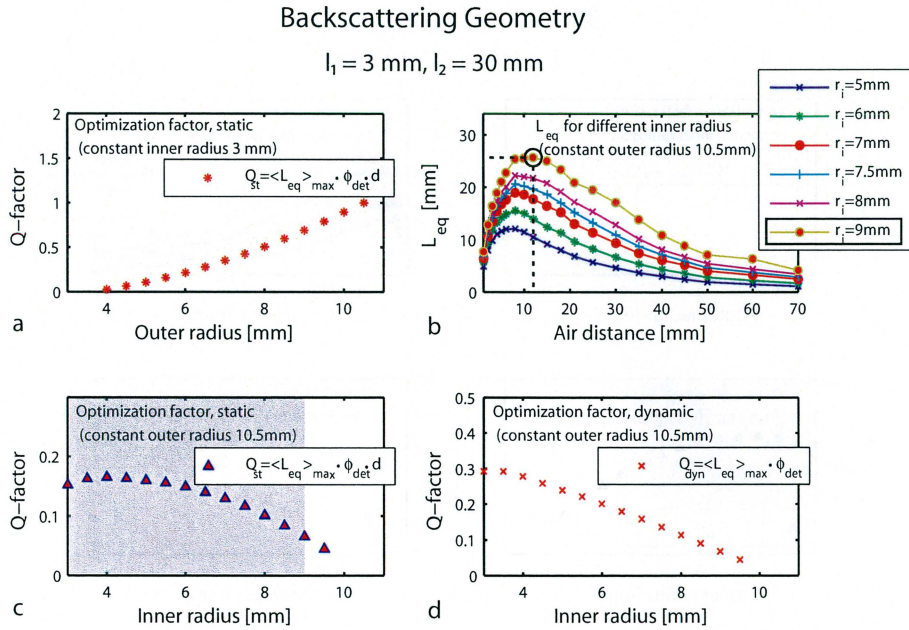
Figure 4.11: *Optimal detection dimensions for $l_1 = 3$ mm and $l_2 = 30$ mm, $\mu'_s = 1.8$ mm^{-1} and $\mu_a = 0.0005$ mm^{-1}, in backscattering geometry. (a) The optimal outer radius is found to be 10.5 mm, when the inner radius is kept constant at 3 mm and the outer radius is varied. (b) The air distance d, corresponding to $< L_{eq} >_{max}$, reaches a value of 10 mm or more for an inner detection radius of 9 mm, when the outer radius is kept constant at 10.5 mm and the inner radius is varied. (c) The optimal inner detection radius is found to be 9 mm, when the outer radius is kept constant at 10.5 mm and the inner radius is varied, in the static case. The not shaded area shows where the condition $d \geq 10$ mm is fulfilled. (d) In the dynamic case, the optimal inner radius is found to be 3.5 mm, when the outer radius is kept constant at 10.5 mm and the inner radius is varied.*
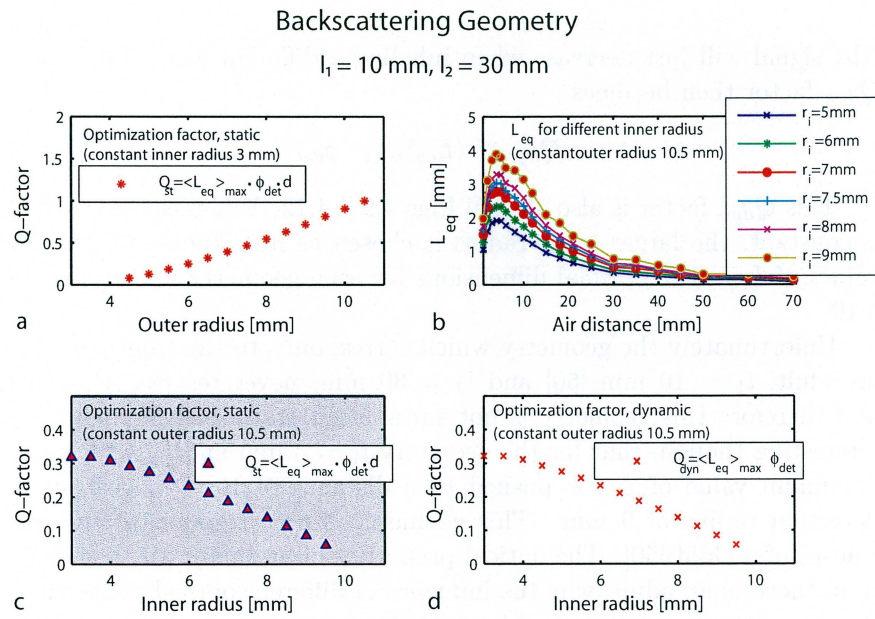
Figure 4.12: *Optimal detection dimensions for $l_1 = 10$ mm and $l_2 = 30$ mm, $\mu'_s = 1.8$ mm^{-1} and $\mu_a = 0.0005$ mm^{-1}, in backscattering geometry. (a) The optimal outer radius is found to be 10.5 mm, when the inner radius is kept constant at 3 mm and the outer radius is varied. (b) The air distance d, corresponding to $< L_{eq} >_{max}$, never reaches a value of 10 mm or more, when the outer radius is kept constant at 10.5 mm and the inner radius is varied. (c) There is no optimal inner radius for the static case, when the outer radius is kept constant at 10.5 mm and the inner radius is varied. The not shaded area shows where the condition $d \geq 10$ mm is fulfilled. (d) In the dynamic case, the optimal inner radius is found to be 3.5 mm.*

Geometry	r_o [mm]	r_i [mm], static	r_i [mm], dynamic
$l_1 = 3$ mm, $l_2 = 3$ mm	10.5	7	3.5
$l_1 = 3$ mm, $l_2 = 10$ mm	10.5	7.5	3.5
$l_1 = 3$ mm, $l_2 = 30$ mm	10.5	9	3.5
$l_1 = 10$ mm, $l_2 = 30$ mm	10.5	–	3.5

Table 4.10: *Optimal detection dimensions according to Eq. 4.2 and Eq. 4.3.*

(the signal will just decrease when inhaling a different gas). The resulting Q_{dyn} factor then becomes

$$Q_{dyn} = \langle L_{eq} \rangle_{max} \cdot \phi_{det} \qquad (4.3)$$

This Q_{dyn} factor is also seen in Figs 4.9 – 4.12. When the value of Q_{dyn} is constant, the larger inner radius is chosen as it is known to give larger values of L_{eq}. The optimal dimensions for each geometry are seen in Table 4.10.

Unfortunately the geometry which corresponds to the frontal sinuses of an adult, $l_1 = 10$ mm [50] and $l_2 = 30$ mm, never reaches $d = 10$ mm and therefore this geometry is not suitable for static measurements. It is interesting though, that for the geometry $l_1 = 3$ mm and $l_2 = 30$ mm, the maximum value of L_{eq} is pushed to a distance of 10 mm with an inner detection radius of 9 mm. This geometry can correspond to the frontal sinuses of a child [50]. The optical properties of an infant are also different from those of an adult, why the influence of different optical properties and primary scatterers are studied in the following section.

It should be noted that in the case of dynamic measurements, when using the backscattering geometry, it is also possible to investigate the maxillary sinuses. Due to their approximate depth of 30 mm it is always impossible to study absolute values, i.e. perform static measurements.

4.4 Varying the reduced scattering coefficient

Simulations were done to study the influence of the reduced scattering coefficient. The scattering coefficient has a relatively high inter individual variation and varies especially with age [13, 49, 51]. The skull of a neonate does not have as high reduced scattering coefficient as an adult skull. Infants also have thinner skull bones, about 3 mm thick for children being born after just 7 - 8 months in the mothers womb. The thickness of the skull bone also varies from person to person, but for an adult it is about 10 mm thick. Even though we have used optical properties and dimensions of neonates it should be noted that neonates do not have frontal sinuses, they start to grow up at an age of about 6 – 7 years. Even at this age the reduced scattering coefficient of the skull is lower than that for an adult, the optical

Optical properties	μ_s [mm^{-1}]	g	μ_s' [mm^{-1}]	μ_a [mm^{-1}]
Adult skull in vitro	16	0.87	2.0 [49] (800 nm)	NA
Delrin	14	0.87 [39]	1.8	0.0005
Adult skull in vivo	13	0.93 [52] (650 - 950 nm)	0.9 [49] (674 - 849 nm)	NA
Neonate skull in vivo	9.3	0.93 [52] (650 - 950 nm)	0.65 [51] (761 nm)	NA

Table 4.11: *Optical properties used in simulations, valid wavelength regions are seen in brackets.*

properties for neonatal skull was used as they were at hand. Neonates do have maxillary sinuses though.

Simulations were made of the backscattering geometry, with primary thicknesses of 3, 5 and 10 mm. The optical properties used are shown in Table 4.11.

The values of the reduced scattering coefficient, μ_s', for adult scalp and skull in vitro and adult skull in vivo are found in Biomedical Photonics Handbook [49]. The value of μ_s' for neonate skull in vivo was found in S. Ijichi *et al.* [51]. The anisotropy factors for Delrin are measured by the Linköping Biomedical Optics Group [39]. The same is used for adult skull in vitro. For adult and neonate skull in vivo, an anisotropy factor for porcine skull, found in N. Ugryumova et al. [52], was used. It should be stressed that it is the reduced scattering coefficient, $\mu_s' = \mu_s(1 - g)$, that is of importance for the results. This means that as long as the reduced scattering coefficient is known, the values of the scattering coefficient and the anisotropy factor are arbitrary under the condition that they must give the correct value of μ_s'. It is of importance to know g and μ_s since these are needed in ASAP$^{\text{TM}}$ as they are used in the calculations of the Monte Carlo simulation; see Chap. 2.2.4. As no values of μ_a was found, it was approximated to zero as the wavelength of the simulated light is in the range of the optical window seen in Fig. 2.1. The results from the simulations of scatterers with different optical properties are shown in Fig. 4.13.

The same investigation of optimal detection dimensions were conducted for the different scattering coefficients and thicknesses of S_1; as in Chap. 4.3. The Q_{st}- and Q_{dyn}-factors are plotted together with the signals for different scattering coefficients and thicknesses of S_1 in Figs 4.14 – 4.18.

The main results are collected in Table 4.12.

It is seen that it is possible to get a signal, which fulfills the condition $d \geq 10$ for frontal sinuses, for plates corresponding to neonatal skull with primary scatterer thicknesses of 3 mm and 5 mm, in the case of static
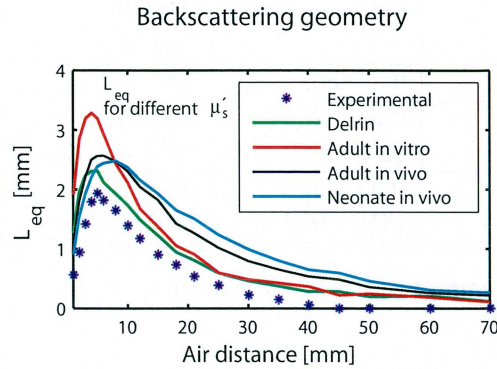
Backscattering geometry

Figure 4.13: The influence of different values of μ'_s is studied in backscattering geometry, with the optical properties shown in Table 4.11. It is seen that both the maximum value of L_{eq} and the corresponding air distance d, varies with μ'_s. The fact that the curve for neonatal skull in vivo has its maximum for a larger d than the others makes it of special interest. The scatterer thicknesses used were l_1 =10 mm and l_2 =30 mm, the detection aperture dimensions were r_i =6 mm and r_o =10.5 mm.

Geometry	r_o [mm]	r_i [mm], static	r_i [mm], dynamic
child skull in vivo $l_1 = 3$ mm	10.5	8	3.5
child skull in vivo $l_1 = 5$ mm	10.5	6	3.5
child skull in vivo $l_1 = 10$ mm	10.5	–	3.5
adult skull in vivo $l_1 = 10$ mm	10.5	–	3.5
adult skull in vitro $l_1 = 10$ mm	10.5	–	3.5

Table 4.12: *Optimal detection dimensions in backscattering geometry for different reduced scattering coefficients and thicknesses of the skull bone or cheek bone (primary scatterer) in the case of dynamic measurements.*
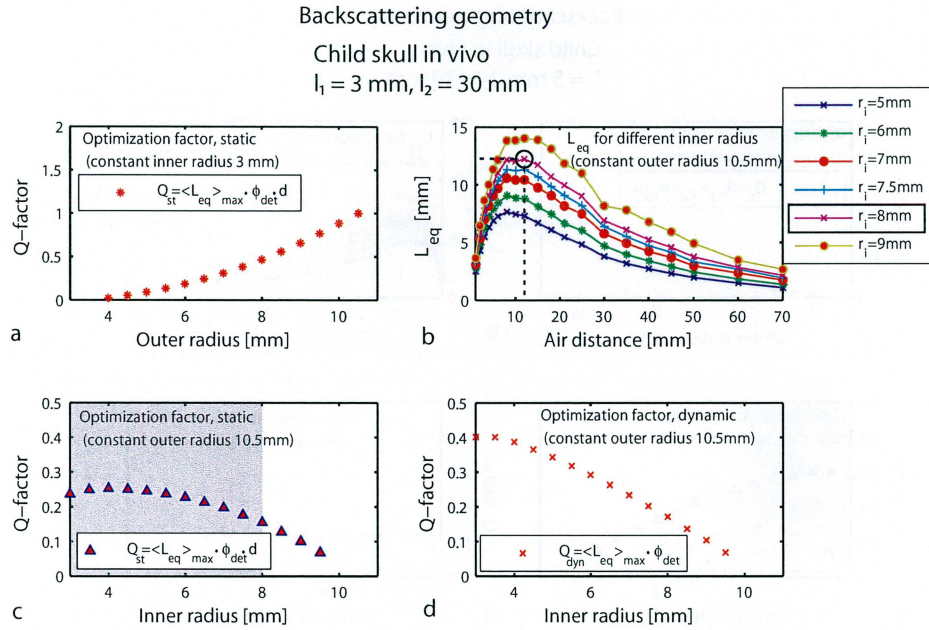
Figure 4.14: *Optimal detection dimensions for child skull in vivo $l_1 = 3$ mm and $l_2 = 30$ mm, $\mu'_s = 0.65$ mm^{-1} and $\mu_a = 0$ mm^{-1}, in backscattering geometry. (a) The optimal outer radius is found to be 10.5 mm, when the inner radius is kept constant at 3 mm and the outer radius is varied. (b) The air distance d, corresponding to $< L_{eq} >_{max}$, reaches a value 10 mm or more for an inner detection radius of 8 mm, when the outer radius is kept constant at 10.5 mm and the inner radius is varied. (c) The optimal inner radius for the static case is found to be 8 mm, when the outer radius is kept constant at 10.5 mm and the inner radius is varied. The not shaded area shows where the condition $d \geq 10$ mm is fulfilled. (d) In the dynamic case, the optimal inner radius is found to be 3.5 mm, when the outer radius is kept constant at 10.5 mm and the inner radius is varied.*
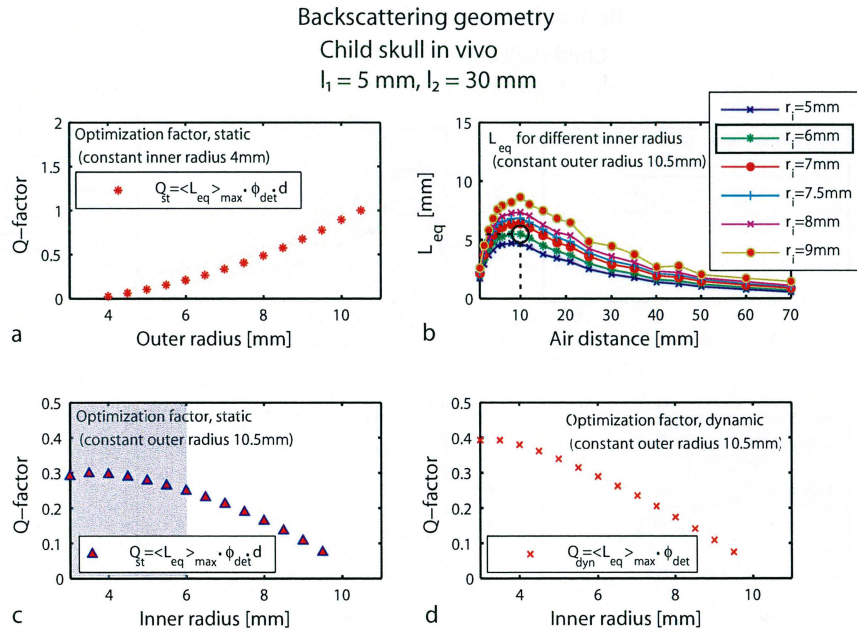
Figure 4.15: *Optimal detection dimensions for child skull in vivo $l_1 = 5$ mm and $l_2 = 30$ mm, $\mu'_s = 0.65$ mm^{-1} and $\mu_a = 0$ mm^{-1} in backscattering geometry. (a) The optimal outer radius is found to be 10.5 mm, when the inner radius is kept constant at 3 mm and the outer radius is varied. (b) The air distance d, corresponding to $< L_{eq} >_{max}$, reaches a value 10 mm or more for an inner detection radius of 6 mm, when the outer radius is kept constant at 10.5 mm and the inner radius is varied. (c) The optimal inner radius for the static case is found to be 6 mm, when the outer radius is kept constant at 10.5 mm and the inner radius is varied. The not shaded area shows where the condition $d \geq 10$ mm is fulfilled. (d) In the dynamic case, the optimal inner radius is found to be 3.5 mm, when the outer radius is kept constant at 10.5 mm and the inner radius is varied.*
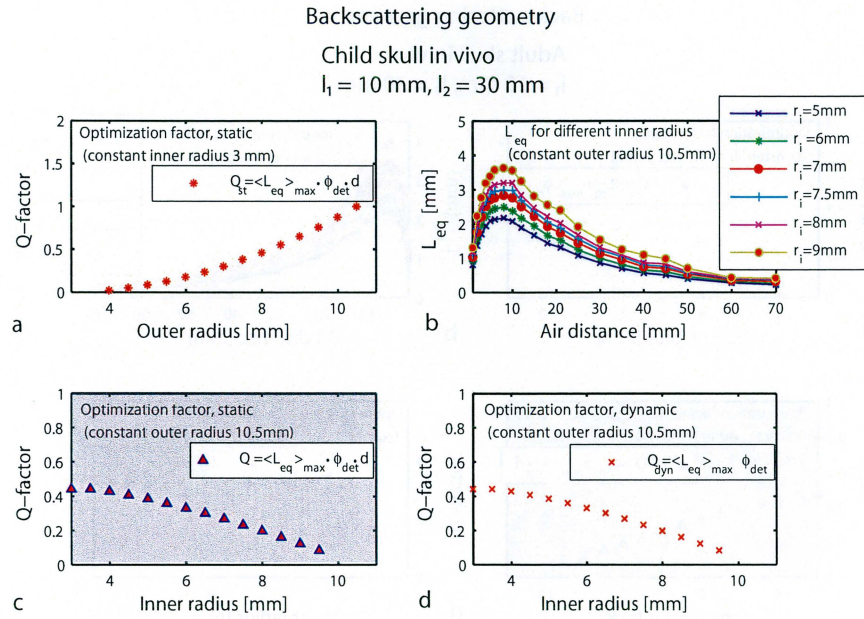
Figure 4.16: *Optimal detection dimensions for child skull in vivo $l_1 = 10$ mm and $l_2 = 30$ mm, $\mu'_s = 0.65$ mm^{-1} and $\mu_a = 0$ mm^{-1}, in backscattering geometry. (a) The optimal outer radius is found to be 10.5 mm, when the inner radius is kept constant at 3 mm and the outer radius is varied. (b) The air distance d, corresponding to $< L_{eq} >_{max}$, never reaches a value 10 mm or more, when the outer radius is kept constant at 10.5 mm and the inner radius is varied. (c) The optimal inner radius for the static case is not found, when the outer radius is kept constant at 10.5 mm and the inner radius is varied. The not shaded area shows where the condition $d \geq 10$ mm is fulfilled.(d) In the dynamic case, the optimal inner radius is found to be 3.5 mm, when the outer radius is kept constant at 10.5 mm and the inner radius is varied.*
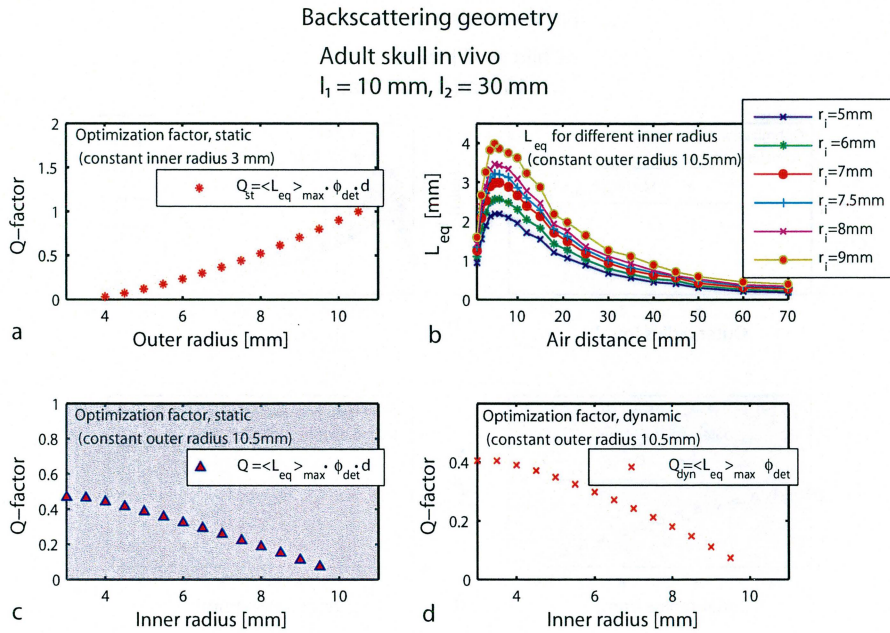
Figure 4.17: *Optimal detection dimensions for adult skull in vivo $l_1 = 10$ mm and $l_2 = 30$ mm, $\mu_s' = 0.9$ mm^{-1} and $\mu_a = 0$ mm^{-1} in backscattering geometry. (a) The optimal outer radius is found to be 10.5 mm, when the inner radius is kept constant at 3 mm and the outer radius is varied. (b) The air distance d, corresponding to $< L_{eq} >_{max}$, never reaches a value 10 mm or more, when the outer radius is kept constant at 10.5 mm and the inner radius is varied. (c) The optimal inner radius for the static case is not found, when the outer radius is kept constant at 10.5 mm and the inner radius is varied. The not shaded area shows where the condition $d \geq 10$ mm is fulfilled.(d) In the dynamic case, the optimal inner radius is found to be 3.5 mm, when the outer radius is kept constant at 10.5 mm and the inner radius is varied.*
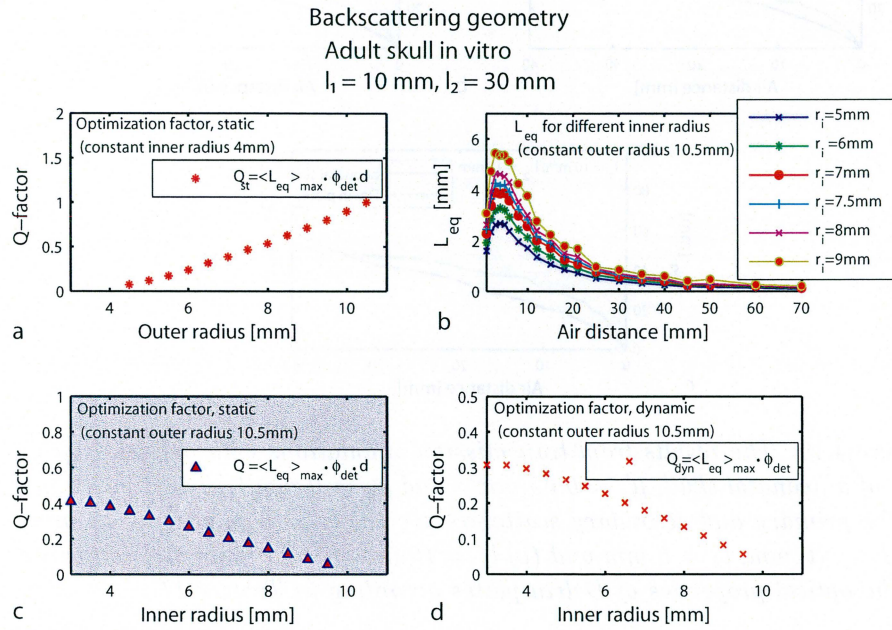
Figure 4.18: *Optimal detection dimensions for adult skull in vitro $l_1 = 10$ mm and $l_2 = 30$ mm, $\mu'_s = 2.0$ mm^{-1} and $\mu_a = 0$ mm^{-1} in backscattering geometry. (a) The optimal outer radius is found to be 10.5 mm, when the inner radius is kept constant at 3 mm and the outer radius is varied. (b) The air distance d, corresponding to $< L_{eq} >_{max}$, never reaches a value 10 mm or more, when the outer radius is kept constant at 10.5 mm and the inner radius is varied. (c) The optimal inner radius for the static case is not found, when the outer radius is kept constant at 10.5 mm and the inner radius is varied. The not shaded area shows where the condition $d \geq 10$ mm is fulfilled.(d) In the dynamic case, the optimal inner radius is found to be 3.5 mm, when the outer radius is kept constant at 10.5 mm and the inner radius is varied.*
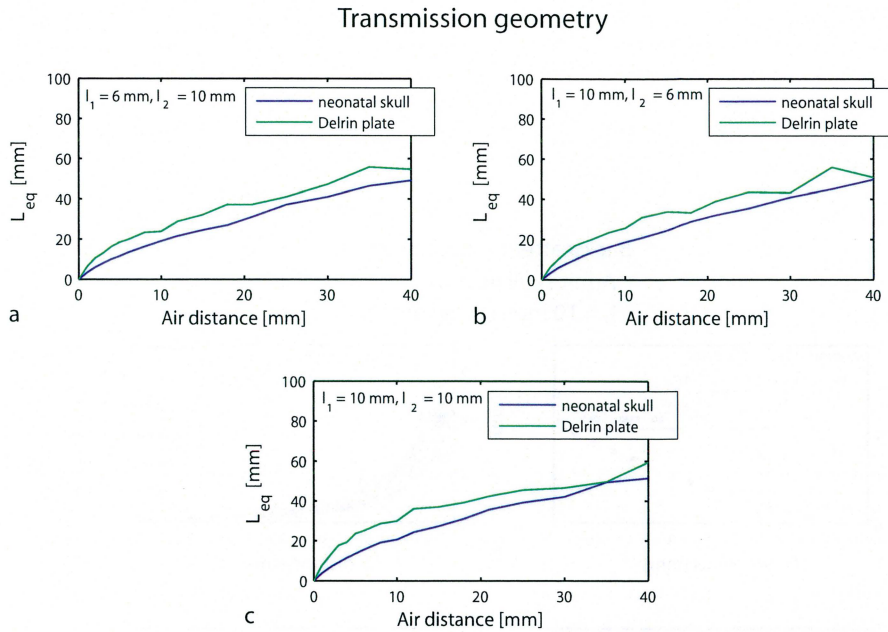
Transmission geometry

Figure 4.19: *The results from transmission simulations with optical proper-ties of a neonatal skull, $\mu'_s = 0.65 \ mm^{-1}$ and $\mu_a = 0 \ mm^{-1}$. The dimensions of the primary and secondary scatterers are (a) $l_1 = 6 \ mm$, $l_2 = 10 \ mm$, (b) $l_1 = 10 \ mm$, $l_2 = 6 \ mm$ and (c) $l_1 = 10 \ mm$, $l_2 = 10 \ mm$ and compared to the optical properties of Delrin plates according to Table 4.11.*

measurements. A primary scatterer thickness of 10 mm unfortunately never fulfills that condition, for any of the reduced scattering coefficients. As men-tioned earlier the most realistic thickness of the primary scatterer, which is a model of the forehead tissue and skull bone, is 10 mm for adults. A dynamic measurement on the other hand is possible for all different thicknesses and reduced scattering coefficients, as well as for investigations of the maxillary sinuses.

A study on how the transmission signal changes when using a reduced scattering coefficient corresponding to neonatal skull (optical properties ac-cording to Table 4.11) is seen in Fig. 4.19.

The effect of a lower reduced scattering coefficient is the same as having a thinner primary and secondary scatterer thickness, which means a smaller L_{eq}, as discussed in Chap. 4.2.2. As when changing the scatterer thicknesses, changing the reduced scattering coefficient does not effect the signal to a larger extent.

4.5 Detection optimization - The diffusion equation

The flux being detected and the maximum value of L_{eq} simulated in ASAP™ for the backscattering geometry, can also be calculated using the diffusion equation and by approximating the plates with Lambertian emitters. This means that the Q_{st}-factor and Q_{dyn}-factor also can be estimated.

4.5.1 Procedure for detection optimization

A good start is to divide this problem into a list of smaller problems and solve the problems step by step. A list of an idea of subproblems with the goal to achieve the Q-factors is presented;

1. Distribution of light transmitted through the primary scatterer.

2. Distribution of light after traveling through the air gap.

3. Distribution of light after diffuse reflectance in the secondary scatterer.

4. Distribution of light after traveling through the air gap the second time.

5. Distribution of light transmitted through the primary scatterer, i.e. final light distribution for light that have traveled through the air gap.

6. Distribution of light directly backscattered in the primary scatterer, also called the short cut photons.

These problems can be solved by using the steady-state diffusion equation for a slab to calculate the transmission and diffuse reflectance. By convolving the achieved light distributions with each other and the equation of a Lambertian emitter, an appropriate value of the detected flux can be modelled.

4.5.2 Calculation of the optimal detection geometry

To solve the first subproblem, the steady-state diffusion equation for a slab (Delrin plate) of thickness l is a good start. The equation is found in Chap. 2.2.3; Eq. 2.44. It was found that there was no need for more than 6 sources, to fulfill the boundary conditions, as source 5 and 6 only gave a small contribution, compared to the other sources; see Fig. 4.20. The positions of the sources are chosen to fulfill the boundary conditions for the fluence rate in the slab, as explained in Chap. 2.2.3. With these 6 point sources the steady-state diffusion equation looks like

$$\phi(\rho, z) = \frac{P\mu_{eff}^2}{4\pi\mu_a} \cdot \left(p\frac{e^{-\mu_{eff}r_1}}{r_1} - \frac{e^{-\mu_{eff}r_2}}{r_2} - \frac{e^{-\mu_{eff}r_3}}{r_3} + \frac{e^{-\mu_{eff}r_4}}{r_4} + \right.$$

$$+ \left. \frac{e^{-\mu_{eff} r_5}}{r_5} - \frac{e^{-\mu_{eff} r_6}}{r_6} \right) \tag{4.4}$$

where

$$r_1 = \sqrt{(z - z_0)^2 + \rho^2} \tag{4.5}$$

$$r_2 = \sqrt{(z + z_0 + 2z_b)^2 + \rho^2} \tag{4.6}$$

$$r_3 = \sqrt{(2l - z - z_0 + 2z_b)^2 + \rho^2} \tag{4.7}$$

$$r_4 = \sqrt{(2l - z + z_0 + 4z_b)^2 + \rho^2} \tag{4.8}$$

$$r_5 = \sqrt{(2l + z - z_0 + 4z_b)^2 + \rho^2} \tag{4.9}$$

$$r_6 = \sqrt{(2l + z + z_0 + 6z_b)^2 + \rho^2} \tag{4.10}$$
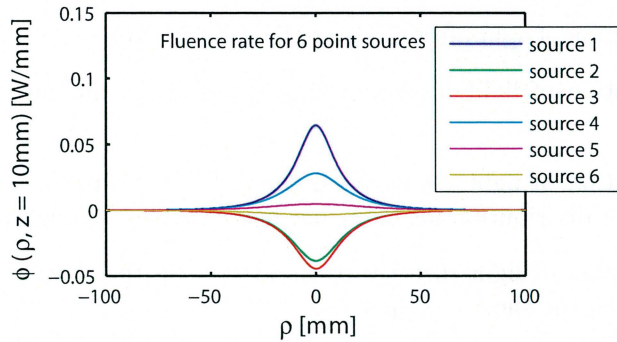
$$\tag{4.11}$$

Figure 4.20: *Contribution to the fluence rate from 6 point sources, at different positions outside the slab, according to Fig. 2.9.*

The definitions of z_0 and z_b are found in Chap. 2.2.3. The value of z_b depends on the refractive indices of the slab and the surrounding medium, in most cases air with n = 1. The Delrin plate has a refractive index of about 1.48 [39], which after some quite lengthy Matlab calculations was found to give $z_b = 2.32 z_0$. See Appendix B for detailed calculations.

To get the distribution of light transmitted through the primary scatterer, the transmission has to be calculated. This is done by using Eq. 2.50 found in Chap. 2.2.3. The value of μ_a was set to 0.0005 mm^{-1} and μ_s' was set to 1.8 mm^{-1}, as in the simulations. This gives $\mu_{eff} = 0.05$ mm^{-1} according to Eq. 2.45. As Fig. 4.20 shows it is sufficient to use 6 sources.

The expression for the transmittance at a depth of $z = 10$ mm, $T_{z=10}$, is convoluted with the expression for a Lambertian emitter, given by Lambert's law (Eq. 4.12), to get the flux reaching the secondary scatterer, ϕ_2
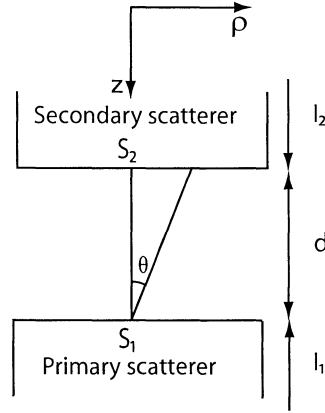
$$I_\theta = I_n cos\theta \tag{4.12}$$

Figure 4.21: *Schematic illustration of a Lambertian emitter (Eq. 4.12) where the angle θ is indicated.*

where I_θ is the intensity at a certain angle θ; see Fig. 4.21. As $I \propto \phi$ the transmitted flux can be convoluted with $cos\theta$, to get ϕ_2.

$$\phi_2 = T_{z=10} * cos\theta \tag{4.13}$$

The distance r, depends on θ and d, as $r = d\sin\theta$.

Next step is to calculate the diffuse reflectance from the secondary scatterer ($d = 30$ mm). This is done by the convolution between ϕ_2 and the expression for diffuse reflection, in Eq. 2.50, using 6 sources.

$$\phi_{2ref} = \phi_2 * R_{z=0} \tag{4.14}$$

As the light continues to the primary scatterer through the air gap, another convolution with $cos\theta$ is necessary.

$$\phi_1 = \phi_{2ref} * cos\theta \tag{4.15}$$

To finally get the flux detected, ϕ_1 is convoluted with the transmittance of the primary scatterer.

$$\phi_{det} = \phi_1 * T_{z=10} \tag{4.16}$$

Also the diffuse reflectance of the primary scatterer ($d = 10$ mm) was calculated with Eq. 2.50, using 6 sources. This flux corresponds to the short cut photons, just entering the primary scatterer.

The result is seen in Fig. 4.22. In Fig. 4.22 (a) it is seen how a central beam stopper will absorb a larger fraction of the short cut photons, than the photons with oxygen imprint. It is also seen that the two fluxes get equally big as far out as at a radius of about 70 mm, which is far beyond the radius of the detector, which is 10.5 mm. This shows the bad starting point, when trying to measure the equivalent mean path length in air.
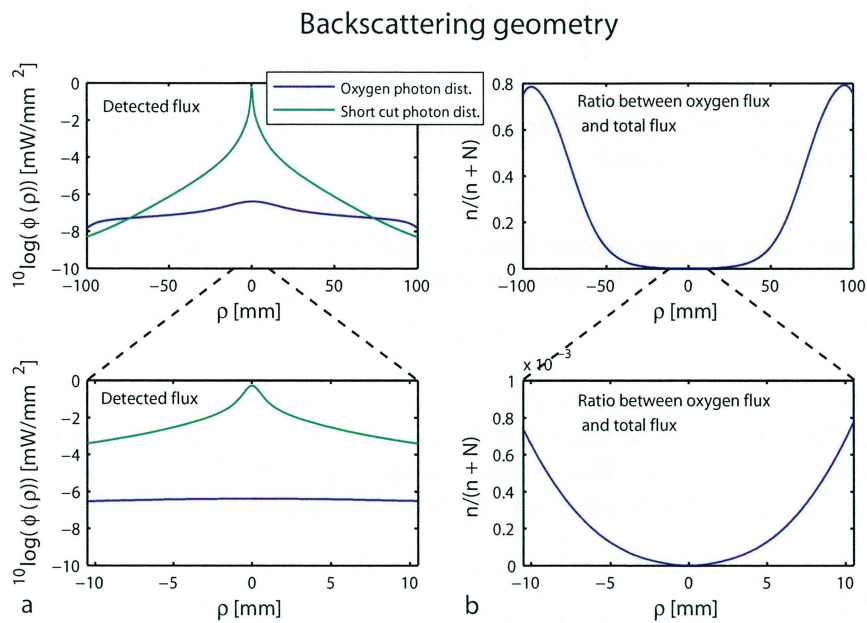
Backscattering geometry

Figure 4.22: *(a) Flux as a function of radius for directly backscattered photons and photons with an oxygen imprint, an enlargement within the detection radius is also plotted. (b) The fraction of photons with an oxygen imprint out of all injected photons, an enlargement within the detection radius is also plotted.*
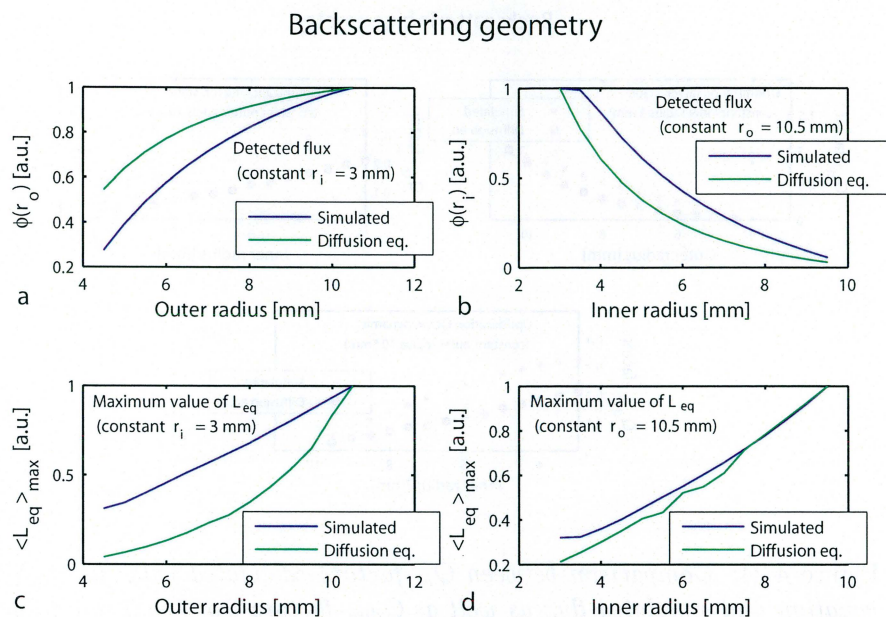
Backscattering geometry

Figure 4.23: *Comparison between flux calculated with the diffusion equation and simulated flux as well as between maximum values of L_{eq} from the diffusion equation and from simulations. (a) Flux as a function of outer radius with constant inner radius of 3 mm. (b) Maximum value of L_{eq} as a function of outer radius with a constant inner radius of 3 mm. (c) Detected flux as a function of inner radius with a constant outer radius of 10.5 mm. (d) Maximum value of L_{eq} as a function of inner radius with a constant outer radius of 10.5 mm.*

Fig. 4.22 (b) shows the ratio between photons with oxygen imprint and short cut photons. It is clearly seen that the fraction of photons with oxygen imprint, increases with the radius.

The fluxes and maximum values of L_{eq} was calculated for different outer detection radiuses and fixed detection inner radius and vice versa, in Matlab and compared with those from the simulations, as seen in Fig. 4.23.

The calculated and simulated curves follows the same behavior quite nice.

Finally the Q_{st}- and Q_{dyn}-factors were calculated according to Eqs 4.2 and 4.3 and plotted together with the simulated Q_{st}- and Q_{dyn}-factors. The result is seen in Fig. 4.24.

Also here the behavior of the calculated factors and the simulated are similar. The optimal detection dimensions are therefore the same as when using the simulations. To calculate the static optimized detection dimensions the values of d corresponding to the maximum value of L_{eq} had to be
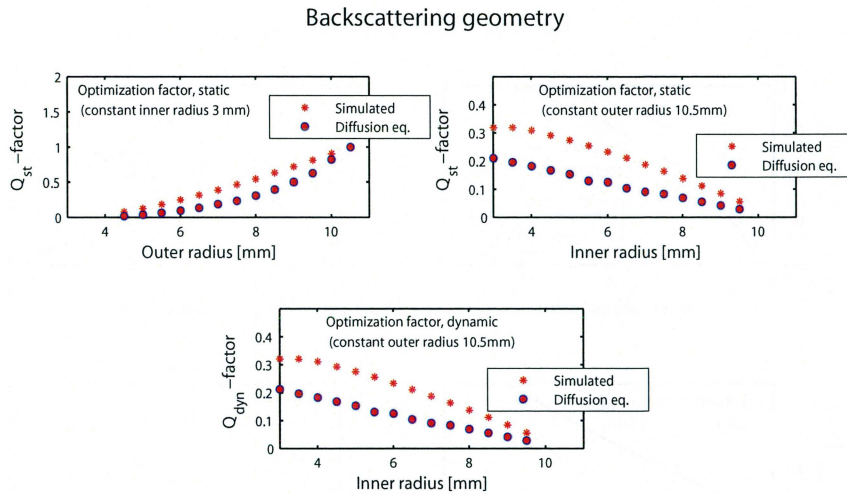
Backscattering geometry

Figure 4.24: *Comparison between Q_{st}-factors calculated with the diffusion equation and simulated flux as well as Q_{dyn}-factors from both the diffusion equation and simulations. (a) Q-factor as a function of outer radius with constant inner radius of 3 mm. (b) Static Q-factor as a function of inner radius with a constant outer radius of 10.5 mm.*

taken from the simulations. This means that as it is the geometry $l_1 = 10$ mm and $l_2 = 30$ mm, there is no inner detection radius giving $d \geq 10$. In the dynamic case an inner detection radius of 3 mm is the optimal dimension.

The major source of error is that the diffusion equation is an approximation requiring diffuse light, while the simulations follows a stochastic model, without requirements. The plates are approximated to Lambertian emitters, which might influence the result.

4.6 Imaging of the frontal sinuses

There are many similarities between the frontalis imaging model and the backscattering phantom model described in Chap 4.2.1. Unfortunately, in the imaging case there are no experimental results to compare the simulation results with. The aim of the simulation is to investigate whether there is a possibility to spatially resolve the frontal sinuses and to guide a possible development of such a GASMAS imaging system of the frontal sinuses; see ASAP^{TM} code in Appendix E.

Identical detection and light source models as in the backscattering model are used (see Chap. 4.2.1) and are therefore not discussed in this chapter. Two different geometrical models were studied, one with the frontalis situated at a depth of 10 mm and the other at a depth of 5 mm. The purpose

of this is to somewhat cover the human variations of the frontalis positions. The model of the head consist of one single scattering block representing the tissue covering the sinuses (bone, muscle, skin, brain etc.) where all three dimensions are (in terms of biophotonics) considered to be infinitely large. Since not only the depths of the frontalis variate from human to human but also their geometrical shape, no exact model of these have been created. Naturally, many different simulations could be performed to once again cover the human variations but since the purpose of the simulation is to only investigate the possibility for spatial imaging this was not done. It should also be mentioned once again that not only does the shape of the frontal sinuses variate, they also vary from being bilateral to only one single cavity. The shape of the sinuses is set in the simulations to be elliptical, with the dimensions $20 \times 25 \times 10$ mm. Fig. 4.25 shows the model of the head and the sinuses, where the dimensions of the scattering block are indicated.
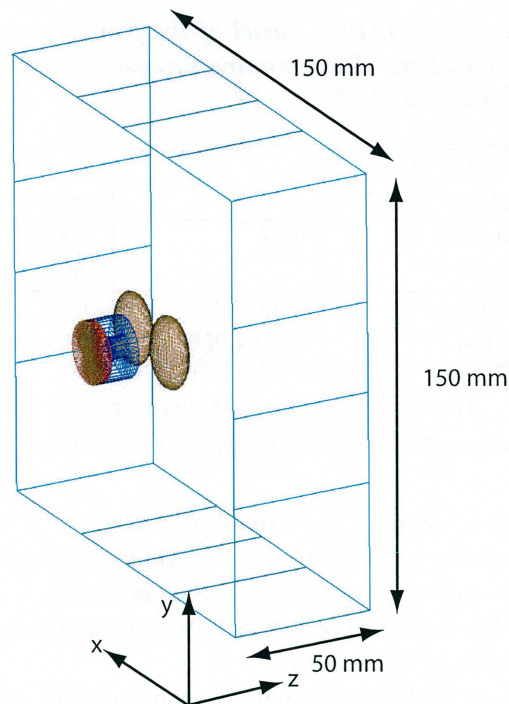

Figure 4.25: *The ASAP^{TM} model used to simulate the frontal sinuses. The backscattering detection system is also shown.*

To perform simulations of the model the head is scanned by moving the detection and light source system 2 mm in the x direction and 4 mm in the y direction (indicated in Fig. 4.25).

Fig. 4.26 shows a closeup on the sinuses and the detection system that was used in the simulations. Every scanning point is simulated with 500 000
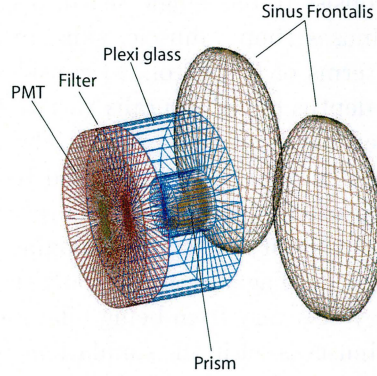
Figure 4.26: *The ASAP^{TM} model of the frontal sinuses and backscattering the detection system. The scanning process is performed on the x-y plane, indicated in the Fig. 4.25.*

Optical properties	μ_s [mm^{-1}]	g	μ'_s [mm^{-1}]	μ_a [mm^{-1}]
Adult skull in vitro	16	0.87	2.0 [49] (800 nm)	NA
Neonate skull in vivo	9.3	0.93 [52] (650 - 950 nm)	0.65 [51] (761 nm)	NA

Table 4.13: *The optical properties used in the image simulations of the frontal sinuses, valid wavelength regions are seen in brackets.*

rays, enough to create a good photon statistic.

As previously mentioned, two different geometries were studied. Additionally, the optical properties in both geometries were varied to represent the difference in optical properties between adults and neonates. The values used are shown in Table 4.13.

One way to evaluate the spatial resolution is to study the cross section of the simulation and compare this with the mathematical shape of the sinuses, described by real parts of Eq. 4.17.

$$Sinus_{math} = 10 \cdot \sqrt{1 - \frac{(x + 12.5)^2}{100}} + 10 \cdot \sqrt{1 - \frac{(x - 12.5)^2}{100}} \qquad (4.17)$$

Here, x is the x-coordinate used in the simulation. The analysis is done by varying the radius of the detection aperture and comparing the resulting cross sections with Eq. 4.17.

Before any analysis of the spatial resolution can be done, one must consider all terms which will influence the results. The maximum value for the equivalent mean path length ($< L_{eq} >_{max}$) is important since a high value is easier to measure. Since the sinuses are separated by 5 mm, a low value of the equivalent mean path length at $x = 0$ ($< L_{eq} >_{min}$) is thus equivalent with good spatial resolution. Naturally the shape of the cross section is important. This term is described with the full width at half maximum ($FWHM_{sim}$), which is compared to the value for the mathematically described sinus cross section $FWHM_{math}$ by dividing the two values. Hence, $\frac{FWHM_{math}}{FWHM_{sim}} \approx 1$ indicates a good spatial resolution. To be able to actually measure any signal, also the flux must be considered. Note, that a high flux does not influence the spatial resolution, but is a required term to perform any experimental measurement. A so called Q_{image}-factor (Eq. 4.18), describing the influence of the terms discussed above, was formed to find the ultimate value for the radius of the detection aperture.

$$Q_{image} = \underbrace{(< L_{eq} >_{max} - < L_{eq} >_{min})}_{term1} \cdot \underbrace{\frac{< L_{eq} >_{max}}{< L_{eq} >_{min}}}_{term2} \cdot \underbrace{\frac{FWHM_{sim}}{FWHM_{math}}}_{term3} \cdot \underbrace{Flux_{sum}}_{term4}$$

(4.18)

Here the total flux of the entire cross section is denoted $Flux_{sum}$. As can be seen the term ($< L_{eq} >_{max} - < L_{eq} >_{min}$) is added, due to the importance of having a large difference between the two values. The margin of error in the experimental setup is at best about $L_{eq} = \pm 1$ mm. Hence, the difference in value between $< L_{eq} >_{max}$ and $< L_{eq} >_{min}$ must be larger than 2.

To be able to compare Q_{image}-values received from different simulations it must be normalized, where a value of zero represents no spatial resolution and perfect spatial resolution is given the value one. Therefore, every term given in Eq. 4.18 is divided with the maximum value of the term itself. Hence, the maximum value for each term will thus be one, resulting in a maximum value of one for the Q_{image}-factor.

4.6.1 Simulations using adult properties

To begin, let us fist consider the optical properties of an adult skull ($g = 0.87$, $\mu_s = 16$ mm^{-1} and $\mu_a = 0$ mm^{-1}) and the frontal sinuses located at a depth of 5 mm. Fig. 4.27 (a) shows the frontal view of the head, with the equivalent mean path length given by the color bar. The figure shows how the signal changes when measuring at different positions. The real location of the sinuses are added for illustration purposes only. Fig. 4.27 (b) shows a tilted view of the entire measurement.

The detection aperture used in Fig. 4.27 has an inner and outer radius of 5 mm and 10.5 mm respectively, which are the values that so far has been used experimentally.
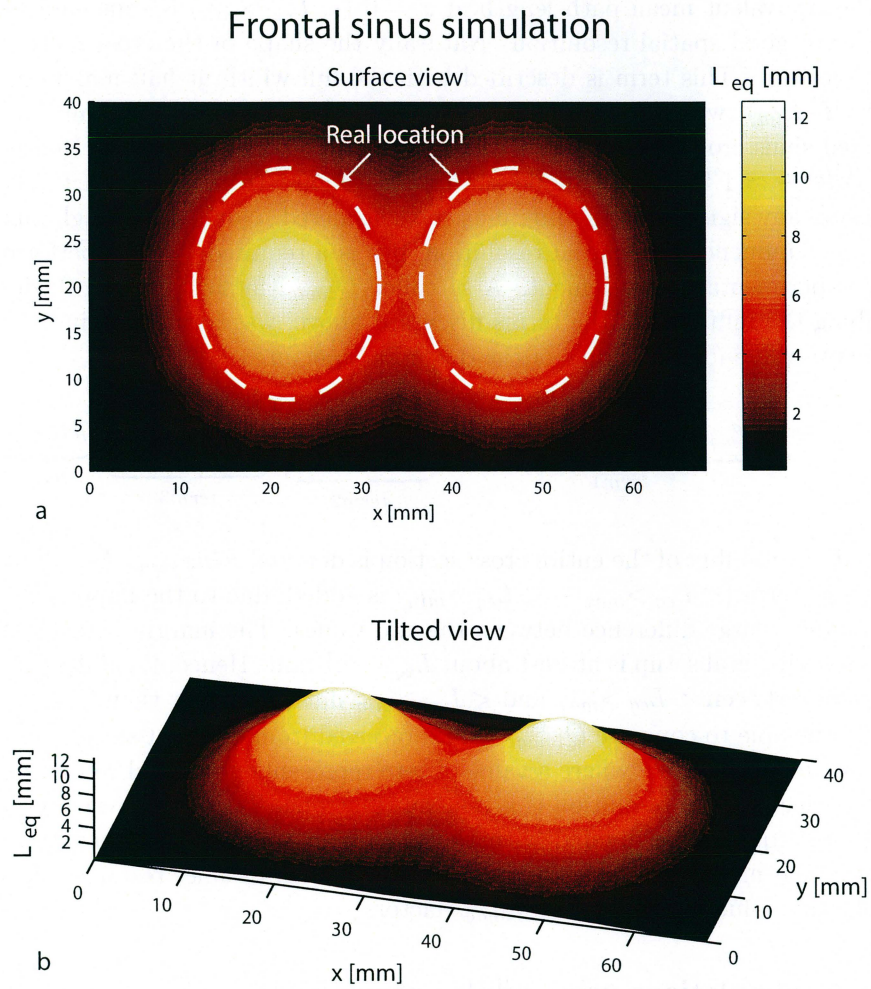
Frontal sinus simulation

a

b

Figure 4.27: (a) The front view of the frontal sinuses (at a depth of 5 mm); simulation with backscattering detection and adult optical properties according to Table 4.13. A detection aperture with an inner and outer radius of 5 mm and 10.5 mm, respectively, was used. The location of the real sinuses is also indicated in the figure. (b) A tilted view of (a).

To investigate the optimal detection aperture the Q_{image}-factor according to Eq. 4.18 has been studied. In Fig. 4.28 the behavior of the different terms describing the Q_{image} are plotted.
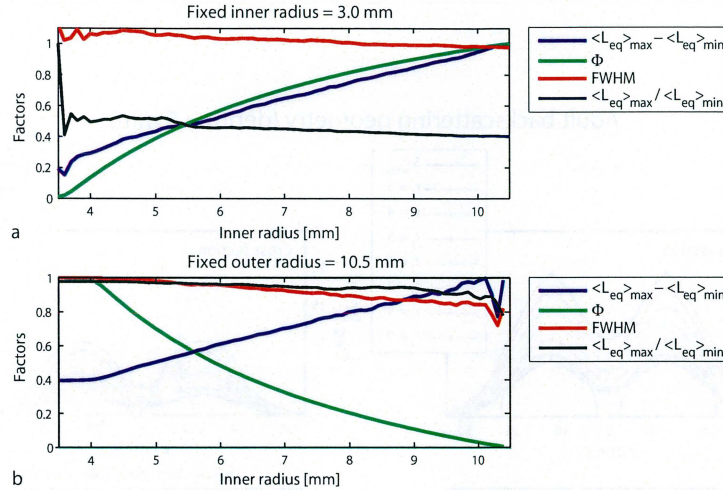

Figure 4.28: *The behavior of the four factors described in Eq. 4.18. The simulations are performed with backscattering geometry on the frontal sinuses located at a depth of 5 mm. (a) In this case a constant inner radius of 3 mm was used and in (b) a constant outer radius of 10.5 mm was used. As can be seen, the main difference between the two measurements is the flux.*

In Fig. 4.28 (a) and (b) one can see that the flux is the main difference between the two techniques (constant inner radius or constant outer radius). One should note that even though the behavior of the four terms shown in Fig. 4.28 (a) seems more favorable this will later on be shown not to be true, due to the condition $< L_{eq} >_{max} - < L_{eq} >_{min} > 2$.

Fig. 4.29 (a) shows seven cross sections all having a detection aperture with a constant outer radius of 10.5 mm. In Fig. 4.29 (b) a constant inner radius of 3 mm was used to produce the cross sections. Fig. 4.29 (c) and (d) show the resulting Q_{image}-values for both cases, calculated according to Eq. 4.18.

As can be seen, high values of the equivalent mean path length are received, due to the relatively superficial position of the sinuses. When having a constant outer radius, the requirement $< L_{eq} >_{max} - < L_{eq} >_{min} > 2$ is fulfilled for all values for the inner radius. As can be seen in Fig. 4.29 (c), the Q_{image}-value does not vary until the inner radius reaches 4 mm, where it decreases. The maximum value $Q_{image} = 0.4$ occurs at an inner radius of 3.6 mm and an outer radius of 10.5 mm. However, higher values on the inner radius can still be used, thus increasing the equivalent mean path length, without loosing much spatial resolution. Since the dominating
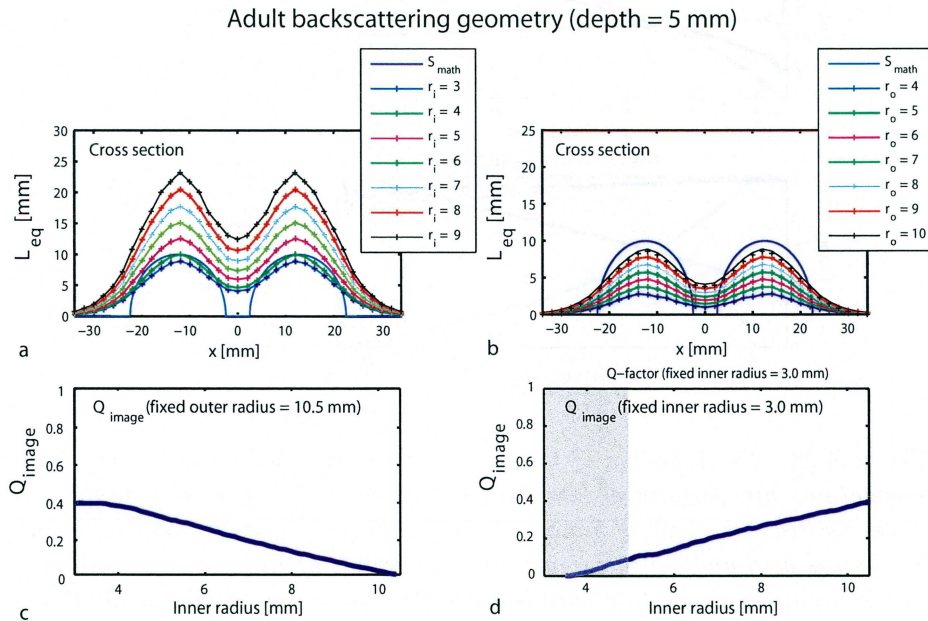
Figure 4.29: *Result from the imaging simulation on the frontal sinuses with the backscattering geometry, where the optical parameters of an adult were used (according to Table 4.13). (a) Cross sections where a detection aperture with a constant outer radius of 10.5 mm was used. The inner radius was varied between 3 mm and 9 mm. (b) The cross sections received when having a detection aperture with a constant inner radius of 3 mm and varying the outer radius. (c) The calculated Q_{image}-values for an inner radii varied from 3 mm to 10.4 mm. The maximum Q_{image}-value is approximately 0.4. (d) The calculated Q_{image}-values for the measurement shown in (b). The shaded area indicates when the requirement $< L_{eq} >_{max} - < L_{eq} >_{min} > 2$ is not fulfilled. The maximum Q_{image}-value is in this case also approximately 0.4.*

term is the flux, it will thus limit the investigation. By increasing the inner radius in the measurement shown in Fig. 4.29 (a), much is gained in the term $< L_{eq} >_{max} - < L_{eq} >_{min}$ (the second most dominating term).

When instead the inner radius of the detection aperture is kept constant, some values for the outer radii do not fulfill the condition discussed above. The two measurements both result in a maximum Q_{image}-value of 0.4.

By instead moving the frontal sinuses to a depth of 10 mm, still using the optical parameters for an adult ($g = 0.87$, $\mu_s = 16$ mm^{-1} and $\mu_a = 0$ mm^{-1}), worse spatial resolution is expected. Fig. 4.30 shows both the frontal and tilted view of the result from the simulation.

As expected, the measurement result in a slightly more blurred image of the sinuses, but as can be seen, the shape of two ellipsoidal sinuses are clearly visible. The values for the equivalent mean path length, also indicated in the figure, are reduced, going from a maximum value of roughly 12 mm (when the sinuses are located at a depth of 5 mm) to 3.5 mm. This is a consequence of having deeper located sinuses. If any spatial resolution is to be seen in the experimental setup high values on the inner radius of the detection aperture must be used. Naturally, this will have great effect on the flux, which decreases when increasing the inner radius. The cross sections for the values of the detection aperture used in Fig. 4.29 (a) and (b) are plotted in Fig. 4.31 (a) and (b). The resulting Q_{image}-values from these two simulations are shown in Fig. 4.31 (c) and (d), respectively.

In Fig. 4.31 (a) one can see how the smoothness of the curves resulting when having a detection aperture with a fixed outer radius is lost when using higher values on the inner radius. This could be due to worse photon statistic, which might be expected when studying deeper located sinuses. As can be seen, the resulting Q_{image}-values, shown in Fig. 4.31 (c), are heavily reduced. The maximum value is found to be approximately 0.04, received when the inner radius is 9.5 mm (with a fixed outer radius of 10.5 mm). The not shaded area indicates when the requirement $< L_{eq} >_{max} - < L_{eq} >_{min} > 2$ mm is fulfilled. As previously mentioned, when using such a high value on the inner radius (9.5 mm), the flux is so heavily reduced that any measurements might be difficult to perform. The limitation is mostly, as discussed above, set by the experimental setup used. One way might be to increase the scanning time for each point, but if this is possible depends on the measurement.

4.6.2 Simulations using neonatal properties

As mentioned above, simulations on the neonatal is done by using the optical parameters $g = 0.93$, $\mu_s = 9.3$ mm^{-1} and $\mu_a = 0$ mm^{-1}. Like before, two simulations were performed, one where the sinuses were positioned at a depth of 5 mm and the second at 10 mm. It should once again be added that neonates do not actually have frontal sinuses, they grow with age. Still,
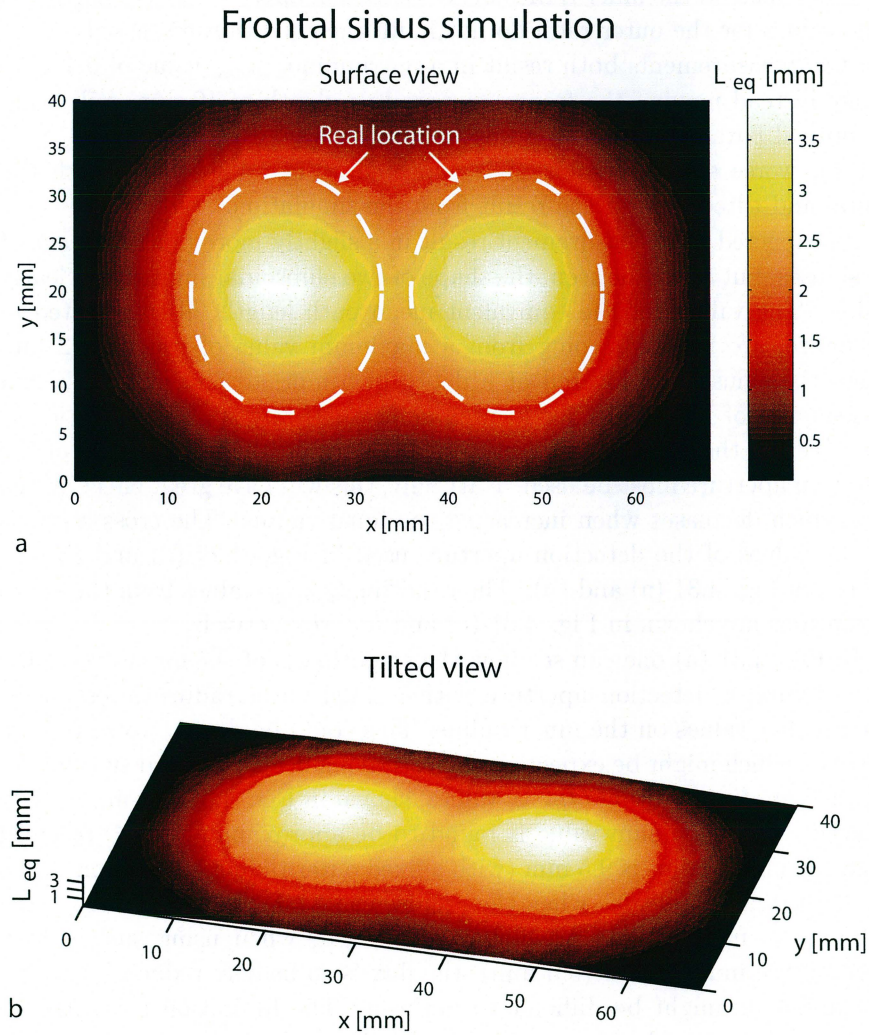
Figure 4.30: *(a) The front view of the frontal sinuses (at a depth of 10 mm) simulation with backscattering detection and adult optical properties according to Table 4.13. A detection aperture with an inner and outer radius of 5 mm and 10.5 mm, respectively, was used. The location of the real sinuses is also indicated in the figure. (b) A tilted view of (a).*
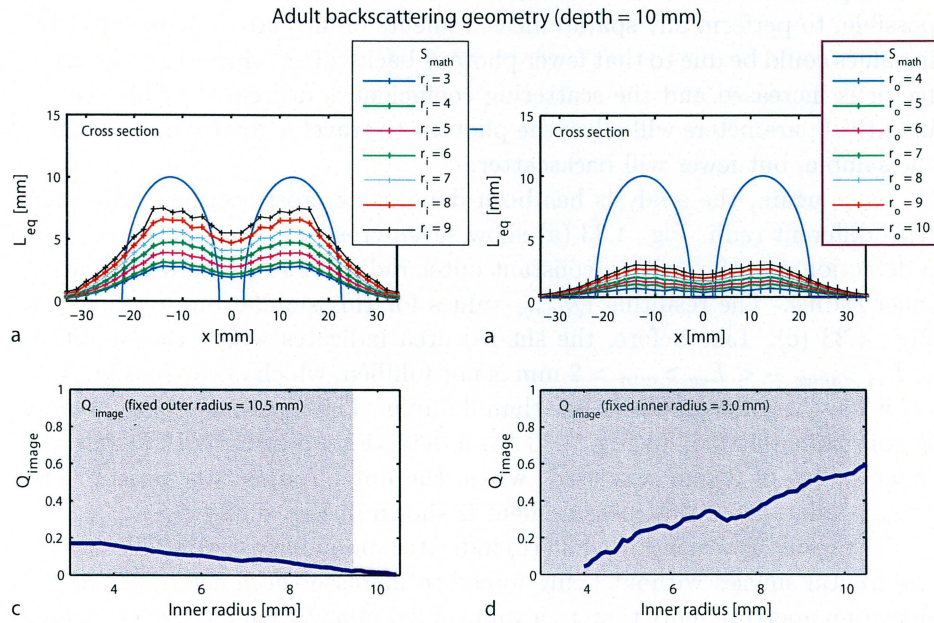
Figure 4.31: *The figure shows the result from the simulations where the frontal sinuses of an adult (according to Table 4.13) are located at a depth of 10 mm. (a) Cross sections with a detection aperture with a constant outer radius of 10.5 mm, where the inner radius is varied between 3 mm and 9 mm. (b) Cross sections with a detection aperture with constant inner radius of 3 mm. (c) and (d) The calculated Q_{image}-values for the two measurements. If the requirement $< L_{eq} >_{max} - < L_{eq} >_{min} > 2$ is not fulfilled it is, like before, indicated with the shaded area. In (c) the maximum Q_{image}-value is approximately 0.04, which is received when having a inner radius of 9.5 mm. As can be seen in (d), the requirement is not fulfilled for any values of the outer radius of the detection aperture.*

there might be a possibility to actually follow the development of the sinuses, especially because the sinuses are located very superficially when growing.

Fig. 4.32 (a) and (b) show, a frontal and a tilted view of the imaging.

The detection aperture used in Fig. 4.32 has an inner radius of 5 mm and an outer radius of 10.5 mm. As can be seen, the value for the equivalent mean path length is lower compared to an adult with sinuses also positioned at a depth of 5 mm. This indicates that it will be more difficult, but still possible, to perform any spatial measurements on neonates. This reduction in values could be due to that fewer photons backscatter, since the anisotropy factor is increased and the scattering coefficient is decreased. This change in optical parameters will allow the photons to travel a greater distance into the sample, but fewer will backscatter.

Once again, the analysis has been done using cross sections, measured with different radii. Fig. 4.33 (a) show seven cross sections, measured with a detection aperture with a constant outer radius of 10.5 mm and a varied inner radius. The resulting Q_{image}-values for this simulation are shown in Fig. 4.33 (c). Like before, the shaded area indicates where the condition $< L_{eq} >_{max} - < L_{eq} >_{min} > 2$ mm is not fulfilled, which occurs in Fig. 4.33 (c) when the inner radius is less than 3.6 mm. The maximum Q_{image}-value is approximately 0.5. In Fig. 4.33 (b) a detection aperture with a constant inner radius of 3 mm was used, where the outer radius was varied. The Q_{image}-values from this measurement is shown in Fig. 4.33 (d).

The result shown in Fig. 4.33 (c) indicate a possibility to spatially resolve the frontal sinuses without being forced to increase the inner radius of the detection aperture more than to a value of 3.6 mm. When having a constant inner radius there is, as can be seen in Fig. 4.33 (d), no possibility to spatially resolve the sinuses.

When moving the sinuses to a depth of 10 mm the equivalent mean path length is heavily reduced and no spatial resolution is possible. Although it might appear as though the sinuses are slightly resolved in Fig. 4.34, this is impossible to see using the current experimental technique.

As can be seen, the simulation result in a strange behavior. The reason for this could be poor photon statistics. The values for the equivalent mean path length are very low so small deviations will therefore be more visible.

The reduction of the equivalent mean path length is clearly shown in Fig. 4.35 (a), shows seven cross sections measured with a detection aperture with a constant outer radius of 10.5 mm and where the inner radius is varied. The resulting Q_{image}-values for this simulation are shown in Fig. 4.35 (c) and as can be seen, even though the values are approximately the same as for an adult, the requirement discussed above is unfortunately never reached. Fig. 4.35 (b) show six cross sections measured with a constant inner radius of 3 mm. The resulting Q_{image}-values for this simulation are plotted in Fig. 4.35 (d). No values of the outer radius fulfill the requirement.

Since neither of the measurements fulfill the requirement, this unfortu-

Frontal sinus simulation

Surface view

Tilted view

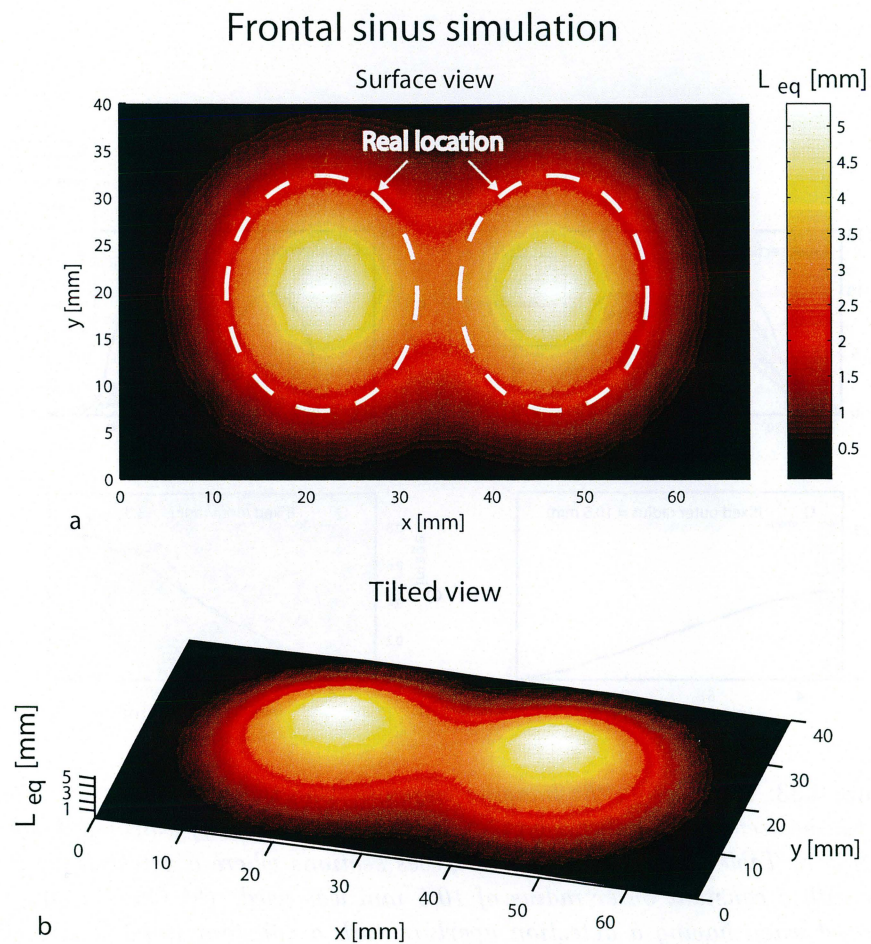Figure 4.32: *Simulations on the frontal sinuses (at a depth of 5 mm) performed using the optical parameters of a neonatal (according to Table 4.13). (a) The front view of the simulation with backscattering detection. A detection aperture with an inner and outer radius of 5 mm and 10.5 mm, respectively, was used. The location of the real sinuses is also indicated in the figure. (b) A tilted view of (a).*

Figure 4.33: *Result from the imaging simulation on the frontal sinuses with the backscattering geometry, where the optical parameters of a neonatal (according to Table 4.13) was used. (a) Cross sections where a detection aperture with a constant outer radius of 10.5 mm was used. (b) Cross sections received when having a detection aperture with a constant inner radius of 3 mm and varying the outer radius. (c) The calculated Q_{image}-values from (a), having a maximum value of approximately 0.47 at an inner radius of 3.6 mm. (d) The calculated Q_{image}-values for the measurement shown in (b). The shaded area indicates where the difference between $< L_{eq} >_{max}$ and $< L_{eq} >_{min}$ is not larger than 2 mm. In this case, this is never fulfilled.*

Figure 4.34: *(a) The front view of the frontal sinuses simulation with backscattering detection and optical properties of a neonatal (according to Table 4.13). A detection aperture with an inner and outer radius of 5 mm and 10.5 mm, respectively, was used. The location of the real sinuses is also indicated in the figure. (b) A tilted view of (a).*
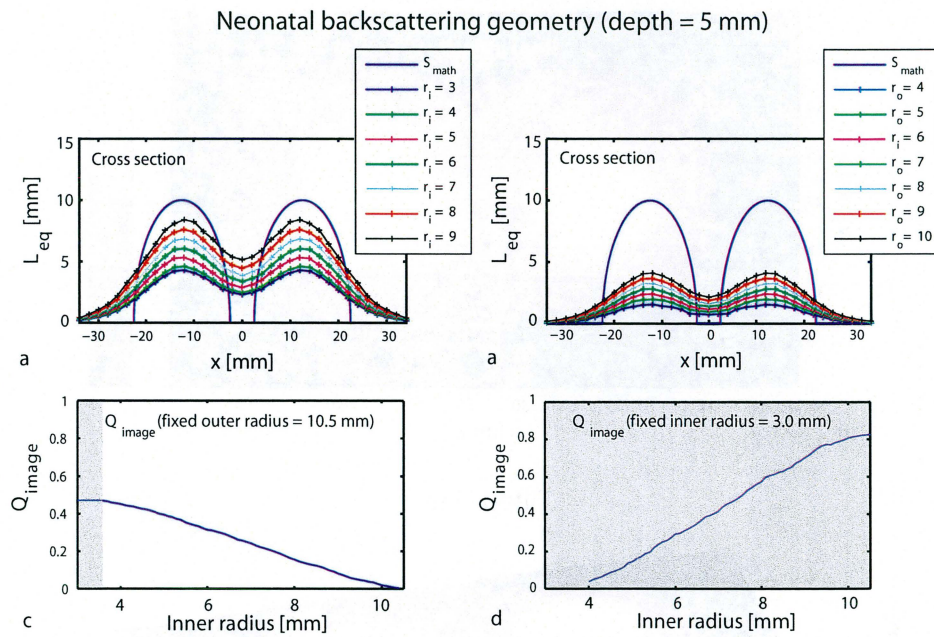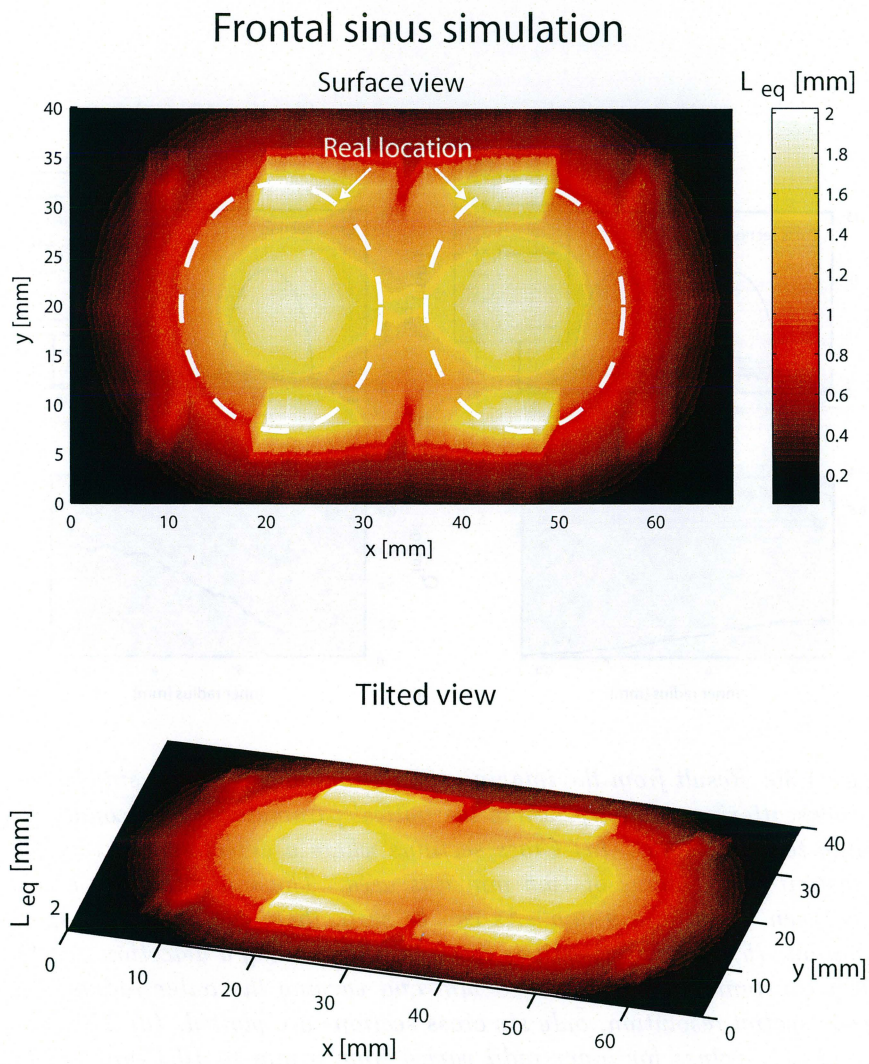
Neonatal backscattering geometry (depth = 10 mm)
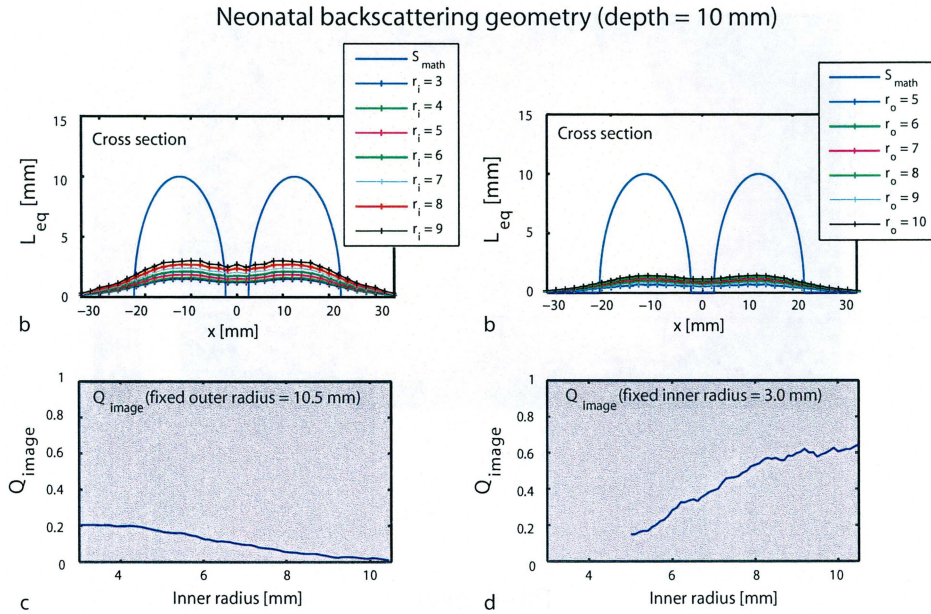
Figure 4.35: *Result from the imaging simulation on the frontal sinuses with the backscattering geometry, where the optical parameters of a neonate (according to Table 4.13). (a) Cross sections where a detection aperture with a constant outer radius of 10.5 mm was used. The inner radius was varied between 3 mm and 9 mm. As can be seen, there are almost no spatial resolution. (b) The cross sections received when having a detection aperture with a constant inner radius of 3 mm and varying the outer radius. Due to poor spatial resolution, only six cross sections are plotted. (c) The calculated Q_{image}-values for inner radii varied from 5 mm to 10.4 mm. In this case the requirement $< L_{eq} >_{max} - < L_{eq} >_{min} > 2$ mm is not fulfilled for any values of the inner radius, which also is the case in (d), where the Q_{image}-values for a fixed inner radius are plotted.*

nately means that with the currently used measuring technique, the frontal sinuses at a depth of 10 mm cannot be spatially resolved, if the optical parameters of the skull are similar to those of a neonatal.

The simulation time depends mostly on the optical parameters used, but does not vary much. The imaging has a total of 385 measuring points, but only 108 was simulated (due to symmetry). Using the adult parameters the simulation time for each measuring point is approximately 4 hours. Thus, the total time needed for one imaging simulation is around 18 days.

4.7 Imaging of the maxillary sinus

The simulations of imaging of the maxillary sinuses of an adult (according to Table 4.13) was performed using the transillumination detection geometry. The light source is inserted, simulating an optical fibre that is in contact with the wall of the oral cavity. The aim of the simulation is, much like the aim of the imaging of the frontal sinuses, to investigate if any spatial resolution can be obtained. In this model no scanning is needed, since the source is situated at the same position during the entire study. The scanning (moving the detector) is instead programmed after the simulation has been done using Matlab. To be able to do this a layer with a thickness of 3 mm and with a higher refractive index ($n = 1.53$) was added outside the head, with the purpose to simulate the filter which must be used in the detection system. Outside this filter a virtual extended detector is added, having the exact shape of the head but with a 4 mm larger radius. A view of the model is shown in Fig. 4.36 (a), (b) and (c). The dimensions of the head were set to $150 \times 250 \times 200$ mm and for the sinus $30 \times 35 \times 40$ mm (both indicated in the figure).

Even though the maxillary sinus is situated on each side of the head only one sinus was added to the model, due to symmetry.

A total of 3200000 rays was needed to achieve good photon statistics. The reason for this large number of rays was due to the relatively large dimensions of the objects.

Fig. 4.37 (a) shows the frontal view of the result. Note the extremely high values of the equivalent mean path length, which is due to the large dimension of the sinus and multiply reflections occurring in the sinus. The result could be compared to the results shown in Fig. 4.5 where the values on the equivalent mean path length is much lower. The reason for the higher values is because the shape of the sinus is elliptical and smooth, thus increasing the probability for multiple reflections. Also, the light can escape in the air gap between the Delrin plates, due to the finite extension of the plates. This cannot occur in the maxillary sinus simulation.

As can be seen in Fig. 4.37 (b) the maximum flux reaching the detector is approximately 0.7 percent. If this is sufficient depends on the equipment
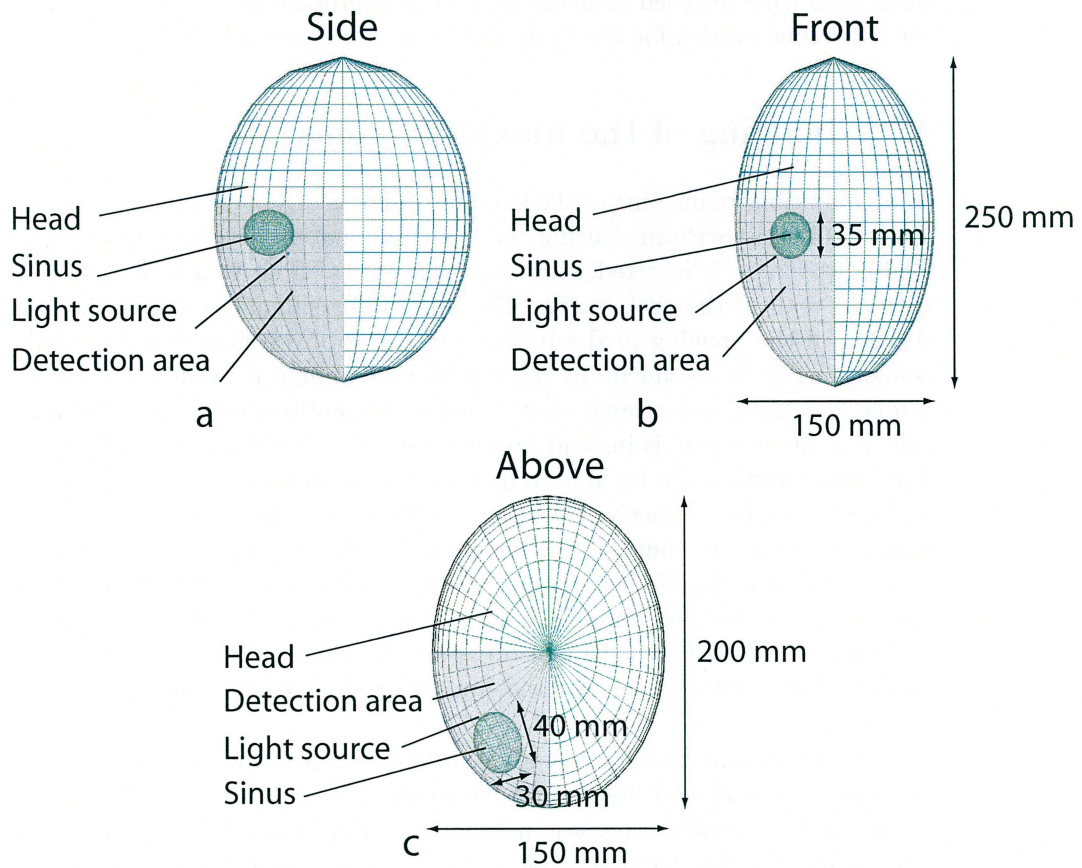
Figure 4.36: *(a) The side view of the model used to simulate the maxillary sinus in the transmission geometry. The head, sinus, light source and detection area are indicated in the figure. (b) The front view of the model. (c) The model seen from above.*
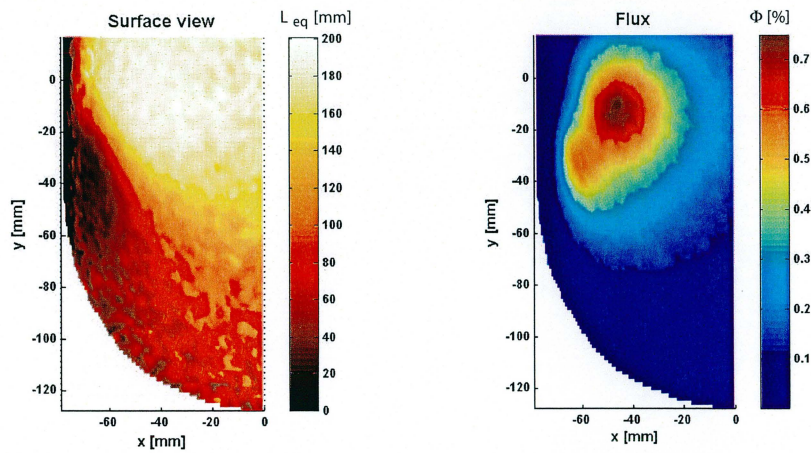
Figure 4.37: *(a) The frontal view of the result from the simulations of imaging of the maxillary sinuses on an adult (according to Table 4.13) in the transmission geometry. The equivalent mean path length is indicated according to the color bar. Note the high values of the equivalent mean path length, reaching values as high as 200 mm. (b) The flux shown in the frontal view of the simulation. Here the percentage of the total flux reaching each measuring point is shown. As can be seen, the flux reaches a maximum value of approximately 0.7 percent.*

used. The reason for the low values on the flux is due to the large dimensions.

The light is directed towards the sinus and the flux on the detection side is shown in Fig. 4.37 (b). It should be noted that the location of the maximum flux is highly related to the position of the light source, as well as its direction.

Chapter 5

Conclusions

There are many sources of error, when comparing the experimental results obtained when performing sinus phantom measurements of the equivalent mean path length with the simulated results. It is difficult to make the experimental measurements as perfect as the simulations, when it comes to dimensions of the plates, apertures and air distances. It is also difficult to measure the optical properties of the plates used in the experiment and without good knowledge of those, there is no possibility of exact agreement between the experiments and the simulations. Despite all this, it is clearly seen that the experiments and simulations agree well in the gross structures.

It is also important to mention that some studies that are possible to perform with simulations, are impossible to achieve from experiments. A good example of this is the study of the number of multiple passes of light over the air gap (symbolizing the sinuses in the phantom) between the two scatterers (symbolizing the covering tissue around the sinuses in the phantoms).

There is no universal optimal detection aperture for static backscattering measurements. It depends on the thicknesses of the scatterers and their optical properties. It is seen though, that for some thicknesses and some lower reduced scattering coefficients, it is possible to achieve an optimal detection aperture and also to perform a static measurement. A dynamic study is possible for all different scatterer thicknesses and optical properties and there is a universal detection aperture. The optimization of the detection apertures would be very time consuming experimentally, why the simulations are very useful. Similar results as from the simulations were achieved with the diffusion equation, showing that there are future possibilities for studies with the diffusion equation. The detection aperture does not affect the transmission measurements in a larger extent, neither does the optical properties.

The study of the imaging potential of the human sinuses using the GAS-MAS technique for backscattering detection measurement, shows possibil-

ities for good resolution of the frontal sinuses. The results also show that there is no universal detection aperture, since this depends on the thickness of the skull bone and the optical properties. By using additional information from, e.g., a computer tomography image or an ultrasound image on a patient, one might be able to determine if any imaging measurement is possible to perform.

It is, as previously mentioned, difficult to experimentally measure signals with such great carefulness that is achieved in the simulations. Although, as the modern technology improves, so do the measuring techniques and thus the measurement range.

In the case of transmission measurements on the maxillary sinus, simulation also shows a possibility for imaging. Due to the relatively large size of these sinuses, high equivalent mean path length values are obtained.

Chapter 6

Acknowledgements

Bibliography

[1] L. Persson et al., "On the potential of human sinus cavity diagnostics using diode laser gas spectroscopy", *Applied Physics B*, **82**, 313 – 317 (2005)

[2] *Health Matters*, Sinusitis, Nat. Inst. of Allergy and Infectious Diseases, US Dept. of Health and Human Services, Bethesda (2005)

[3] M. Sjöholm et al., "Analysis of gas dispersed in scattering media", *Opt. Lett.*, **26**, 18 (2001)

[4] J. Alnis et al., "Laser spectroscopy of free molecular oxygen dispersed in wood materials", *Applied Physics B*, **77**, 691 – 695 (2003)

[5] L. Persson et al., "Studies of gas exchange in fruits using laser spectroscopic techniques", *FRUITIC 05*, 12 – 16 September (2005)

[6] M. Andersson et al., "Spectroscopic studies of wood-drying processes", *Optics Express*, **14**, 8 (2006)

[7] S. Svanberg, Differential absorption LIDAR (DIAL) in M. W. Sigrist *Air Monitoring by Spectroscopic Techniques*, Chapter 3, John Wiley & Sons, Inc. (1994)

[8] T. Fujii and T. Fukuchi, *Laser Remote Sensing*, Taylor & Francis Group (2005)

[9] P. Stierna et al., *Aspects on Sinusitis Diagnosis and treatment in adults*, Eli Lilly Sweden AB, (1996)

[10] H. Haken and H. C. Wolf, *The Physics of Atoms and Quanta*, Springer-Verlag, Berlin Heidelberg 2004

[11] H. Ibach and H. Lüth, *Solid State Physics an Introduction to Materials Science*, 3rd ed., Springer-Verlag, Berlin Heidelberg (2003)

[12] J.-L. Boulnois, "Photophysical processes in recent medical laser developments: a review", *Lasers Med. Sci.* **1**, 47 – 66 (1986)

[13] A. J. Welch, M. J. C. van Gemert, *Optical-Thermal Response of Laser-Irradiated Tissue*, Chapter 1, 2, 5 and 8, Plenum Press, New York (1995)

[14] S. Svanberg, *Atomic and Molecular Spectroscopy*, Chapter 3, 4th ed., Springer-Verlag, New York, Berlin, Heidelberg (2004)

[15] J. M. Hollas, *Modern Spectroscopy*, Chapter 1, 4-7, 4th ed., John Wiley & Sons Ltd, West Sussex (2004)

[16] http://www.physchem.ox.ac.uk/~ jmbgroup/O2b_ abstract.pdf, 2006-03-10

[17] W. T. Hill III and A. L. Schawlow, "Intracavity absorption detection of magnetic-dipole transitions in $^{18}O_2$ and the determination of the $b^1\Sigma_g^+$ ($v = 2$) state rotational constants", *J. Opt. Soc. Am. B*, **5**, 745 (1988)

[18] G. Herzberg, *Molecular Spectra and Molecular Structure I. Diatomic Molecules*, Page 19 – 20, Van Nostrand Reinhold Company Inc. (1950)

[19] http://www.photometer.com/en/abc/abc_061.htm, 2006-05-28

[20] S. Svanberg, *Atomic and Molecular Spectroscopy*, Chapter 6, 4th ed., Springer-Verlag, New York, Berlin, Heidelberg (2004)

[21] S. Svanberg, *Atomic and Molecular Spectroscopy*, Chapter 4, 4th ed., Springer-Verlag, New York, Berlin, Heidelberg (2004)

[22] C. Abrahamsson, *Time-Resolved Spectroscopy for Pharmaceutical Applications*, Doctoral thesis, LRAP-348, (Lund Institute of Technology, Lund, 2005)

[23] M. Soto Thompson, *Photodynamic Therapy utilizing Interstitial Light Delivery Combined with Spectroscopic Methods*, Doctoral thesis, LRAP-331,(Lund Institute of Technology, Lund, 2004)

[24] S. Andersson-Engels, http://kurslab.fysik.lth.se/FED4Medopt/diffusion2.pdf, 2006-05-28

[25] S. A. Prahl et al., "A Monte Carlo model of light propagation in tissue", *SPIE Institute Series*, Vol. IS 5 (1989)

[26] S. Svanberg, *Atomic and Molecular Spectroscopy*, 4th edition, Chapter 8, Springer-Verlag, Berlin Heidelberg (2004)

[27] J. M. Hollas, *Modern Spectroscopy*, Chapter 9, 4th ed., John Wiley & Sons Ltd, West Sussex (2004)

[28] http://www.signalrecovery.com/, Technical note 1001, 2006-04-06

[29] http://www.signalrecovery.com/, Technical note 1000, 2006-04-06

[30] http://kurslab.fysik.lth.se/FED4Medopt/transport.pdf, 2006-05-29

[31] http://encarta.msn.com/encyclopedia_1741500785/Air.html, 2006-05-24

[32] L. Persson et al., "Diode laser absorption spectroscopy for studies of gas exchange in fruits", *Opt. Lasers Eng*, **44**, 687 – 698 (2006)

[33] http://cfcenter.stanford.edu/CFNews-Sinusitis.html, 2006-05-24

[34] http://www.sinuswars.com/sinus.htm, 2006-05-24

[35] T. Petrén, *Lärobok i anatomi, Del 1 rörelseapparaten*, Aktiebolaget nordiska bokhandlens förlag, Stockholm (1976)

[36] http://cfcenter.stanford.edu/CFNews-Sinusitis.html, 2006-05-29

[37] http://www.umm.edu/careguides/allergy/allergy_sinusitis.html, 2006-05-24

[38] A.J.Welch and M. J. C. van Gemert, *Optical-Thermal Response of Laser-Irradiated Tissue*, Page 261, Plenum Press, New York, (1995)

[39] M. Sundberg, http://www.biop.dk/biophotonics05/posters/sundberg_poster.pdf, 2006-05-29

[40] Breault Research Orginazation, Inc.,"Wave optics in ASAP", *ASAP Procedural Note*, Tucson (2005)

[41] Breault Research Orginazation, Inc., *The ASAP^{TM} Primer*, Tucson (2005)

[42] Breault Research Orginazation, Inc., "Using voxels in ASAP modeling fluorescence and volume scatter", *ASAP Procedural Note*, Tucson (2005)

[43] L. Wang and S. L. Jacques, "Monte Carlo modeling of light transport in multi-layered tissues", standard C, (Laser biology research laboratory, M. D. Anderson cancer center, University of Texas, Houston, Texas 1992)

[44] http://kurslab.fysik.lth.se/FED4Medopt/ISlabhl.pdf, 2006-05-24

[45] J. Sørensen, *Optical analysis of biological media*, Doctoral thesis, LRAP-265, (Lund Institute of Technology, Lund, 2000)

[46] N. Yavari, *Optical spectroscopy for tissue diagnostics*, Licentiate thesis, LRAP-358, (Lund Institute of Technology, Lund, 2006)

[47] http://kurslab.fysik.lth.se/FED4Medopt/temporallab.pdf, 2006-05-24

[48] T. Svensson et al., "Characterization of normal breast tissue heterogeneity using time-resolved near-infrared spectroscopy", *Phys. Med. Biol.* **50** (2005).

[49] T. Vo-Dinh, *Biomedical Photonics Handbook*, Chapter 2 , CRC Press LLC (2003)

[50] N. Lynnerup et al., "Thickness of the human cranial diploe in relation to age, sex and general body build", *Head & Face Medicine*, **1**, 13 (2005)

[51] S. Ijichi et al., "Developmental Changes of Optical Properties in Neonates Determined by Near-Infrared Time-Resolved Spectroscopy", *Pediatric Research*, **58**, 568-573 (2005)

[52] N. Ugryumova et. al., "Measurement of bone mineral density via light scattering", *Phys. Med. Biol.*, **49**, 472 (2004)

[53] C. J. Foot, *Atomic physics*, Appendix C, Oxford University Press (2005)

[54] R. C. Haskell et al., "Boundary conditions for the diffusion equation in radiative transfer" *J. Opt. Soc. Am. A*, **11**, 10, 2730 – 2731 (1994)

Appendix A

Magnetic dipole transitions

In the same way as the electric field of an electromagnetic wave gives rise to electric dipole transitions, the magnetic field component induces magnetic dipole transitions (interact with the magnetic dipole moment) in atoms and molecules. The matrix elements of the electric dipole moment is given by

$$\mathbf{R}^{nm} = \int \psi_n^* \mathbf{M} \psi_m d\tau \qquad (A.1)$$

Here $\mathbf{M}$ is the electric dipole moment and ψ_n and ψ_m are the eigenfunctions of the two states n and m. If $\mathbf{R}^{nm}$, also called the transition moment, differs from zero for the states n and m, the states combine with each other with a certain probability for emission or absorption of radiation. If the transition moment is zero the transition is forbidden as an electric dipole transition. In the case of the magnetic dipole moment, it should be substituted in place of the electric, in Eq. A.1. If the matrix elements of the magnetic dipole moment are different from zero there is a non-zero transition probability. The transitions are only 10^{-5} of typical dipole transition probabilities, why they are considered forbidden [18].

Magnetic dipole transitions do not obey the same selection rules as electric. Both sets of selection rules can be seen in Table A.1 below. The fact that $\Delta l = 0$ and $\Delta n = 0$ for magnetic dipole transitions, means that there must be no change of configuration [53].

Electric dipole transitions		Magnetic dipole transitions	
$\Delta J = 0, \pm 1$	$0 \leftrightarrow 0$ forbidden	$\Delta J = 0, \pm 1$	$0 \leftrightarrow 0$ forbidden
$\Delta M_j = 0, \pm 1$		$\Delta M_j = 0, \pm 1$	
Parity change		No parity change	
$\Delta l = \pm 1$		$\Delta l = 0$	
Any Δn		$\Delta n = 0$	
$\Delta L = 0, \pm 1$		$\Delta L = 0$	
$\Delta S = 0$		$\Delta S = 0$	

Table A.1: Selection rules

Appendix B

Calculating an extrapolated boundary

According to R. C. Haskell et al. [54] the extrapolated boundary for a medium of a certain refractive index n, can be calculated as follows:

$$z_b \quad = \quad \frac{|\phi|}{3|j_z|} z_0 = \frac{2}{3} \frac{1 + R_j}{1 - R_\phi} z_0 \tag{B.1}$$

$$R_\phi \quad \equiv \quad \int_0^{\frac{\pi}{2}} 2 \sin\theta \cos\theta R_{Fresnel}(\theta) d\theta \tag{B.2}$$

$$R_J \quad \equiv \quad \int_0^{\frac{\pi}{2}} 3 \sin\theta \cos^2\theta R_{Fresnel}(\theta) d\theta \tag{B.3}$$

$$R_{Fresnel}(\theta) \quad = \quad \frac{1}{2} \left(\frac{n\cos\theta' - n_{out}\cos\theta}{n\cos\theta' + n_{out}\cos\theta} \right)^2 +$$

$$+ \frac{1}{2} \left(\frac{n\cos\theta - n_{out}\cos\theta'}{n\cos\theta + n_{out}\cos\theta'} \right)^2$$

$$\text{when } 0 \le \theta \le \theta_c \tag{B.4}$$

$$R_{Fresnel}(\theta) \quad = \quad 1 \qquad \text{when } \theta_c \le \theta \le \frac{\pi}{2} \tag{B.5}$$

where θ is the angle of the incoming light, θ' is the angle of the reflected light and θ_c is the critical angle for which there will be total reflection, i.e. $\theta' = \pi/2$. The angles θ' and θ_c are given by Snell's law:

$$n\sin\theta \quad = \quad n_{out}\sin\theta' \tag{B.6}$$

$$n\sin\theta_c \quad = \quad n_{out} \tag{B.7}$$

The extrapolated boundary was calculated in Matlab after insertion of the refractive indices: $n = 1.48$, $n_{out} = 1$,

Appendix C

ASAP^{TM} code for the backscattering phantom model

```
      SYSTEM NEW
RESET

!!BACKSCATTERING PHANTOM MODEL

!! Define system units and wavelengths

UNITS MILLIMETERS 'mW'
WAVELENGTH 760 NM
LEVEL 2000000000

!! Define coatings

COATING PROPERTIES

   0 0 'ABSORB'
   0 1 'TRANSMIT'
   1 0 'REFLECT'

!! Define Media

MODELS
   VOLUME scatter 0.87 efficiency 14`0.0005 obscuration 1  !!PLOT

MODELS
   VOLUME scatter 0.99 efficiency 0.000000001`0.00002  obscuration 1   !!PLOT

MEDIA 1
   1.48 SCATTER 1 0 1 1000000 1000000 'DELRIN'

MEDIA
   1.0 SCATTER 2 'OXY'
   1.53 'SCHOTTRG715'
   1.49 'PLEXI'
   !!1.511 'BK7GLASS'

FRESNEL TIR

SPLIT 10 MONTECARLO

!! GEOMETRY DEFINITIONS BEGIN HERE

   !!   DETECTOR

SURFACE
   PLANE  Z -10.7 ELLIPSE 10.5 10.5
OBJECT 'DETECTOR'
   INTERFACE COATING ABSORB AIR AIR

   !! FRONT OF FILTER

SURFACE
   PLANE  Z -10.6 ELLIPSE 10.50
OBJECT 'FILTER.FRONT'
   INTERFACE COATING BARE AIR SCHOTTRG715
    REDEFINE COLOR 10

   !!BACK OF FILTER

SURFACE
   PLANE  Z -7.6 ELLIPSE 10.50
OBJECT 'FILTER.BACK'
   INTERFACE COATING BARE AIR SCHOTTRG715
    REDEFINE COLOR 10

   !! SIDE OF FILTER

EDGE
```

```
  ELLIPSE  Z -10.60 10.50 10.50 64 0 360
  ELLIPSE Z -7.6 10.5 10.5 64 0 360
OBJECT 'FILTER.SIDE'
  .1 .2
  INTERFACE COATING BARE AIR SCHOTTRG715
  REDEFINE COLOR 10

  !! PLEXIGLAS

EDGE
POINTS X 0
10.5 2.5 1
10.5 -7.5 1
0 -7.5 1
0 -2.62 1
3.62 -2.62 1
3.62 2.5 1
SWEEP AXIS 360 Z
OBJECT 'PLEXI.BODY'
INTERFACE COATING BARE PLEXI AIR



  !! PLEXIGLAS COATING

EDGE
POINTS X 0
0 -2.6 1
3.6 -2.6 1
3.6 2.49 0
SWEEP AXIS 360 Z
OBJECT 'PLEXI.INNER_COATING'
INTERFACE COATING ABSORB AIR AIR

EDGE
POINTS X 0
10.6 2.5 1
10.6 -10.7 1
  SWEEP AXIS 360 Z
  OBJECT 'PLEXI.OUTER_COATING'
  INTERFACE COATING ABSORB AIR AIR

  !! PRISM


LENSES

  RIGHT Y -2.5 2.5 ''SCHOTT_BK7''  Z
OBJECT 'PRISM.PRISM'


!! PLEXI GLASS SURFACE

SURFACE
  PLANE Z 2.6 ELLIPSE 100
  OBJECT 'PLEXI.SURFACE'
  INTERFACE COAT TRANSMIT AIR AIR


  !! FRONT OF VOLUME 1

SURFACE
  PLANE  Z 2.7 RECTANGLE 50.0
OBJECT 'S1.FRONT'
  INTERFACE COATING BARE AIR DELRIN
  REDEFINE COLOR 18
```

```
!! BACK OF VOLUME 1

SURFACE
   PLANE  Z 5.7 RECTANGLE 50.0
OBJECT 'S1.BACK'
   INTERFACE COATING BARE OXY DELRIN
   REDEFINE COLOR 18

   !! SIDE OF VOLUME 1


EDGE
   RECTANGLE Z 2.7 50.0 50.0 16 0 360
   RECTANGLE Z 5.7 50.0 50.0 16 0 360
OBJECT 'S1.SIDE'
   .1 .2
   INTERFACE COATING BARE AIR DELRIN
   REDEFINE COLOR 18



   !! SIDE OF OXYGEN


EDGE
   RECTANGLE Z 5.7 50.0 50.0 16 0 360
   RECTANGLE Z 6.7 50.0 50.0 16 0 360
OBJECT 'OXYGEN'
   .1 .2
   INTERFACE COATING TRANSMIT AIR OXY

   !! FRONT OF VOLUME 2

SURFACE
   PLANE  Z 6.7 RECTANGLE 50.0
OBJECT 'S2.FRONT'
   INTERFACE COATING BARE OXY DELRIN
   REDEFINE COLOR 18

   !! BACK OF VOLUME 2

SURFACE
   PLANE  Z 16.7000 RECTANGLE 50.0
OBJECT 'S2.BACK'
   INTERFACE COATING BARE AIR DELRIN
   REDEFINE COLOR 18

   !! SIDE OF VOLUME 2


EDGE
   RECTANGLE Z 6.7 50.0 50.0 16 0 360
   RECTANGLE Z 16.7000 50.0 50.0 16 0 360
OBJECT 'S2.SIDE'
   .1 .2
   INTERFACE COATING BARE AIR DELRIN
   REDEFINE COLOR 18




!! SOURCE DEFINITIONS BEGIN HERE

EMITTING DISK Y -2.8 0.3 0.3 1000000 10.0 10.0
FLUX TOTAL 2.0


!! TRACE RAYS
```

```
HALT 1000 1E-6


SAVE 10

TRACE

CONSIDER ONLY DETECTOR
$IO OUTPUT BS1MM ONLY
HISTORY LIST
$IO OUTPUT CLOSE



CONSIDER ONLY DETECTOR

STATS

$BEEP
```

Appendix D

ASAP^{TM} code for the transmission phantom model

```
   SYSTEM NEW
RESET

!!TRANSMISSION PHANTOM MODEL

!! DEFINE SYSTEM UNITS AND WAVELENGTH

UNITS MILLIMETERS 'mW'
WAVELENGTH 760 NM
LEVEL 10000000

!! DEFINE COATINGS

COATING PROPERTIES

   0 0 'ABSORB'
   0 1 'TRANSMIT'
   1 0 'REFLECT'

!! DEFINE MEDIA

MODELS
   VOLUME scatter 0.93 efficiency 9.3`0.0005 obscuration 1   !!PLOT

MODELS
   VOLUME scatter 0.99 efficiency 0.000000001`0.00002  obscuration 1   !!PLOT

MEDIA 1
   1.48 SCATTER 1 0 1 1000000 1000000 'DELRIN'

MEDIA
   1.0 SCATTER 2 'OXY'
   1.53 'SCHOTTRG715'


FRESNEL TIR

SPLIT 10 MONTECARLO

!! GEOMETRY DEFINITIONS BEGIN HERE



   !! FRONT OF VOLUME 1

SURFACE
   PLANE  Z 0.0 RECTANGLE 50.0
OBJECT 'S1.FRONT'
   INTERFACE COATING BARE AIR DELRIN
   REDEFINE COLOR 18

   !! BACK OF VOLUME 1

SURFACE
   PLANE  Z 10.0 RECTANGLE 50.0
OBJECT 'S1.BACK'
   INTERFACE COATING BARE OXY DELRIN
   REDEFINE COLOR 18

   !! SIDE OF VOLUME 1


EDGE
   RECTANGLE Z 0.0 50.0 50.0 16 0 360
   RECTANGLE Z 10.0 50.0 50.0 16 0 360
OBJECT 'S1.SIDE'
   .1 .2
   INTERFACE COATING BARE AIR DELRIN
```

```
     REDEFINE COLOR 18

       !! OXYGEN

EDGE
     RECTANGLE Z 10.0000 50.0 50.0 16 0 360
     RECTANGLE Z 11.0000 50.0 50.0 16 0 360
OBJECT 'OXYGEN'
     .1 .2
     INTERFACE COATING BARE AIR OXY
     REDEFINE COLOR 1

       !! FRONT OF VOLUME 2

SURFACE
     PLANE  Z 11.0 RECTANGLE 50.0
OBJECT 'S2.FRONT'
     INTERFACE COATING BARE OXY DELRIN
     REDEFINE COLOR 18

       !! BACK OF VOLUME 2

SURFACE
     PLANE  Z 21.0 RECTANGLE 50.0
OBJECT 'S2.BACK'
     INTERFACE COATING BARE AIR DELRIN
     REDEFINE COLOR 18

       !! SIDE OF VOLUME 2


EDGE
     RECTANGLE Z 11.0 50.0 50.0 16 0 360
     RECTANGLE Z 21.0 50.0 50.0 16 0 360
OBJECT 'S2.SIDE'
     .1 .2
     INTERFACE COATING BARE AIR DELRIN
     REDEFINE COLOR 18

       !!  MASK

SURFACE
     PLANE  Z 21.0001 ELLIPSE 100
OBJECT 'MASK'
     INTERFACE COATING TRANSMIT AIR AIR


       !! FRONT OF FILTER

SURFACE
     PLANE  Z 21.1 ELLIPSE 10.50
OBJECT 'FILTER.FRONT'
     INTERFACE COATING BARE AIR SCHOTTRG715
     REDEFINE COLOR 10

       !!BACK OF FILTER

SURFACE
     PLANE  Z 24.10 ELLIPSE 10.50
OBJECT 'FILTER.BACK'
     INTERFACE COATING BARE AIR SCHOTTRG715
     REDEFINE COLOR 10

       !! SIDE OF FILTER

SURFACE
     TUBE  Z 0.0 10.50 10.50 23.0 10.50 10.50
OBJECT 'FILTER.SIDE'
```

```
   INTERFACE COATING BARE AIR SCHOTTRG715
   BOUNDS -.2 +.3
   REDEFINE COLOR 10

   !!  DETECTOR

SURFACE
   PLANE  Z 24.10001 ELLIPSE 10.50 10.50
OBJECT 'DETECTOR'
   INTERFACE COATING ABSORB AIR AIR


!! SOURCE DEFINITIONS BEGIN HERE

EMITTING DISK Z -0.0001 0.3 0.3 2000001 10.0 10.0

FLUX TOTAL 2.0

!! TRACE RAYS
SAVE 10

TRACE

CONSIDER ONLY DETECTOR
$IO OUTPUT T1MM ONLY
HISTORY LIST
$IO OUTPUT CLOSE
```

Appendix E

ASAP^{TM} code for the frontal sinuses imaging

```
!!SPATIAL RESOLUTION FRONTAL SINUSES

$DO 0 34 2
{
!!_____
SYSTEM NEW
RESET

UNITS MM 'mW'
WAVELENGTH 760 NM

LEVEL 2E9

COATING PROPERTIES
   0 1 'TRANSMIT'
   1 0 'REFLECT'
   0 0 'ABSORB'

MODEL
   VOLUME 0.99 1E-9`2E-5 1

MODEL
   VOLUME 0.93 9.3 1

MEDIA
   1.0 'AIR'
   1.53 'SCHOTT'
   1.49 'PLEXI'
   1.0 SCATTER .2 'OXY'
   1.48 SCATTER .1 0 1 10000000 10000000 'SPRID'

FRESNEL TIR

SPLIT 10 MONTECARLO

HALT 1000 1E-6
!!-------------------------------------------------------------

!!_____
!!DETECTOR
SURFACE
   PLANE Z -10.7 ELLIP 10.5 10.5
   OBJECT 'PMT'
   INTERFACE COATING ABSORB AIR AIR
   REDEFINE COLOR 1


!!FILTER
SURFACE
   PLANE Z -10.6 ELLIP 10.5 10.5
   OBJECT 'FILTER.FRONT'
   INTERFACE COATING BARE AIR SCHOTT
   REDEFINE COLOR 2

SURFACE
   PLANE Z -7.6 ELLIP 10.5 10.5
   OBJECT 'FILTER.BACK'
   INTERFACE COATING BARE AIR SCHOTT
   REDEFINE COLOR 2

EDGE
   ELLIP Z -10.6 10.5 10.5 64 0 360
EDGE
   ELLIP Z -7.6 10.5 10.5 64 0 360
OBJECT
   .1 .2 'FILTER.EDGE'
   INTERFACE COATING BARE AIR SCHOTT
```

```
      REDEFINE COLOR 2


   !!PLEXI
   EDGE
      POINTS X 0
      10.5 2.5 1
      10.5 -7.5 1
      0 -7.5 1
      0 -2.62 1
      3.62 -2.62 1
      3.62 2.5 1
      SWEEP AXIS 360 Z
   OBJECT 'PLEXI.EDGE'
      INTERFACE COATING BARE PLEXI AIR
      REDEFINE COLOR 3

   EDGE
      POINTS X 0
      0 -2.6 1
      3.6 -2.6 1
      3.6 2.49 0
      SWEEP AXIS 360 Z
   OBJECT 'PLEXI.INNER_COATING'
      INTERFACE COATING ABSORB AIR AIR
      REDEFINE COLOR 4

   EDGE
      POINTS X 0
      10.6 2.5 1
      10.6 -10.7 1
      SWEEP AXIS 360 Z
   OBJECT 'PLEXI.ABSORB'
      INTERFACE COATING ABSORB AIR AIR
      REDEFINE COLOR 4



   !!PRISM
   LENSES
      RIGHT Y -2.5 2.5 ''SCHOTT_BK7'' Z
      OBJECT 'PRISM.PRISM'


   !!MASK
   SURFACE
      PLANE Z 2.6 ELLIP 40 40
      OBJECT 'MASK'
      INTERFACE COATING TRANSMIT AIR AIR
      REDEFINE COLOR 6


   !!FOREHEAD
   SURFACE
      PLANE Z 2.7 RECTANGLE 75 75
      OBJECT 'S1.FRONT'
      INTERFACE COATING BARE AIR SPRID
      REDEFINE COLOR 9
   SURFACE
      PLANE Z 52.7 RECTANGLE 75 75
      OBJECT 'S1.BACK'
      INTERFACE COATING BARE AIR SPRID
      REDEFINE COLOR 9
   EDGE
      RECTANGLE Z 2.7 75 75 16 0 360
   EDGE
      RECTANGLE Z 52.7 75 75 16 0 360
```

```
OBJECT
   .1 .2 'S1.SIDE'
   INTERFACE COATING BARE AIR SPRID
   REDEFINE COLOR 9

!!FRONTAL SINUS 1
ENT OBJECT
   ELLIPSOID 10 12.5 5 12.5 0 12.7 'BIHALA.1'
   INTERFACE COATING BARE SPRID OXY
   REDEFINE COLOR 7
!!FRONTAL SINUS 2_____
ENT OBJECT
   ELLIPSOID 10 12.5 5 -12.5 0 12.7 'BIHALA.2'
   INTERFACE COATING BARE SPRID OXY
   REDEFINE COLOR 7
!!_____
!!CONTROL SURFACES_____
ENT OBJECT
   ELLIPSOID 9.99 12.49 4.99 12.5 0 12.7 'INRE.1'
   INTERFACE COATING TRANSMIT OXY OXY
   REDEFINE COLOR 9
!!_____
ENT OBJECT
   ELLIPSOID 9.99 12.49 4.99 -12.5 0 12.7 'INRE.2'
   INTERFACE COATING TRANSMIT OXY OXY
   REDEFINE COLOR 9

GROUP .1 .2 .3 .4 .5 .6 .7
SHIFT X ?
SHIFT Y 16


!!-------------------------------------------
!!SOURCE
EMITTING DISK Y -2.8 0.3 0.3 500000 10 10
FLUX TOTAL 2


!!-------------------------------------------


!!TRACE RAYS

SAVE 10


TRACE

CONSIDER ONLY PMT

$IO OUTPUT ?_16_5MMCHILD.OUT ONLY
HISTORY LIST
$IO OUTPUT CLOSE

RETURN

}
```

Appendix F

ASAP^{TM} code for the maxillary sinuses imaging

```
!! SPATIAL RESOLUTION MAXILLARY SINUSES

$DO 1 9 2
{
$TIC
!!_____
SYSTEM NEW
RESET

UNITS MM 'mW'
WAVELENGTH 760 NM

LEVEL 2E9

COATING PROPERTIES
   0 1 'TRANSMIT'
   1 0 'REFLECT'
   0 0 'ABSORB'

MODEL
VOLUME 0.99 1E-9`2E-5 1


MODEL
   VOLUME 0.87 16 1

MEDIA
   1.0 'AIR'
   1.53 'SCHOTT'
   1.49 'PLEXI'
   1.0 SCATTER .2 'OXY'
   1.48 SCATTER .1 0 1 10000000 10000000 'DELRIN'

FRESNEL TIR

SPLIT 10 MONTECARLO

HALT 1000 1E-6
!!----------------------------------------------------------------

!!DETECTOR
ENT OBJECT
   ELLIPSOID 79 129 104 0 0 0 'PMT'
   INTERFACE COATING ABSORB AIR AIR
   REDEFINE COLOR 5


!!FILTER
ENT OBJECT
   ELLIPSOID 78.5 128.5 103.5 0 0 0 'FILTER.1'
   INTERFACE COATING BARE SCHOTT AIR
   REDEFINE COLOR 5

!!FILTER
ENT OBJECT
   ELLIPSOID 75.5 125.5 100.5 0 0 0 'FILTER.2'
   INTERFACE COATING BARE SCHOTT AIR
   REDEFINE COLOR 5

!!HEAD
ENT OBJECT
   ELLIPSOID 75 125 100 0 0 0 'HEAD'
   INTERFACE COATING BARE DELRIN AIR
   REDEFINE COLOR 6

!!MAXILLARY SINUS 1
ENT OBJECT
```

```
   ELLIPSOID 15 17.5 20 33 -10 -58 'BIHALA.1'
      INTERFACE COATING BARE DELRIN OXY
      REDEFINE COLOR 7
      ROTATE Y 40
!!MAXILLARY SINUS 2_____

ENT OBJECT
   ELLIPSOID 14.95 17.45 19.95 33 -10 -58 'BIHALA.2'
      INTERFACE COATING BARE OXY
      REDEFINE COLOR 8
      ROTATE Y 40
!!_____

!!ORAL CAVITY_____
ENT OBJECT
   ELLIPSOID 1 1 1 45 -26 -43 'ORALCAV'
      INTERFACE COATING BARE AIR DELRIN
      REDEFINE COLOR 9
!!_____

!!-------------------------------------------------------

!!SOURCE
SEED 2000010?
EMITTING DISK Y 0 0.3 0.3 80000 10 10
      FLUX TOTAL 2
      SHIFT X 45
      SHIFT Y -26
      SHIFT Z -43
      ROTATE X -60 -26 -43
      ROTATE Z 30 45 -26
!!SOURCE

!!-------------------------------------------------------


!!TRACE RAYS

SAVE 10


TRACE
STATS

CONSIDER ONLY PMT

$IO OUTPUT SEED10?.OUT ONLY
HISTORY LIST
$IO OUTPUT CLOSE

RETURN

$TIC
$BEEP
}
```